# JOURNAL OF CAVE AND KARST STUDIES

December 2018
Volume 80, Number 4
ISSN 1090-6924
A Publication of the National Speleological Society

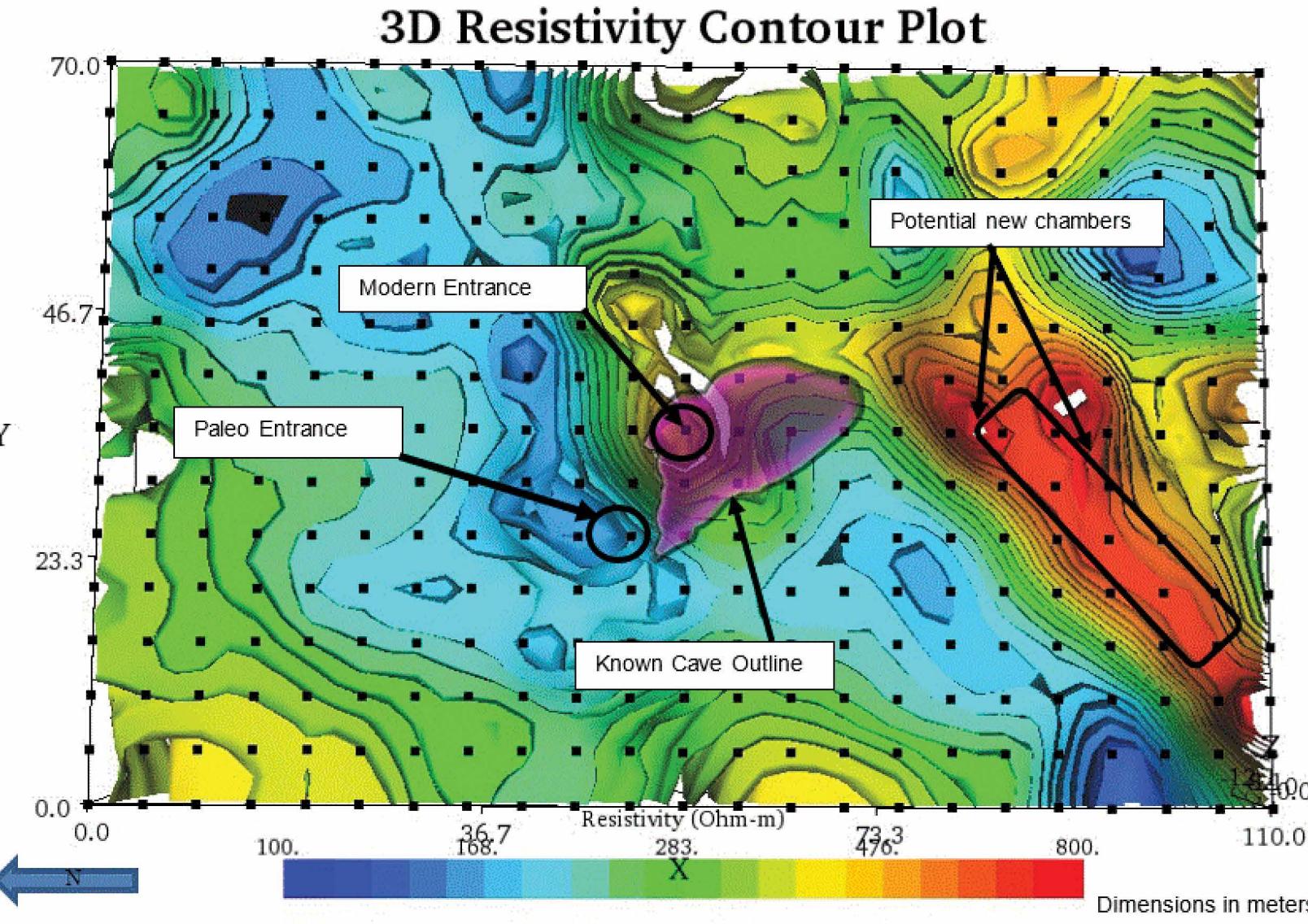


DEDICATED TO THE ADVANCEMENT OF SCIENCE, EDUCATION, EXPLORATION, AND CONSERVATION

**Published By**
**The National Speleological Society**

**http://caves.org/pub/journal**

**Office**
6001 Pulaski Pike NW
Huntsville, AL 35810 USA
Tel:256-852-1300
nss@caves.org

**Editor-in-Chief**
**Malcolm S. Field**
National Center of Environmental
Assessment (8623P)
Office of Research and Development
U.S. Environmental Protection Agency
1200 Pennsylvania Avenue NW
Washington, DC 20460-0001
703-347-8601 Voice 703-347-8692 Fax
field.malcolm@epa.gov

**Production Editor**
**Scott A. Engel**
Knoxville, TN
225-281-3914
saecaver@gmail.com

**Journal Copy Editor**
**Linda Starr**
Albuquerque, NM

The *Journal of Cave and Karst Studies* , ISSN 1090-6924, CPM Number #40065056, is a multi-disciplinary, refereed journal published four times a year by the National Speleological Society. The *Journal* is available by open access on its website, or check the website for current print subscription rates. Back issues are available from the NSS office.

POSTMASTER: send address changes to the National Speleological Society Office listed above.

The Journal of Cave and Karst Studies is covered by the following ISI Thomson Services Science Citation Index Expanded, ISI Alerting Services, and Current Contents/Physical, Chemical, and Earth Sciences.

Copyright © 2018
by the National Speleological Society, Inc.

**BOARD OF EDITORS**

**Anthropology**
**George Crothers**
University of Kentucky
Lexington, KY
george.crothers@utk.edu

**Conservation-Life Sciences**
**Julian J. Lewis & Salisa L. Lewis**
Lewis & Associates, LLC.
Borden, IN
lewisbioconsult@aol.com

**Earth Sciences**
**Benjamin Schwartz**
Texas State University
San Marcos, TX
bs37@txstate.edu

**Leslie A. North**
Western Kentucky University
Bowling Green, KY
leslie.north@wku.edu

**Mario Parise**
University Aldo Moro
Bari, Italy
mario.parise@uniba.it

**Exploration**
**Paul Burger**
National Park Service
Eagle River, Alaska
paul_burger@nps.gov

**Microbiology**
**Kathleen H. Lavoie**
State University of New York
Plattsburgh, NY
lavoiekh@plattsburgh.edu

**Paleontology**
**Greg McDonald**
National Park Service
Fort Collins, CO
greg_mcdonald@nps.gov

**Social Sciences**
**Joseph C. Douglas**
Volunteer State Community College
Gallatin, TN
615-230-3241
joe.douglas@volstate.edu

**Book Reviews**
**Arthur N. Palmer & Margaret V Palmer**
State University of New York
Oneonta, NY
palmeran@oneonta.edu

Front cover: Electrical resistivity survey completed at Friesenhahn Cave. See Muhlestein et al. in this issue.

Rafał Ogórek, C, Katarzyna Guz-Regner, Tomasz Kokurewicz, Elżbieta Baraniok, and Bartosz Kozak. Airborne bacteria cultivated from underground hibernation sites in the Nietoperek bat reserve (Poland). *Journal of Cave and Karst Studies*, v. 80, no. 4, p. 161-171. DOI:10.4311/2017MB0117

# AIRBORNE BACTERIA CULTIVATED FROM UNDERGROUND HIBERNATION SITES IN THE NIETOPEREK BAT RESERVE (POLAND)

Rafał Ogórek[1, C], Katarzyna Guz-Regner[2], Tomasz Kokurewicz[3], Elżbieta Baraniok[1], Bartosz Kozak[4]

Abstract

The study is the first report of cultivable bacteria present in the close vicinity of hibernating bats. Samples were collected in January 2016 in one location outside the hibernation site and in five locations underground. Samples were incubated at 7 and 37 °C. Bacteria were identified based on phenotypic tests and 16S rRNA gene analysis. Air samples collected inside of underground sites contained more propagules of bacteria (from 232 ± 28.3 to 1189 ± 124.7 bacterial colony-forming units per $m^3$ of air) than outdoor air samples (42 ± 12.2). In total, eight species of airborne bacteria belonging to three phyla and three orders were cultured from the samples. More species of airborne bacteria, eight, were isolated from the indoor underground air samples than from the outdoor air, two, especially in close vicinity to hibernating bats. Generally, *Actinobacteria* dominated in this study. *Paeniglutamicibacter psychrophenolicus* was isolated most frequently from samples incubated at 7 °C, and *Micrococcus luteus* from samples incubated at 37 °C. Additionally, the study was supplemented by detailed phenotypic and physiological characteristics of airborne bacteria obtained in the Nietoperek bat reserve.

## Introduction

Microorganisms, especially extremophilic Bacteria and Archaea, are able to colonize all niches of the biosphere, including underground ecosystems (Rampelotto, 2013). However, because of low constant temperatures and high humidity of the air, little availability of nutrients, no light, and extensive areas of mineral surfaces, underground ecosystems are one of the most inhospitable habitats for microbial life (Jurado et al., 2010; Vanderwolf et al., 2013; Ogórek et al., 2014). Specific microclimatic conditions in underground sites, especially low temperatures (ca. from 2 °C to 10 °C) and high relative humidity (above 80 %) of air, allow bats to minimize energy during hibernation, when their food supply is scarce from late autumn to early spring (Speakman and Racey, 1989; Kokurewicz, 2004).

From August to October, before hibernation starts, bats gather in underground sites and actively fly in front of entrances to the underground. This phenomenon, known as swarming, involves circling both inside and outside the hibernacula (Fenton, 1969; Kretzschmar and Heinz, 1995). Due to their unique lifestyle, bats can provide organic nutrients and microorganisms for caves and other subterranean habitats directly from the surface of their bodies or indirectly through their guano. In addition, bat carcasses can be a source of organic matter for bacteria and fungi and a food source for arthropods (Veikkolainen et al., 2014; Kokurewicz et al., 2016; Ogórek et al., 2016a). However, it should be mentioned that other factors such as air currents, percolation via surface water, soil, and sediments, human activities, and the presence of small mammals and arthropods may also influence underground ecosystems and provide energy sources and nutrients (Chelius et al., 2009; Vanderwolf et al., 2013; Ogórek et al., 2016b).

The majority of microorganisms cannot actively grow in the subterranean ecosystems, but they could be present in aerosol form (Ogórek et al., 2016b). Bioaerosols may contain bacteria, fungi, viruses, cellular fragments, fungal spores, and byproducts of microbial metabolism such as mycotoxins, endotoxins, enterotoxins, and enzymes (Mandal and Brandl, 2011). Many reports have been published about underground airborne bacteria and fungi (Rdzanek et al., 2015; Ogórek et al., 2016a, 2016b), but only one microbiological study has been published for a large bat-hibernation site that relates to airborne fungi. It was found that the number of cultivable airborne fungi increase significantly during the hibernation season (Kokurewicz et al., 2016). There are no known similar reports regarding bacteria or bacteria and fungi in bioaerosols a short distance from hibernating bats.

The aims of the study were to determine phenotypic and genotypic diversity of airborne bacteria present close to hibernating bats, to quantify their concentrations, and to assess the pathogenic potential for bat assemblages and in the underground system of Nietoperek bat reserve.

[1]University of Wroclaw, Institute of Genetics and Microbiology, Department of Genetics, Przybyszewskiego Street 63/77, 51-148 Wroclaw, Poland
[2]University of Wroclaw, Institute of Genetics and Microbiology, Department of Microbiology, Przybyszewskiego Street 63/77, 51-148 Wroclaw, Poland
[3]Wrocław University of Environmental and Life Sciences, Institute of Biology, Department of Vertebrate Ecology and Paleontology, Kożuchowska 5b, 51-631 Wroclaw, Poland
[4]Wrocław University of Environmental and Life Sciences, Department of Genetics, Plant Breeding and Seed Production, Grunwaldzki Square 24a, 50-363 Wroclaw, Poland
[C]Corresponding author: rafal-ogorek@wp.pl

## Material and methods

### Description of the Study Area

Nietoperek bat reserve is situated in western Poland in the central part of the so-called Międzyrzecz Fortified Front (52°25′N, 15°32′E), which was built by Germans in the 1930s and during World War II. The above-ground bunkers are connected by approximately 32 km long systems of underground railway tunnels (Woźniak, 1996). To protect hibernating bats and their foraging areas around the fortifications the underground system with the surrounding surface area of 7377.37 ha became protected in November 2007 as Natura 2000 site (area code: PLH080003). The underground corridors of the MMF are one of the ten largest bat hibernation sites in the European Union, and most parts are closed for visitors during the hibernation period from October 15 to April 15. Four bat species are under protection in MMF and mentioned in Annex II of the EU Habitat Directive (Directive 92/43/EEC, 1992) (i.e., *Myotis myotis*, *Barbastella barbastellus*, *Myotis dasycneme*, and *Myotis bechsteinii*). The air temperature in the underground complex ranges from 0 °C near the entrances to 10.4 °C in rear parts. So far 12 bat species with a maximum number of 38,594 individuals have been found hibernating there. Since 1995 the dominant species has been the greater mouse-eared bat (*M. myotis*), constantly increasing in its number since 1985 (Kokurewicz et al., 2014, 2016). Generally, the population of bats in the Nietoperek bat reserve is fairly constant. For example, in January 2014 among all the locations of our study (Fig. 1), the largest number of bats (423 bats) was recorded in section 7.2 (Locations from IV to VI). On the other hand, in Location III there were recorded only several individuals, and in Location II (section 7.8) only ten bats (Kokurewicz et al., 2016).

### Sampling Methods

The observations were made under the license nr.WPN-I.640 I.369.2015.JK issued by Nature Conservancy Management in Gorzów Wielkopolski. The microbial air sampler MAS100-ECO (MBV), and YPG medium (yeast extract peptone glucose: 10.0 g $L^{-1}$ yeast extract, 20.0 g $L^{-1}$ peptone, 20.0 g $L^{-1}$ glucose, 15.0 g $L^{-1}$ agar) were used for the microbiological evaluation of the air. In order to eliminate fungi and yeast from the bacteria samples, 30 g $mL^{-1}$ of nystatin was added to the medium (Polfa, Kraków). The samples were taken on January 9, 2016 from one location situated ca. 5 m in front of the entrance of the underground tunnels of Nietoperek bat reserve and from five locations inside of them (Fig. 1). The microbial air sampler was positioned at a distance of 0.7 m from clusters of *M. myotis* (locations from IV to VII) or it was positioned 1.5 m above the level of the floor (locations from I to III). It was programmed for air sample volumes of 50 L and 100 L, and the measurement in particular sampling sites was performed in triplicates for each volume. The incubation of samples in Petri dishes with YPG medium was carried out at 7 ± 0.5 °C for 21 days and 37 ± 0.5 °C for 5 days. After incubation, bacterial colonies on the plates were counted, and the colony-forming units concentrations were expressed as CFU per cubic meter of air using the formula $X = (a \times 1000) / V$, where $a$ is the number of colonies obtained on a Petri dish, and $V$ is the air volume sampled ($m^3$). Then bacterial colonies were subcultured on YPG medium for phenotypic and molecular identification.

### Phenotypic Studies

Bacterial colonies on YPG medium were subcultured on nonselective media, Nutrient agar (NA, Biocorp, Poland) and Tryptic Soy agar (TSA, Biocorp, Poland) for morphological and phenotypic analyses. Biochemical and enzymatic characteristics of bacterial isolates were determined after incubation at 25 ± 0.5 °C for 48 h by using commercial systems API 20NE and API 20 Staph (Biomerieux) with inoculation of 0.5 McF ($10^8$ CFU $ml^{-1}$) in sterile water solution of 0.85 % NaCl. The profile of substrate utilization by bacteria in oxidative and fermentative conditions was assessed according to recommended procedures using API Aux Medium (1.5 % v/v vitamin solution, 1 % v/v trace elements, 0.15 % agar, 0.2 % $(NH_4)_2SO_4$, 0.62 % $NaH_2PO_4$, 0.15 % KCl) and API Staph Medium (0.05 % yeast extract, 1 % bactopeptone, 0.5 % NaCl, trace elements 1 % v/v). The addition of reagents and the interpretation of reactions were done according to the manufacturer's directions. The supplementary tests, including those for cell morphology and Gram-stain reaction, oxidase and catalase production, and casein, starch, and Tween-80 utilization were performed based on standard methods (Smibert and Krieg, 1994). The ability of growth for bacteria ($C_k$ $10^4$ CFU $mL^{-1}$) at 25 ± 0.5 °C and 35 ± 0.5 °C and in the presence of 12.5 % NaCl at 25 ± 0.5 °C was evaluated visually based on the turbidity of Nutrient Broth (NB, Biocorp, Poland) after incubation for 1 to 3 days. The antimicrobial susceptibility to bacitracin (10UI, Becton Dickinson, Poland) and furazolidone (100 mg $L^{-1}$, Becton Dickinson, Poland) was determined after incubation at 25 ± 0.5 °C for 24 h to 48 h by disc diffusion test on nutrient agar with bacterial suspensions of 0.1 mL $10^8$ CFU $mL^{-1}$ in saline water solution of 0.85 % NaCl. Bacterial isolates without a zone of inhibition were defined as resistant. The ability of $N_2$ fixation by bacteria was detected in culture after incubation at 25 °C for 3 to 5 days by using a modified Ashby (ASH) medium (1 % mannitol, 0.5 % terhalose, 0.5 % glucose, 0.02 % $K_2HPO_4$, 0.02 % $Mg_2SO_4 \cdot 7H_2O$, 0.02 % NaCl, 0.01 % $K_2SO_4$, 0.05 % $CaCO_3$, 1.5 % agar) (Stella and Suhaimi, 2010). The growth of bacteria on this medium indicated the bacterial ability to fix $N_2$ from the air. The results were interpreted using the APIweb software and monographs (Lapage et al., 1968; Kocur et al., 1972, 1975; Kodama et al., 1985; Margesin et al., 2004; Gupta et al., 2004; Lalucat et al., 2006; Zhao

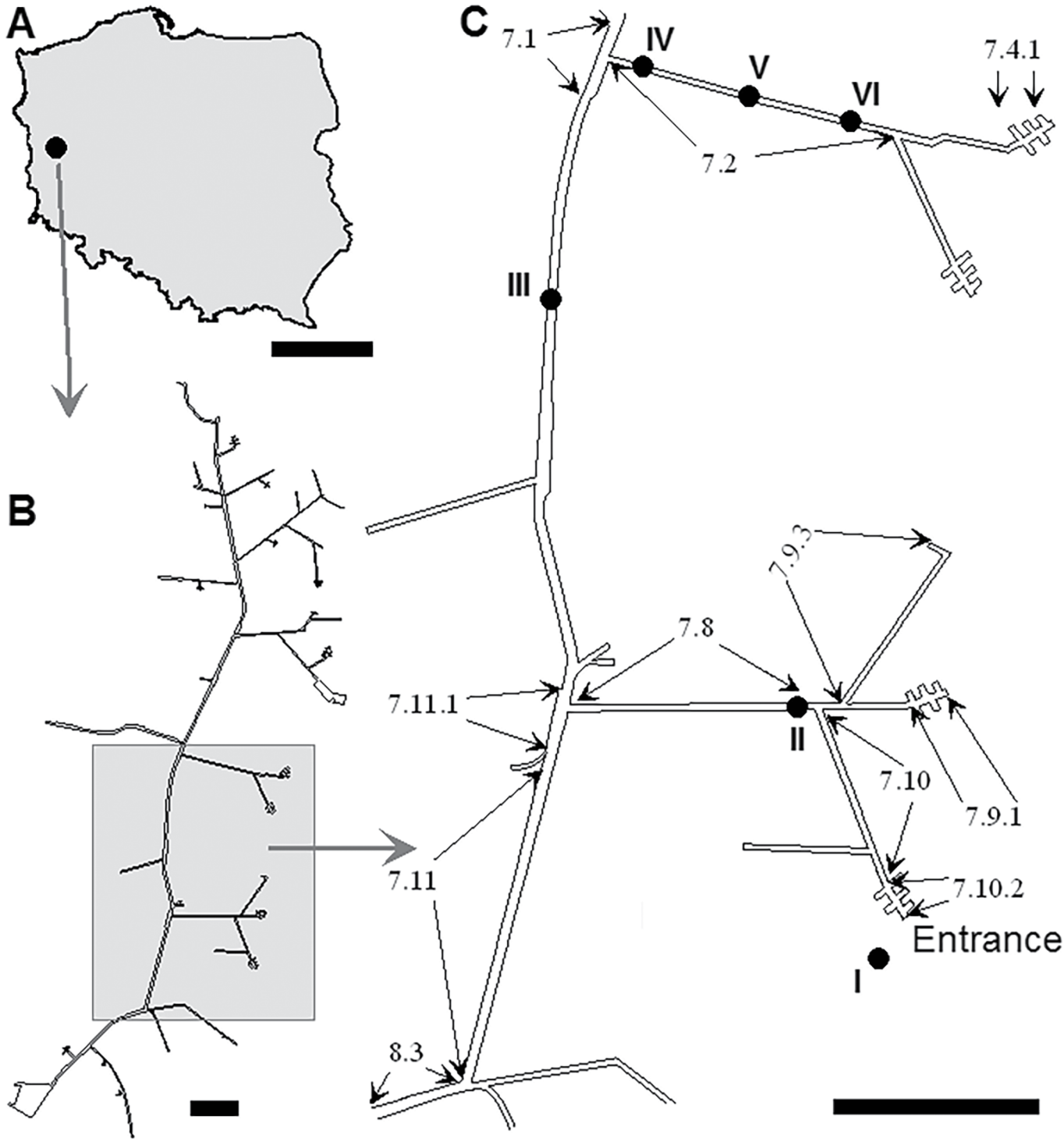


Figure 1. Geographic location of Nietoperek bat reserve in Western Poland (A). The outline of the underground fortification system (B). Sections (7.1–8.3) and sampling sites (C): location I outside the underground fortification system, and locations II to VI inside the underground fortification system. Scale bars: A = 250 km, B and C = 500 m.

et al., 2009; Pindi et al., 2010; Kim et al., 2016). Subsequently, bacterial cultures were genetically analyzed to confirm the affiliation of the species and determine the genetic diversity.

**Molecular Studies**

DNA was extracted according to the CTAB method (Doyle and Doyle, 1987) with minor modifications (Ogórek et al., 2012). Amplification of DNA was performed in a 25 µL reaction mixture using the 2×PCR mixture containing a Taq polymerase (0.1 U $\mu L^{-1}$), dNTP mix (2 mM), $MgCl_2$ (4 mM), 0.25 µM of each primer, rD1: AAGGAGGTGATCCAGCC,

and fD1: AGAGTTTGATCCTGGCTCAG (Weisburg et al., 1991) and 45 ng of DNA in the Biometra thermal cycler for 35 cycles. After initial denaturation for 5 min at 94 °C, each cycle comprised 30 s denaturation at 94 °C, 30 s annealing at 55 °C, 45 s extension at 72 °C, with a final extension for 7 min at 72 °C at the end of 35 cycles. The amplification product was separated on agarose gel (1.5 %), visualized by UV light, purified from the gel and sequenced by the sequencing service at Macrogen (http://dna.macrogen.com/eng/). Partial sequences were analyzed with the BLAST algorithm (http://www.ncbi.nlm.nih.gov/), aligned and compared with published 16s rRNA sequences from GenBank of the National Center for Biotechnology Information, Bethesda, MD, USA.

## Results

Eight species of airborne bacteria belonging to three phyla and three orders were isolated from air samples collected in the Nietoperek bat reserve. The species diversity, eight, of airborne bacteria was higher in air samples collected inside the underground Nietoperek bat reserve than from the outdoor air, two. From indoor and outdoor sites, bacterial species such as *Paeniglutamicibacter psychrophenolicus* and *P. sulfurous* were cultured only from samples incubated at 7 °C. Other bacterial species were cultured only from samples incubated at 37 °C (Tables 1, 2).

**Table 1. Airborne bacteria cultured from air samples in the Nietoperek bat reserve, and results of BLAST analysis (all E values were zero).**

| Isolate | Identification | | Identity with Sequence from GenBank | | |
|---|---|---|---|---|---|
| | Species | GenBank Accession No. | Query Cover, % | Identity, % | Accession |
| UWR_Bak5 | *Dermacoccus nishinomiyaensis* | KY575239.1 | 100 | 93 | NR_044872.1 |
| UWR_Bak7 | *Micrococcus luteus* | KY575241.1 | 98 | 91 | KY317958.1 |
| UWR_Bak4 | *Micrococcus yunnanensis* | KY575238.1 | 98 | 94 | KU877632.1 |
| UWR_Bak8 | *Paenibacillus polymyxa* | KY575242.1 | 98 | 95 | CP011420.1 |
| UWR_Bak1 | *Paeniglutamicibacter psychrophenolicus* | KY575235.1 | 100 | 94 | NR_027226.1 |
| UWR_Bak2 | *Paeniglutamicibacter sulfureus* | KY575236.1 | 96 | 92 | AB046358.1 |
| UWR_Bak6 | *Pseudomonas oryzihabitans* | KY575240.1 | 100 | 91 | LC191548.1 |
| UWR_Bak3 | *Pseudomonas stutzeri* | KY575237.1 | 91 | 91 | CP011854.1 |

Overall, indoor air samples contained more propagules of bacteria than outdoor air samples, from 232 ± 28.3 to 1189 ± 124.7 and 42 ± 12.2 bacterial CFU per $m^3$ of air respectively. The highest number of species isolated from the indoor air was noted for location V (eight bacterial species) and the smallest number of species was noted for location II (four bacterial species). The incubation temperature of samples influenced the number of bacteria cultured from the air (Table 2). After an incubation of samples at 7 °C, the highest number of detected species was noted for location VI (Fig. 2). The bacterial species most frequently isolated from the air outside the Nietoperek bat reserve was *P. psychrophenolicus*, and from the air inside of it was *Micrococcus luteus* (Table 2).

Airborne bacteria isolated from the Nietoperek tunnels showed morphological diversification between the genus, but not within the genus, with the exception of color and colony diameter on nutrient agar medium for *Micrococcus* and *Pseudomonas* spp. All species grew at 25 °C and were resistant to furazolidone. *Paenibacillus polymyxa*, *Pseudomonas oryzihabitans* and *P. stutzeri* were also resistant to bacitracin, all other bacterial species were sensitive to it. Species *P. psychrophenolicus* and *P. sulfureus* did not grow at 35 °C, but others did. Among all tested species, only *M. luteus* showed growth in nutrient broth medium with 12.5 % NaCl. The majority of bacteria required oxygen for growth, with the exception of *P. polymyxa*, which grew in presence and absence of oxygen (Table 3).

The studied biochemical properties of airborne bacteria were diversified, although some trends between species belonging to the same genus were detected. Generally, species were separated into two main clusters. Based on enzymatic metabolism, isolates of *P. psychrophenolicus* and *P. sulfureus* showed the highest similarity, and they differed only in reduction of nitrate to nitrite, utilization of glucose, and phenylacetic acid (Table 4). The most extensive biochemical profile showed *P. polymyxa*, and only this species produced acetylmethylcarbinol, β-glactosidase, β-glucosidase, and utilized lactose and N-acetyl-β-glucosamine. In contrast, the narrowest range of biochemical abilities was shown by *Dermacoccus nishinomiyaensis*. Among all tested biochemical properties, calatase was produced by all tested species, whereas indole was produced by none (Table 4).

## Discussion

Bats (order *Chiroptera*) occur on all continents except Antarctica. Some species inhabit polar regions and isolated oceanic islands (Jones et al., 2009). These small endothermic mammals play important roles in ecosystems and the economy, as plant pollinators, seed dispersers responsible for regeneration of tropical rain forest, predators of insect

**Table 2. Average number of airborne bacteria cultured at 7 °C and 37 °C from air samples in the Nietoperek bat reserve with mean ± standard deviation of CFU per m³ (ND = not detected).**

| Species | Sampling Location | | | | | | | | | | | |
|---|---|---|---|---|---|---|---|---|---|---|---|---|
| | I | | II | | III | | IV | | V | | VI | |
| | 7 °C | 37 °C | 7 °C | 37 °C | 7 °C | 37 °C | 7 °C | 37 °C | 7 °C | 37 °C | 7 °C | 37 °C |
| *Dermacoccus nishinomiyaensis* | ND | ND | ND | ND | ND | ND | ND | 43 ± 9.3 | ND | 86 ± 14.4 | ND | 49 ± 12.7 |
| *Micrococcus luteus* | ND | ND | ND | 36 ± 6.0 | ND | 142 ± 13.6 | ND | 311 ± 45.0 | ND | 432 ± 63.5 | ND | 367 ± 37.5 |
| *Micrococcus yunnanensis* | ND | ND | ND | ND | ND | 65 ± 16.6 | ND | 96 ± 23.6 | ND | 126 ± 24.7 | ND | 103 ± 21.2 |
| *Paenibacillus polymyxa* | ND | ND | ND | 59 ± 8.9 | ND | 11 ± 3.7 | ND | 204 ± 33.2 | ND | 158 ± 24.5 | ND | 115 ± 24.5 |
| *Paeniglutamicibacter psychrophenolicus* | 29 ± 10.2 | ND | 98 ± 21.1 | ND | 146 ± 33.9 | ND | 171 ± 27.8 | ND | 197 ± 29.3 | ND | 227 ± 47.1 | ND |
| *Paeniglutamicibacter sulfureus* | 13 ± 8.5 | ND | 39 ± 13.9 | ND | 45 ± 8.4 | ND | 105 ± 21.2 | ND | 131 ± 26.4 | ND | 176 ± 37.6 | ND |
| *Pseudomonas oryzihabitans* | ND | ND | ND | ND | ND | 34 ± 4.7 | ND | 13 ± 6.6 | ND | 23 ± 7.7 | ND | 9 ± 3.7 |
| *Pseudomonas stutzeri* | ND | ND | ND | ND | ND | ND | ND | 2 ± 1.9 | ND | 36 ± 5.3 | ND | ND |

I – Outside the underground fortification system.
II to VI – Inside the underground fortification system (II = Single individuals), (III = Several individuals), (IV to VI = Large number of bats wintering in clusters).

populations, including agricultural and forest pests, and insects harmful for humans such as mosquitoes (*Culicidae*) and biting midges (*Ceratopogonidae* and *Simuliidae*) (Vilas, 2016). Moreover, most bat species are listed in the IUCN Red list of endangered species and almost half of these are considered threatened or near-threatened (Mickleburgh et al., 2002). Thus, their health and factors determining their favorable conservation status should be monitored, including microbial agents that can cause death in bats (Evans et al., 2009; Mühldorfer et al., 2010). Therefore, microbiological monitoring of bats could be a vital element of the protection of these mammals.

Most of airborne bacterial species isolated a short distance from bats hibernating in the Nietoperek belonged to the *Actinobacteria* phylum. This phylum is widely distributed in the environment and represents one of the largest taxonomic units; it includes five subclasses and fourteen suborders. *Actinobacteria* are also one of the most dominant groups of the skin microbiota in humans, various amphibian species, fish, and bats (Larsen et al., 2013; Kueneman et al., 2014; Hamm et al., 2017). Members of this phylum are well adapted to survive long periods and grow well in nutrient-depleted environments (Barton et al., 2004). Therefore, *Actinobacteria* represent one of the most abundant microbiota from the underground ecosystems where bats hibernate (Northup et al., 2011). However, it should be noted that only fewer than 1% of bacteria from this phylum can be detected by using culture-based methods (Zang et al., 2013). This study supports literature reports that *Actinobacteria* exhibit a wide variety of morphologies as well as diverse physiological and metabolic properties, such as the production of enzymes (Ventura et al., 2007). Other species of airborne bacteria isolated from the Nietoperek belonged to the *Firmicutes* and *Proteobacteria*. These phyla are the cosmopolitan group of environmental bacteria, especially in the colder parts of the world (Teixeira et al., 2010). *Firmicutes* and *Proteobacteria*, like *Actinobacteria*, can colonize the body of bats and their guano, but they are less dominant than the *Actinobacteria* phylum (Hoyt et al., 2015; Banskar et al., 2016). Some species of *Proteobacteria* probably play an important role in maintaining interactions in microbial communities of the skin of bats, decreasing or preventing development and growth of undesirable or pathogenic microbes. For example, *Pseudomonas* spp. isolated from the skin of bats can inhibit *in vitro* the growth of the white-nose syndrome fungus *Pseudogymnoascus destructans* (Hoyt et al., 2015).

The study was conducted during winter, and the bacterial species most frequently isolated from the air samples incubated at 7 °C was *Paeniglutamicibacter psychrophenolicus* (basonym: *Arthrobacter psychrophenolicus*), which is a Gram-positive, non-endospore-forming, non-motile aerobic bacterium (Margesin et al., 2004). *P. psychrophenolicus* belongs to the *Actinobacteria* phylum and cannot grow at temperatures of 35 °C because

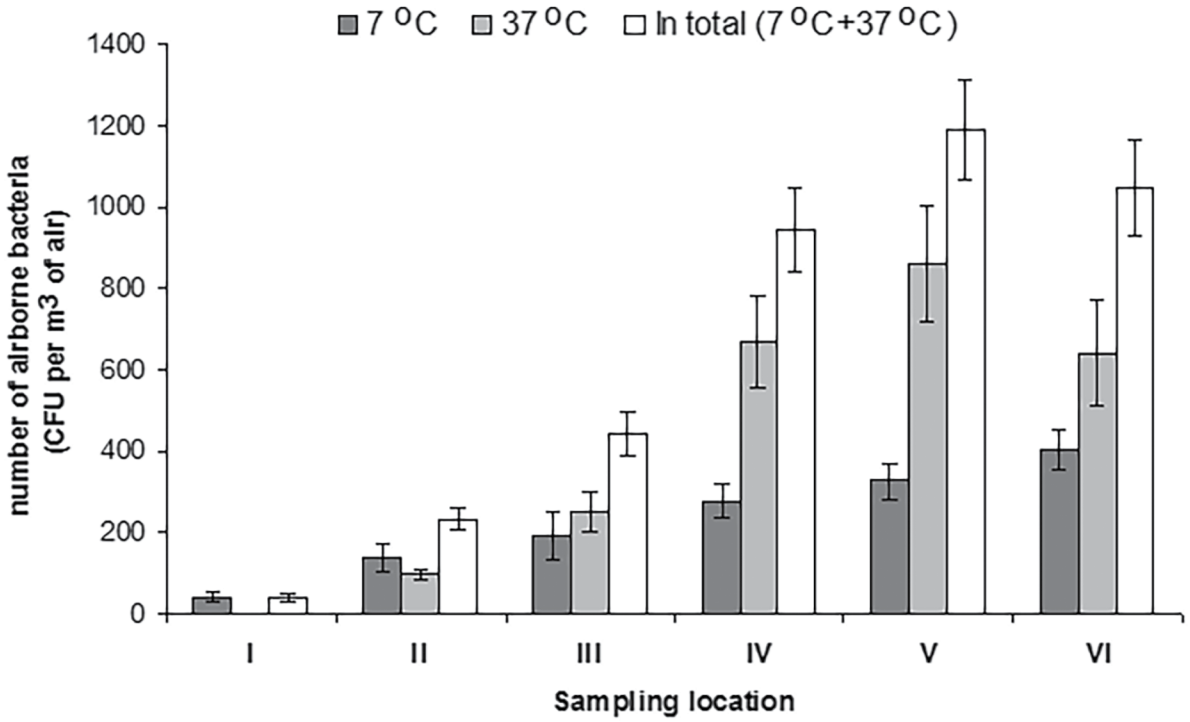


Figure 2. Total number of airborne bacteria (CFU per $m^3$ ± standard deviation) cultured from the Nietoperek bat reserve. Sampling location I was outside the underground fortification system, locations II to VI were inside the underground fortification system (Figure 1). II had single individuals, III had several individuals, and IV–VI had large numbers of bats wintering in clusters.

of its facultative psychrophilic characteristics (Margesin et al., 2004; Ventura et al., 2007). Cold-adapted species belonging to this genus are widespread among bacteria found in subterranean sites, glacier silts, or Arctic and Antarctic environments (Loveland-Curtze et al., 1999; Juck et al., 2000; Stibor et al., 2003). The ability of *P. psychrophenolicus* and *P. sulfureus* to survive in colder temperatures is probably one of the main reasons that these bacterial species were isolated only from the outdoor air samples in this study.

Of particular interest in this study are phenotypic characteristics and the role of *Micrococcus luteus*, because it was the most-isolated species from the air samples incubated at 37 °C. *M. luteus*, in contrast to *P. psychrophenolicus*, grows at 35 °C and is a typical Gram-positive, obligate-aerobic bacterium. This species is present in soil, water, and undergrade environments and on the skin of humans and other animals (Kocur et al. 1972; Ventura et al., 2007; Rdzanek et al., 2015). Generally, *M. luteus* is considered a non-pathogenic saprophyte, but some strains may occasionally act as opportunists. For example, this species can cause septic arthritis, pneumonia, urinary tract infection in an immune-deficient person, meningitis, and native and prosthetic valve endocarditis (Kocur et al., 1972; Fosse et al., 1985).

Other bacterial species isolated from the air a short distance from hibernating bats are mainly considered as saprophytic organisms, but in some situations can be pathogenic. For example, *Dermacoccus nishinomiyaensis* is found in water and on the skin of mammals and is considered to be non-pathogenic (Kocur et al., 1975). However, according to recent reports, this species can cause wound infections (Shah et al., 2015). Generally, *Pseudomonas oryzihabitans* is described as a saprophyte of humans and other warm blooded animals (Giacometti et al., 1998; Molinari et al., 2003). In recent years, a nosocomial pathogenic potential has been discussed, because infections usually occur in cases referring to contaminated catheters, peritoneal dialysis, bacteremia, or even sepsis patients (Lucas et al., 1994; Verhasselt et al., 1995; Marín et al., 2000). Thus, *P. oryzihabitans* infection is strongly associated with presence of bacterial biofilms, previous trauma or surgery, and immunocompromised hosts. Reports of its pathogenic potential in humans are rare (Lin et al., 1997). *Micrococcus yunnanensis* is a novel actinobacterium that was isolated from surface-sterilized plants (Zhao et al., 2009). It is likely that it is an endophytic bacterium, which naturally colonizes the internal tissue of plants (Pisarska and Pietr, 2015). *Paenibacillus polymyxa*, formerly known as *Bacillus polymyxa*, is a plant growth promoting rhizobacterium that is used for the biocontrol of plant diseases (Ash et al., 1993; Dijksterhuis et al, 1999). For example, it is used against the plant-parasitic nematodes, and phytopathogenic fungi (Caruso et al., 1984). Additionally, this species is antagonistic to human pathogenic bacteria and fungi *in vitro* (Seldin et al., 1999). *Pseudomonas stutzeri* is a typical soil bacterium that is widely distributed in the environment (Lalucat et al., 2006). It can be an opportunistic

**Table 3. Phenotypic analysis and supplementary diagnostic test results of airborne bacteria isolated in the Nietoperek bat reserve.**

| Characteristic | ***Dermacoccus nishinomiyaensis*** UWR_Bak5 | ***Micrococcus luteus*** UWR_Bak7 | ***Micrococcus yunnanensis*** UWR_Bak4 | ***Paenibacillus polymyxa*** UWR_Bak8 | ***Paeniglutamicibacter psychrophenolicus*** UWR_Bak1 | ***Paeniglutamicibacter sulfureus*** UWR_Bak2 | ***Pseudomonas oryzihabitans*** UWR_Bak6 | ***Pseudomonas stutzeri*** UWR_Bak3 |
|---|---|---|---|---|---|---|---|---|
| Colonies on AN at 25 °C | | | | | | | | |
| Color | Orange-Yellow | Yellow | Bright Yellow | Pale White | Yellowish-Grey | Yellowish-Grey | Non-Pigment | Pale Yellow |
| Diameter (mm) after 48 h | 1.0 | 0.5 | 1.0 | 1.0 | 1.0–2.0 | 1.0–2.0 | 3.0 | 2.0–3.0 |
| Shape | Circular, entire, convex, smooth, glistening, non-transparent. | Circular, entire, convex, smooth, non-glistening, non-transparent. | Circular, entire, convex, smooth, non-glistening, non-transparent. | Flate, smooth glistening, non-transparent. | Circular, entire, convex, smooth, glistening, non-transparent. | Circular, entire, convex, smooth, glistening, non-transparent. | Flate, transparent non-glistening slightly wrinkled. | Flate, transparent non-glistening slightly wrinkled. |
| Bacteria Cell | | | | | | | | |
| Shape | Spherical | Spherical | Spherical | Rod-Like | Rod-Like | Rod-Like | Rod-Like | Rod-Like |
| Arrangement | Irregular Clusters | Tetrads | Tetrads | Clusters | Pleomorphic | Pleomorphic | Single | Single |
| Gram Stain | Positive | Positive | Positive | Positive | Positive | Positive | Negative | Negative |
| Growth Temperature | | | | | | | | |
| 25 °C | + | + | + | + | + | + | + | + |
| 35 °C | + | + | + | + | – | – | + | + |
| Growth in NB with 12.5 % NaCl | – | + | – | – | – | – | – | – |
| Growth Condition[a] | OA | OA | OA | FA | OA | OA | A | OA |
| Susceptibility to Agents[b] | | | | | | | | |
| Bacitracin 10UI | S | S | S | R | S | S | R | R |
| Furazolidone 100 µg mL$^{-1}$ | R | R | R | R | R | R | R | R |

Symbols: AN – nutrient agar; NB – nutrient broth; S – sensitive; R – resistance; "+" growth; "–"no growth;
a Type of growth condition: "A" as aerobic, "OA" as obligate aerobe, "FA" as facultative anaerobe;
b Disk Diffusion Assay

**Table 4. Biochemical properties of airborne bacteria isolated in the Nietoperek bat reserve (Symbols of reaction: "+" positive, "−" negative).**

| Characteristic | *Dermacoccus nishinomiyaensis* UWR_Bak5 | *Micrococcus luteus* UWR_Bak7 | *Micrococcus yunnanensis* UWR_Bak4 | *Paenibacillus polymyxa* UWR_Bak8 | *Paeniglutamicibacter psychrophenolicus* UWR_Bak1 | *Paeniglutamicibacter sulfureus* UWR_Bak2 | *Pseudomonas oryzihabitans* UWR_Bak6 | *Pseudomonas stutzeri* UWR_Bak3 |
|---|---|---|---|---|---|---|---|---|
| Production of: | | | | | | | | |
| Catalse | + | + | + | + | + | + | + | + |
| Oxidase | + | + | − | − | − | − | − | + |
| Acetylmethylcarbinol | − | − | − | + | − | − | − | − |
| Indole | − | − | − | − | − | − | − | − |
| Enzymes | | | | | | | | |
| Urease | + | + | − | − | + | + | − | − |
| Nitrogenase | − | − | − | + | − | − | + | + |
| Nitrate reduction | − | − | − | + | + | − | − | + |
| Arginine ihydrolase | − | − | − | − | − | − | − | − |
| Alkaline hosphatase | − | + | + | − | − | − | − | − |
| α-glucosidase | − | + | + | + | + | + | − | − |
| β-glactosidase | − | − | − | + | − | − | − | − |
| β-glucosidase | − | − | − | + | − | − | − | − |
| Hydrolysis of: | | | | | | | | |
| Skimmed Milk | + | + | − | + | − | − | − | − |
| Gelatine | + | − | + | + | − | − | − | − |
| Starch | − | − | − | + | − | − | − | + |
| Tween80 | − | − | + | + | − | − | − | + |
| Utilization of: | | | | | | | | |
| Glucose | + | − | + | + | − | + | + | + |
| Trehalose | + | + | + | + | + | + | + | − |
| Arabinose | + | − | − | + | − | − | + | − |
| Lactose | − | − | − | + | − | − | − | − |
| Mannose | − | + | + | + | − | − | + | − |
| Mannitol | − | − | − | + | + | + | + | + |
| Maltose | + | + | + | + | + | + | + | + |
| Sucrose | − | + | − | + | − | − | − | − |
| Gluconate | − | − | − | + | + | + | + | + |
| N-acetyl-β-glucosamine | − | − | − | + | − | − | − | − |
| Citrate | − | − | − | − | + | + | + | + |
| Capric acid | − | − | + | − | − | − | + | + |
| Adipic acid | − | − | + | − | − | − | − | − |
| Malic acid | − | − | + | − | + | + | + | + |
| Phenylacetic acid | − | − | + | − | + | − | − | − |
| Trehalose | + | + | + | + | + | + | + | − |

pathogen for humans, however, *P. stutzeri* infection is rare (Noble and Overman, 1994; Reisler and Blumberg, 1999). Under certain circumstances, these bacterial species could act as potential opportunists affecting the health status of individual bats such as in individuals that are weakened by disease or malnutrition or have been traumatized by martens or cats or during the flight.

## Conclusions

This study is the first that describes cultivable airborne bacteria present in the environment of hibernating bats. Bacterial communities showed differences in terms of composition and abundance among the different parts of the Nietoperek underground corridors, and bacterial growth was dependent on the incubation temperature of samples as well as on the number of bats. Results indicate that indoor air samples contained more propagules of bacteria and more bacterial species than outdoor air samples. Moreover, hibernating bats may be good vectors of bacteria in underground sites because more species of airborne bacteria were isolated from the samples in close vicinity to them. *Actinobacteria* dominated in this study. *Paeniglutamicibacter psychrophenolicus* was isolated most frequently from samples incubated at 7° C, and *Micrococcus luteus* from samples incubated at 37 °C. Some of the species found in the study can cause opportunistic infections in humans and animals. To better understand the microbial composition and relevance of specific bacteria, further investigations in underground sites could provide more insights into the complex ecosystems and should be regularly performed.

## Acknowledgments

Thanks to Professor Dr. Hab. Gabriela Bugla-Płoskońska from University of Wroclaw (Poland) for the first reading of the manuscript and critical remarks. Research funding was provided by the Ministry of Science and Higher Education carried out by the University of Wroclaw “Grant to Young Researchers”. Award Number: 0420/2557/18.

## References

Ash, C., Priest, F.G., and Collins, M.D., 1993, Molecular identification of rRNA group 3 bacilli (Ash, Farrow, Wallbanks and Collins) using a PCR probe test. Proposal for the creation of a new genus *Paenibacillus*: Antonie van Leeuwenhoek, v. 64, p. 253–260.

Banskar, S., Bhute, S.S., Suryavanshi, M.V., Punekar, S., and Shouchea, Y.S., 2016, Microbiome analysis reveals the abundance of bacterial pathogens in *Rousettus leschenaultii* guano: Scientific Reports, v. 6, article 36948. http://dx.doi.org/10.1038/srep36948.

Barton, H.A., Taylor, M.R., and Pace, N.R., 2004, Molecular phylogenetic analysis of a bacterial community in an oligotrophic cave environment: Geomicrobiology Journal, v. 21, p. 11–20.

Caruso, F.I., Zuck, M.G., and Bessette, A.E., 1984, Bacterial seedling blight of tomato caused by *Bacillus polymyxa*: Plant Disease, v. 68, p. 617–620. http://dx.doi.org/10.1094/PD-68-617.

Chelius, M.K., Beresford, G., Horton, H., Quirk, M., Selby, G., Simpson, R.T., Horrocks, R., and Moore, J.C., 2009, Impacts of alterations of organic inputs on the bacterial community within the sediments of Wind Cave, South Dakota, USA: International Journal of Speleology, v. 38, no. 1, p. 1–10. http://dx.doi.org/10.5038/1827-806X.38.1.1.

Dijksterhuis, J., Sanders, M., Gorris, L.G.M., and Smid, E.J., 1999, Antibiosis plays a role in the context of direct interaction during antagonism of *Paenibacillus polymyxa* towards *Fusarium oxysporum*: Journal of Applied Microbiology, v. 86, p. 13–21. http://dx.doi.org/10.1046/j.1365-2672.1999.t01-1-00600.x.

Directive 92/43/EEC (1992) The Conservation of Natural Habitats and of Wild Fauna and Flora, European Commission, 1992, The Habitats Directive, http://ec.europa.eu/environment/nature/legislation/habitatsdirective/index_en.htm [accessed February 18, 2017]

Doyle, J.J., and Doyle, J.L., 1987, A rapid DNA isolation procedure for small quantities of fresh leaf tissue: Phytochemical Bulletin, v. 19, p. 11–15.

Evans, N.J., Bown, K., Timofte, D., Simpson, V.R., and Birtles, R.J., 2009, Fatal borreliosis in bat caused by relapsing fever spirochete, United Kingdom: Emerging Infectious Diseases, v. 15, p. 1331–1333. http://dx.doi.org/10.3201/eid1508.090475.

Fenton, M.B., 1969, Summer activity of *Myotis lucifugus* (Chiroptera: Vespertilionidae) at hibernacula in Ontario and Quebec: Canadian Journal of Zoology, v. 47, p. 597–602. https://doi.org/10.1139/z69-103.

Fosse, T., Peloux, Y., Granthil, C., Toga, B., Bertrando, J., and Sethian, M., 1985, Meningitis due to *Micrococcus luteus*: Infection, v. 13, p. 280–281.

Giacometti, A., Cirioni, O., Quarta, M., Schimizzi, A.M., Del Prete, M.S., and Scalise, G., 1998, Unusual clinical presentation of infection due to *Flavimonas oryzihabitans*: European Journal of Clinical Microbiology & Infectious Diseases, v. 17, no. 9, p. 645–648.

Gupta, P., Reddy, G.S.N., Delille, D., and Shivaji, S., 2004, *Arthrobacter gangotriensis* sp. nov. and *Arthrobacter kerguelensis* sp. nov. from Antarctica: International Journal of Systematic and Evolutionary Microbiology, v. 54, p. 2375–2378. https://doi.org/10.1099/ijs.0.63110-0.

Hamm, P.S., Caimi, N.A., Northup, D.E., Valdez, E.W., Buecher, D.C., Dunlap, C.A., Labeda, D.P., Lueschow, S., and Porras-Alfaro, A., 2017, Western bats as a reservoir of novel *Streptomyces* species with antifungal activity: Applied and Environmental Microbiology, v. 83, article e03057-16. https://doi.org/10.1128/AEM.03057-16.

Hoyt, J.R., Cheng, T.L., Langwig, K.E., Hee, M.M., Frick, W.F., and Kilpatrick, A.M., 2015, Bacteria isolated from bats inhibit the growth of *Pseudogymnoascus destructans*, the causative agent of White-Nose Syndrome: PLOS ONE, v. 10, no. 4, p. e0121329. https://doi.org/10.1371/journal.pone.0121329.

Jones, G., Jacobs, D.S., Kunz, T.H., Willig, M.R., and Racey P.A., 2009, CarpeNoctem: the importance of bats as bioindicators: Endangered Species Research, v. 8, p. 93–115. https://doi.org/10.3354/esr00182.

Juck, D., Charles, T., Whyte, L.G., and Greer, C.W., 2000, Polyphasic microbial community analysis of petroleum hydrocarbon-contaminated oils from two northern Canadian communities: FEMS Microbiology Ecology, v. 33, p. 241–249. https://doi.org/10.1111/j.1574-6941.2000.tb00746.x.

Jurado, V., Laiz, L., Rodriguez-Nava, V., Boiron, P., Hermosin H., Sanchez-Moral, S., and Saiz-Jimenez, C., 2010, Pathogenic and opportunistic microorganisms in caves: International Journal of Speleology, v. 39, no. 1, p. 15–24. http://dx.doi.org/10.5038/1827-806X.39.1.2.

Kim, Young Soo, Kotnala, B., Kim, Young Ho, and Jeon, Yongho, 2016, Biological characteristics of *Paenibacillus polymyxa* GBR-1 involved in root rot of stored Korean ginseng: Journal of Ginseng Research, v. 40, p. 453–461. http://dx.doi.org/10.1016/j.jgr.2015.09.003.

Kocur, M., Páčová, Z., and Martinec, T., 1972, Taxonomic status of *Micrococcus luteus* (Schroeter 1872) Cohn 1872, and designation of the neotype strain: International Journal of Systematic and Evolutionary Microbiology, v. 22, no. 4, p. 218–223. http://dx.doi.org/10.1099/00207713-22-4-218.

Kocur, M., Schleifer, K.H., and Kloos, W.E., 1975, Taxonomic Status of *Micrococcus nishinomiyaensis* Oda 1935: International Journal of Systematic Bacteriology, v. 25, no. 3, p. 290–293. http://dx.doi.org/10.1099/00207713-25-3-290.

Kodama, K., Kimura, N., and Komagata, K., 1985, Two new species of *Pseudomonas*: *P. oryzihabitans* isolated from rice paddy and clinical specimens and *P. luteola* isolated from clinical specimens: International Journal of Systematic and Evolutionary Microbiology, v. 35, no. 4, p. 467–474. http://dx.doi.org/10.1099/00207713-35-4-467.

Kokurewicz, T., 2004, Sex and age related habitat selection and mass dynamics of Daubenton's bats *Myotis daubentonii* (Kuhl, 1817) hibernating in natural conditions: Acta Chiropterologica, v. 6, no. 1, p. 121–144. https://doi.org/10.3161/001.006.0110.

Kokurewicz, T., Bongers, F., Ciechanowski, M., Duvergè, L., Glover, A., Haddow, J., Rachwald, A., Rusiński, M., Schmidt, C., Schofield, H., Wawrocka, K., Willems, W., and Zapart, A., 2014, Bat research and conservation in "Nietoperek" bat reserve (Western Poland), in Lina, P.H.C., and Huson, A.M., eds., Abstracts of the XIII European Bat Research Symposium, September 01-05.2014, Šibenik, Croatia: Zagreb, Croatian Speleological Society, pp. 93–94.

Kokurewicz, T., Ogórek, R., Pusz, W., and Matkowski, K., 2016, Bats increase the number of cultivable airborne fungi in the "Nietoperek" bat reserve in western Poland: Microbial Ecology, v. 72, no. 1, p. 36–48. https://doi.org/10.1007/s0024.

Kretzschmar, F., and Heinz, B., 1995, Social behaviour of a large population of *Pipistrellus pipistrellus* (Schreber, 1774) (*Chiroptera*: *Vespertilionidae*) and some other bat species in the mining-system of a limestone quarry near Heidelberg (South West Germany): Myotis International Journal of Bat Research, v. 32-33, p. 221–229.

Kueneman, J.G., Parfrey, L.W., Woodhams, D.C., Archer, H.M., Knight, R., and McKenzie, V.J., 2014, The amphibian skin-associated microbiome across species, space and life history stages: Molecular Ecology, v. 23, p. 1238-1250. https://doi.org/10.1111/mec.12510.

Lalucat, J., Bennasar, A., Bosch, R., García-Valdés, E., and Palleroni, N.J., 2006, Biology of *Pseudomonas stutzeri*: Microbiology and Molecular Biology Reviews, v. 70, no. 2, p. 510–547. https://doi.org/10.1128/MMBR.00047-05.

Lapage, S.P., Hill, L.R., and Reev, J.D., 1968, *Pseudomonas stutzeri* in pathological material: Journal of Medical Microbiology, v. 1, p. 195–202. https://doi.org/10.1099/00222615-1-2-195.

Larsen. A,, Tao, Zhen., Bullard, S.A., and Arias, C.R., 2013, Diversity of the skin microbiota of fishes: evidence for host species specificity: FEMS Microbiology Ecology, v. 85, p. 483–494. https://doi.org/10.1111/1574-6941.12136.

Lin, Rong-Dih, Hsueh, Po-Ren, Chang, Jen-Chyi, Teng, Lee-Jene, Chang, Shan-Chwen, Ho, Shen-Wu, Hsieh, Wei-Chuan, and Luh, Kwen-Tay, 1997, *Flavimonas oryzihabitans* bacteremia: clinical features and microbiological characteristics of isolates: Clinical Infectious Diseases, v. 24, no. 5, p. 867–873. https://doi.org/10.1093/clinids/24.5.867.

Loveland-Curtze, J., Sheridan, P.P., Gutshall, K.R., and Brenchley, J.E., 1999, Biochemical and phylogenetic analyses of psychrophilic isolates belonging to the *Arthrobacter* subgroup and description of *Arthrobacter psychrolactophilus* sp. nov.: Archives of Microbiology, v. 171, p. 355–363. https://doi.org/10.1007/s002030050.

Lucas, K.G., Kiehn, T.E., Sobeck, K.A., Armstrong, D., and Brown, A.E., 1994, Sepsis caused by *Flavimonas oryzihabitans*: Medicine (Baltimore), v. 73, no. 4, p. 209–214.

Mandal, J., and Brandl, H., 2011, Bioaerosols in indoor environment – A review with special reference to residential and occupational locations: The Open Environmental & Biological Monitoring Journal, v. 4, p. 83–96. https://doi.org/10.2174/1875040001104010083.

Margesin, R., Schumann, P., Spröer, C., and Gounot, A.-M., 2004, *Arthrobacter psychrophenolicus* sp. nov., isolated from an alpine ice cave: International Journal of Systematic and Evolutionary Microbiology, v. 54, p. 2067–2072. https://doi.org/10.1099/ijs.0.63124-0.

Marín, M., García de Viedma, D.C., Martín-Rabadán, P., Rodríguez-Créixems, M., and Bouza, E., 2000, Infection of Hickman catheter by *Pseudomonas* (formerly *Flavimonas*) *oryzihabitans* traced to a synthetic bath sponge: Journal of Clinical Microbiology, v. 38, no. 12, p. 4577–4579.

Mickleburgh, S.P., Hutson, A.M., and Racey, P.A., 2002, A review of the global conservation status of bats: Oryx, v. 36, p. 18–34. https://doi.org/10.1017/S0030605302000054.

Molinari, L.M., de Oliveira Scoaris, D., Bocchi Pedroso, R., de Lucas Rodrigues Bittencourt, N., Nakamura C.V., Ueda-Nakamura, T., de Abreu Filho, B.A., and Dias Filho, B.P., 2003, Bacterial microflora in the gastrointestinal tract of Nile tilapia, *Oreochromis niloticus*, cultured in a semi-intensive system: Acta Scientiarum. Biological Sciences, v. 25, no. 2, p. 267–271.

Mühldorfer, K., Wibbelt, G., Haensel, J., Riehm, J.M., and Speck, S., 2010, *Yersinia* species isolated from bats, Germany: Emerging Infectious Diseases, v. 16, p. 578–580. https://doi.org/10.3201/eid1603.091035.

Noble, R.C., and Overman, S.B., 1994, *Pseudomonas stutzeri* infection: a review of hospital isolates and a review of the literature: Diagnostic Microbiology and Infectious Disease, v.19, p. 51–56. https://doi.org/10.1016/0732-8893(94)90051-5.

Northup, D.E., Melim, L.A., Spilde, M.N., Hathaway, J.J.M., Garcia, M.G., Moya, M., Stone, F.D., Boston, P.J., Dapkevicius, M.L.N.E., and Riquelme, C., 2011, Lava cave microbial communities within mats and secondary mineral deposits: implications for life detection on other planets: Astrobiology, v. 11, p. 601–618. https://doi.org/10.1089/ast.2010.0562.

Ogórek, R., Kozak, B., Lejman, A., Kalinowska, K., and Dyląg, M., 2012, Analiza genetyczna szczepów *Candida albicans* za pomocą techniki RFLP-PCR (Molecular typing of *Candida albicans* isolates using RFLP-PCR): Mikologia Lekarska, v. 9, no. 3, p. 109–114 [in Polish].

Ogórek, R., Pusz, W., Lejman, A., and Uklańska-Pusz, C., 2014, Microclimate effects on number and distribution of fungi in the underground comlex in the Owl Mountains (Góry Sowie), Poland: Journal of Cave and Karst Studies, v. 76, no. 2, p. 146–153. http://dx.doi.org/10.4311/2013MB0123.

Ogórek, R., Dyląg, M., Kozak, B., Višňovská, Z., Tančinová, D., and Lejman, A., 2016a, Fungi isolated and quantified from bat guano and air in Harmanecká and Driny Caves (Slovakia): Journal of Cave and Karst Studies, v. 78, no. 1, p. 41–49. http://dx.doi.org/10.4311/2015MB0108.

Ogórek, R., Višňovská, Z., and Tančinová, D., 2016b, Mycobiota of underground habitats: case study of Harmanecká Cave in Slovakia: Microbial Ecology, v. 71, no. 1, p. 87–99. https://doi.org/10.1007/s00248-015-0686-4.

Pindi, P.K., Manorama, R., Begum, Z., and Shivaji, S., 2010, *Arthrobacter antarcticus* sp. nov., isolated from an Antarctic marine sediment: International Journal of Systematic and Evolutionary Microbiology, v. 60, p. 2263–2266. https://doi.org/10.1099/ijs.0.012989-0.

Pisarska, K., and Pietr, S.J., 2015, Biodiversity of dominant cultivable endophytic bacteria inhabiting tissues of six different cultivars of Maize (*Zea mays* L. ssp. mays) cropped under field conditions: Polish Journal of Microbiology, v. 64, no. 2, p. 163–170.

Rampelotto, P.H., 2013, Extremophiles and extreme environments: Life (Basel), v. 3, no. 3, p. 482–485. https://doi.org/10.3390/life3030482.

Rdzanek, M., Pusz, W., Gębarowska, E., and Pląskowska, E., 2015, Airborne bacteria and fungi in a coal mine in Poland: Journal of Cave and Karst Studies, v. 77, no. 3, p. 177–82.

Reisler, B.R., and Blumberg, H., 1999, Community-Acquired *Pseudomonas stutzeri* vertebral osteomyelitis in a previously healtyh patient: case

report and review: Clinical Infectious Diseases, v. 29, p. 667–669. https://doi.org/10.1086/598650.

Seldin, L., Silva de Azevedo, F., Alviano, D.S., Alviano, C.S., and de Freire Bastos, M.C., 1999, Inhibitory activity of *Paenibacillus polymyxa* SCE2 against human pathogenic microorganisms: Letters in Applied Microbiology, v. 28, p. 423–427. https://doi.org/10.1046/j.1365-2672.1999.00563.x.

Shah, P., Ostwal, K., Jadhav, A., and Shaikh, N., 2015, Post hysterectomy wound infection by *Dermacoccus nishinomiyaensis* – a first case report in India: European Journal of Biomedical and Pharmaceutical Sciences, v. 2, no. 4, p. 329–335.

Smibert, R.M., and Krieg, N.R., 1994, Phenotypic characterization, *in* Gerhardt, P., Murray, R.G.E., Wood, W.A., Krieg, N.R., eds., Methods for General and Molecular Bacteriology: Washington, D.C., American Society for Microbiology, pp. 607–654.

Speakman, J.R., and Racey, P.A., 1989, Hibernal ecology of the pipistrelle bat: energy expenditure, water requirements and mass loss, implications for survival and the function of winter emergence flights: Journal of Animal Ecology, v. 58, p. 797–813. https://doi.org/10.2307/5125.

Stella, M., and Suhaimi, M., 2010, Selection of suitable growth medium for free-living diazotrophs isolated from compost: Journal of Tropical Agriculture and Food Science, v. 38, no. 2, p. 211–219.

Stibor, M., Potockỳ, M., Picková, A., Karasová, P., Russell, N.J., and Králová, B., 2003, Characterization of cold-active dehydrogenases for secondary alcohols and glycerol in psychrotolerant bacteria isolated from Antarctic soil: Enzyme and Microbial Technology, v. 32, p. 532–538. https://doi.org/10.1016/S0141-0229(02)00339-3.

Teixeira, L.C.R.S., Peixoto, R.S., Cury, J.C., Sul, Woo Jun, Pellizari, V.H., Tiedje, J., and Rosado, A.S., 2010, Bacterial diversity in rhizosphere soil from Antarctic vascular plants of Admiralty Bay, maritime Antarctica: The ISME Journal, v. 4, p. 989–1001. https://doi.org/10.1038/ismej.2010.35.

Vanderwolf, K.J., Malloch, D., McAlpine, D.F., and Forbes, G.J., 2013, A world review of fungi, yeasts, and slime molds in caves: International Journal of Speleology, v. 42, no. 1, p. 77–96. http://dx.doi.org/10.5038/1827-806X.42.1.9.

Veikkolainen, V., Vesterinen, E.J., Lilley, T.M., and Pulliainen, A.T., 2014, Bats as reservoir hosts of human bacterial pathogen, *Bartonella mayotimonensis*: Emerging Infectious Diseases, 20(6), 960–967. http://dx.doi.org/10.3201/eid2006.130956.

Ventura, M., Canchaya, C., Tauch, A., Chandra, G., Fitzgerald, G.F., Chater, K.F., and van Sinderen, D., 2007, Genomics of actinobacteria: tracing the evolutionary history of an ancient phylum: Microbiology and Molecular Biology Reviews, v. 71, no. 3, p. 495–548. http://dx.doi.org/10.1128/MMBR.00005-07.

Verhasselt, B., Claeys, G., Elaichouni, A., Verschraegen, G., Laureys, G., and Vaneechoutte, M., 1995, Case of recurrent *Flavimonas oryzihabitans* bacteremia associated with an implanted central venous catheter (Port-A-Cath): assessment of clonality by arbitrarily primed PCR: Journal of Clinical Microbiology, v. 33, no. 11, p. 3047–3048.

Vilas, R.A., 2016, Ecological and economical impact of bats on ecosystem: International Journal of Life Sciences, v. 4, no. 3, p. 432–440.

Weisburg, W.G., Barns, S.M., Pelletier, D.A., and Lane, D.J., 1991, 16S Ribosomal DNA amplification for phylogenetic study: Journal of Bacteriology, v. 173, no. 2, p. 697–703. http://dx.doi.org/10.1128/jb.173.2.697-703.

Woźniak C., 1996, History and architecture of the undergrounds of the Międzyrzecki Rejon Umocniony, *in* Kokurewicz, T., ed., The Nature of the Gorzow Voyvodeship (1996). Bat reserve “Nietoperek”: Gorzow Wielkopolski, Voyvodeship Fund for Environment Protection and Water Management, pp. 78–113.

Zang, Emerson., Brandes, S., Tovar, M., Martin, K., Mech, F., Horbert, P., Henkel, T., Figge, M.T., and Roth, M., 2013, Real-time image processing for label-free enrichment of Actinobacteria cultivated in picolitre droplets: Lab on a Chip, v. 13, p. 3707–3713. http://dx.doi.org/10.1039/C3LC50572C.

Zhao, Guo-Zhen, Li, Jie, Qin, Sheng, Zhang, Yu-Qin, Zhu, Wen-Yong, Jiang, Cheng-Lin, Xu, Li-Hua, and Li, Wen-Jun, 2009, *Micrococcus yunnanensis* sp. nov., a novel actinobacterium isolated from surface-sterilized *Polyspora axillaries* roots: International Journal of Systematic and Evolutionary Microbiology, v. 59, p. 2383–2387. http://dx.doi.org/10.1099/ijs.0.010256-0.

James C. Currens. Hypothesized mechanism for the initiation of soil cavities and subsequent cover-collapse in karst terrain. *Journal of Cave and Karst Studies*, v. 80, no. 4, p. 172-180. DOI:10.4311/2016ES0148

# HYPOTHESIZED MECHANISM FOR THE INITIATION OF SOIL CAVITIES AND SUBSEQUENT COVER-COLLAPSE IN KARST TERRAIN

James C. Currens

Abstract

Cover collapse is the unpredictable collapse of unconsolidated earth material over soluble bedrock. In Kentucky, cover collapse costs an estimated $20 to $60 million annually. The Kentucky Geological Survey began keeping a catalog of case histories in 1997 and now receives about 24 reports a year. A total 354 cover-collapse sites were evaluated for this paper, which reports on efforts to discover a relationship between what can be seen (or other otherwise measured) of cover-collapse at the surface and what is happening in the subsurface. The evaluation of measurements made of the cover collapses found 45 % are underlain by Ordovician age carbonates, 41 % are on Mississippian rocks, and 13 % are underlain by Silurian-Devonian stratigraphy. Diameter, elongation (asymmetry ratio), and Riley Sphericity (circularity) were calculated from the length and width of the collapse opening. Distribution of the data is log normal. The diameter of the collapses average 2.4 m. Student's T-tests resulted in a significant difference in depth between collapses underlain by Mississippian versus Silurian-Devonian carbonates. Collapses on Mississippian rocks have large differences in the variance for asymmetry, circularity, and diameter when compared to the variance for Ordovician and Silurian-Devonian cover-collapses. Only 7 % of the cover-collapse sites occur within larger, pre-existing sinkholes. During evaluation of these correlations, it was observed that the cumulative count of cover-collapse per calendar month follows an annual cycle. Collapses are at a minimum in February, but increase to a maximum in July. The count begins to decrease in August and continues to decline through December into January. It is suggested that the air temperature is an important component of the cover-collapse process, possibly accelerating drying of the soil cover, resulting in subsequent collapse.

## Introduction

The Kentucky Geological Survey (KGS) has been accumulating data on the timing and location of cover collapse sinkholes since 1997 (Currens, 2012). The original purpose of this investigation was to document these features and identify any trend in the accumulated data that correlated with an above-ground, more easily observed, parameter. This paper reports on efforts to discover a relationship between what can be seen (or otherwise measured) of cover-collapse at the surface and what is happening in the subsurface. For a less technical reference and additional detail on karst in Kentucky see Currens, 2002.

An assemblage of a large data set, to which the analytical methods could be applied, took 19 years. The data collection was limited in scope to sinkholes in Kentucky. Approximately half of the recent sites documented in the field for this paper were documented by the land owner via an online form. The additional information gathered from the owner is important and is notably valuable when digital photographs are included. Although the data set is the largest of its kind in Kentucky and now contains over 354 reports on file as of September, 2015, it is thought to represent only a fraction of the collapse events that have occurred since the KGS began keeping records.

Cover-collapse damage is distributed widely across Kentucky and frequently damaged buildings, roads, utility lines, and farm equipment (Fig. 1). It has killed livestock, including some thoroughbred horses, and has injured people. In Kentucky, cover collapse costs an estimated $20 to $60 million annually (Dinger, Zourarakis, and Currens, 2007). Of the nearly 4 million people that live in Kentucky, 2.94 million people or 67% lived on karst in 2010 (Cecil, 2015, Department of Environmental and Earth Sciences, University of Kentucky). One of the more expensive collapse events was the Corvette Museum in February 12, 2004, which cost $3.2 million to repair and the damage to the automobiles was an additional $3.1 million (Kambesis et al, 2003).

## Geologic Setting

Kentucky karst is developed on extensive outcrops of carbonate bedrock representing vast ranges in geologic age, distinct mineralogy and characteristic primary sedimentary structures. Of a total of 354 cover collapse sites, 41 % are underlain by Mississippian age (Lower Carboniferous) carbonates, whereas 45 % and 13 %, respectively, are underlain by Ordovician and Silurian-Devonian rocks. The geology of 1 % of the sites is undetermined. The sites are located on 32 different, formal stratigraphic units and the distribution parallels the exposed carbonate area of each geologic system (Fig. 1).

University of Kentucky, Kentucky Geological Survey, Retired, 504 Rose Street, 228 Mining and Mineral Resources Building, Lexington, Kentucky, U.S.A.
Corresponding author: tbcjcc@gmail.com

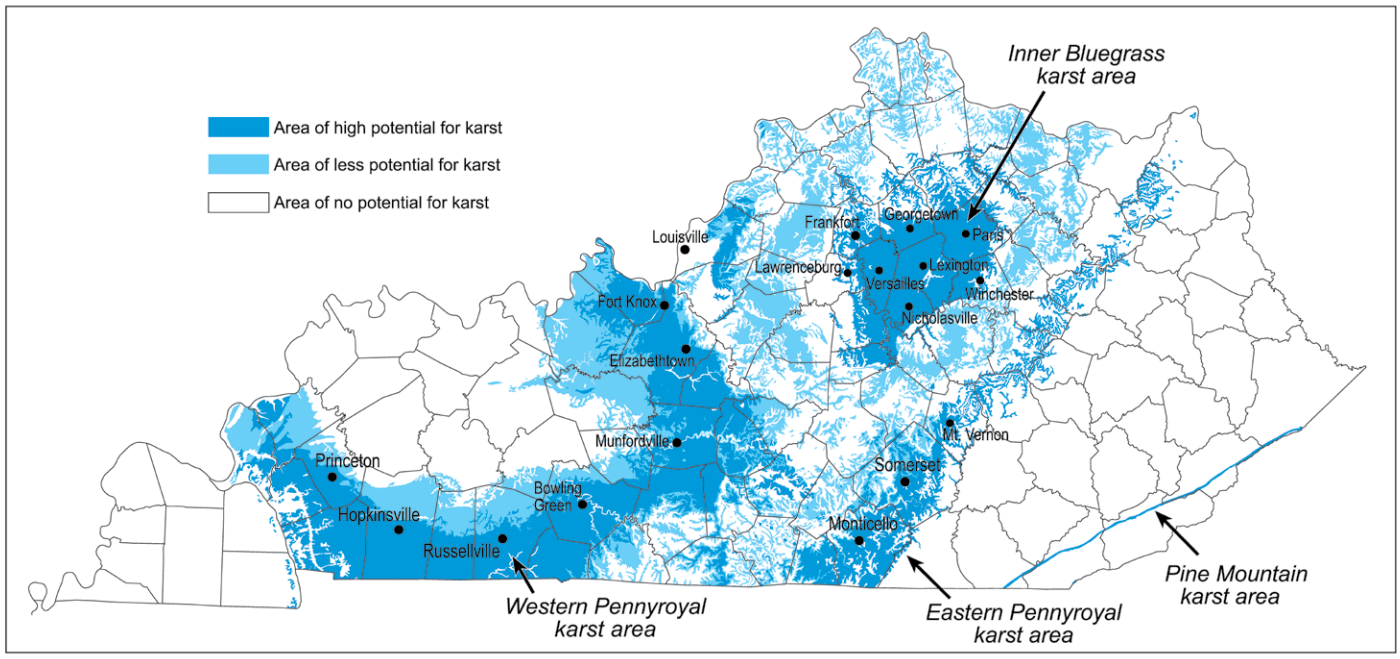


Figure 1. Kentucky karst occurrence map. Darker blue areas have a higher density of karst features.

Karst development is largest in the Western Pennyroyal area, which forms an arc from the Ohio River, near Fort Knox, south to the state's southern border, then west past Hopkinsville and north again back to the Ohio River (Fig. 1). The Western Pennyroyal is underlain by Mississippian (Lower Carboniferous) carbonates with an aggregated thickness up to 150 m. Mississippian strata dip toward the Illinois basin and have hundreds of meters of Upper Mississippian and Pennsylvanian (Upper Carboniferous) deposits covering them in the center of the basin. Karst development is limited to the outcrop on the basin margins.

The Inner Bluegrass occurs in the central part of Kentucky. Lower to middle Ordovician limestones are draped over the Cincinnati Arch, a regional structural high. The Kentucky River has cut through the thick bedded, lower Ordovician, creating kilometers of near vertical cliffs flanking the river. Some of the deepest caves and vertical shafts in Kentucky are found in this region.

Geologically similar, the Eastern Pennyroyal and the Carter Caves area karst is developed in Mississippian limestones, which crop out along the margin of the Appalachian Basin and on the Carter Caves arch. The karst is aerially extensive and some of the longest caves in the state are found in the Eastern Pennyroyal. East and south of Louisville, the Scottville lowland is developed on Silurian and Devonian limestones and dolostone. Although the karst development is somewhat subdued, the area is known for frequent cover collapse.

Finally, there is the Pine Mountain area, created by the Hercynian orogeny, when compressive forces drove the deeply buried rocks to the surface along a fault that was partly parallel with the bedding. There are no communities in this area and cover collapse is seldom reported (Fig. 1).

## Previous Research

There are six basic types of karst sinkholes (White, 1988, Waltham et al., 2005, Ford and Williams, 2007, Gutierrez, et al., 2008): solution (of bedrock), soluble bedrock collapse, (insoluble) cap rock collapse, cover collapse (also called dropout), suffusion, and buried. Of the six types of sinkholes, cover-collapse sinkholes are one of the most destructive, karst-related geologic hazards (Sowers, 1996). The process leading to the development of voids in unconsolidated material overlying karstic bedrock has been thought to be well understood for many years (White, 1988, White and White, 1992, White and White, 1999, Tharp, 2003). Soluble bedrock is riddled with small conduits (0.05 to 0.25 m). The conduits in the bedrock eventually coalesce in a tributary pattern, confluent with a cave passage. A self-supporting roof of insoluble material (residual chert fragments, silt, loess, disaggregated sandstone, or fluvial sand and gravel) spans the growing void in the cover collapse (Currens et al., 2012).

Tharp (2003) has modeled cover collapse development and found that soil plasticity is a critical component. He also found plasticity of the cover in the immediate vicinity of the void decreases. Thus, the initiation of a cover collapse has been attributed to a loss of cohesion and surcharge loading from a wetting front (which results in a hydrostatic load),

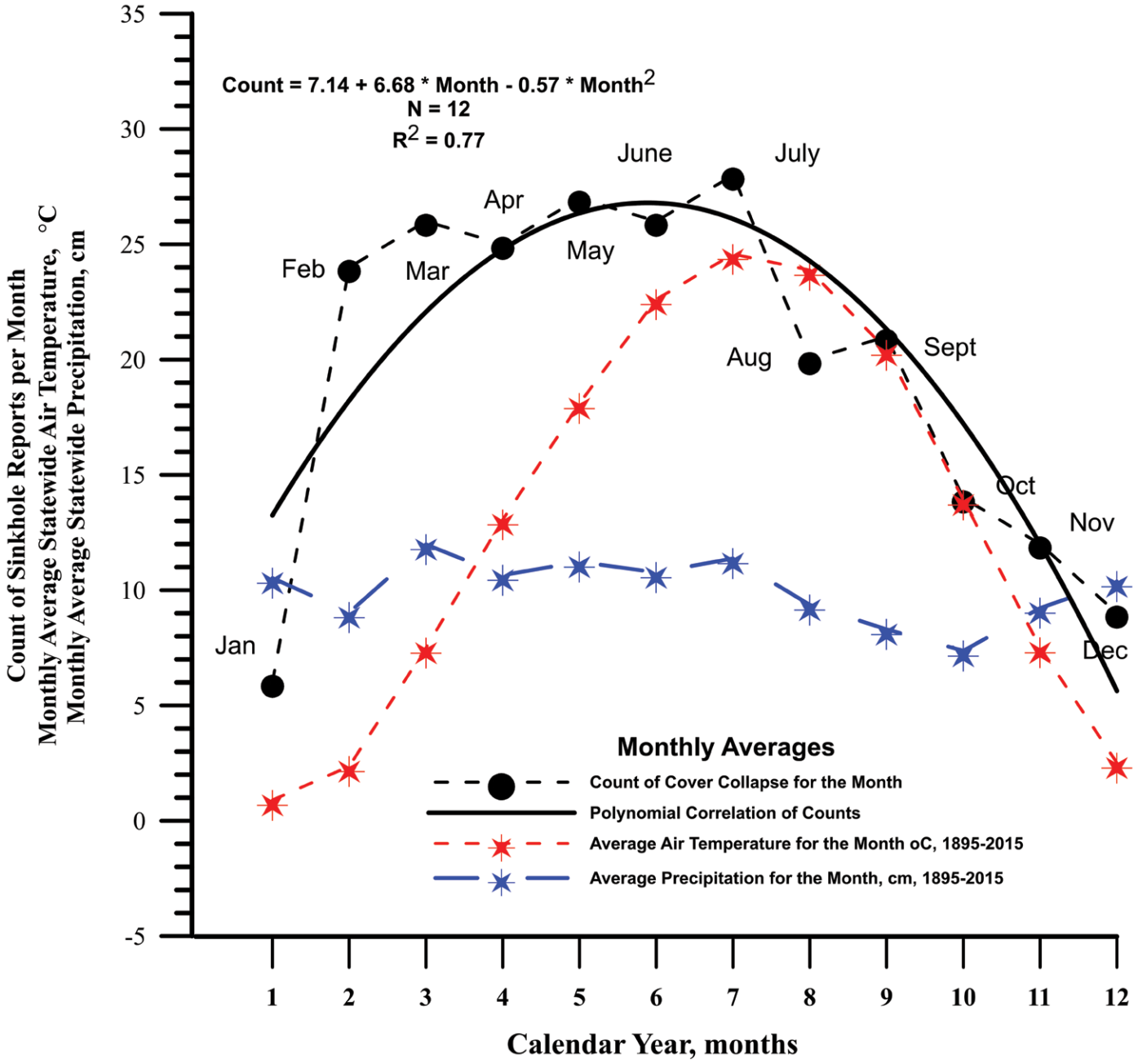


Figure 2. Relationship for the count of cover collapse per month to the average monthly state-wide precipitation and to air temperature.

and due to fracturing of the cover arch, loss of strength (Tharp, 1999). The spalling of layers of soil from the arch interior reduces the head gradient and may re-stabilize the arch until the next recharge event (Tharp, 1999).

Hyatt and Jacobs (1996) studied the geometry of 312 new sinkholes, resulting from a 500-year return-frequency flood along the Flint River in Georgia. The flooding occurred following 53 cm of rain in 19 hours from Tropical Storm Albert in July, 1994. Their findings noted that the new sinkholes had nearly circular outlines at the intersection with the surface and an apparent lack of influence by the regional jointing orientation. In the southeast United States, the elongation index (asymmetry ratio) ranges from 1.0 to 2.3 (Beck, 1991). Hyatt and Jacobs (1996) also noted closely-spaced clusters of new sinkholes in Georgia as a result of the riverine flooding. The relationship between older sinkholes and historic, documented cover collapse has also been studied by Hyatt, Wilkes and Jacobs (1999). They found that older sinkholes tended to be weakly clustered in groups, as opposed to randomly distributed. Their concluding remark, however, stated that nearest-neighbor analysis indicated that “the vast majority of new sinkholes have not clustered around old ones.” Precipitation is thought to influence the timing and rate of cover collapse development (Tharp, 1999). In fields and woodlands, where recharge is slowed, and initially more evenly distributed over the surface by the canopy, grass land, or vegetative litter on the forest floor, the areal distribution of collapse is seemingly random.

Development of analytical models to describe the dynamics and flux of heat and fluid (air, water, $CO_2$) flow in the epikarst and the overlying cover have been evaluated (Covington, 2016). Permeability of the cover and its thickness relative to the epikarst are an important, limiting constraint on air flow between the karst subsurface and the surface. "If there is a thick, relatively [speaking], cover then this will shut down chimney-effect air flow within the fracture network below it" (Covington, 2016). By reciprocity then, if the cover has a sufficient number of interconnected macropores, air flow would be concentrated along those efficient routes, and the cover material adjacent to the macropores would experience more frequent wetting and drying cycles.

## Methods

### Data Description

The list of data gathered by KGS for each collapse was modified from the work of Wilson (Wilson and Shock, 1996). Parameters were omitted or added as thought relevant to the geology of Kentucky. When a call or email was received, often a decision had to be made as to whether the sinkhole report was credible enough to drive hundreds of miles to visit the collapse site. If the owner of the sinkhole could fill out the reporting form available online and attach digital photographs, the decision could be made much easier. The KGS online form includes the following fields:

Location:
Longitude and Latitude, dms
Longitude and Latitude, decimal
Elevation
7½ minute, topographic quadrangle
County

Date: Year, season, month, day, hour
Of occurrence
Of report

Dimensions
Length, width, total depth
Azimuths of principal axes
Description of side-slope angle
General Shape
Sketch of cross-section and plan

Hydrologic Setting
Depth to water, if visible
Bedrock exposed
Depth to bedrock

General description of antecedent weather conditions
Soil name or type

## Calculated Parameters

Length and width of the opening and the azimuth of the principal axes were measured at ground level. Unfortunately, the length and azimuth of the principal axis of the collapse were one parameter that was frequently omitted from the data on the form by property owners and other non-geologists filing a report. The diameter, elongation index (asymmetry ratio), and Riley Sphericity (proxy for circularity index) are calculated from the lengths of the long and short axis.

Circularity index can be conceptualized as the ratio of the areas of two circles, one of which has an imperfect outline, divided by that of a perfect circle (Montero and Bribiesca, 2009). The two area values are defined as having an equal diameter. Brinkmann et al., (2008) describe a circularity index they used for sinkholes in Hillsborough, Florida as comparing the diameter and area of a sinkhole with the area of a circle of the same diameter as the sinkhole. But no equation is provided and no source for the circularity is cited by Brinkmann et al.

Another circularity index is written as $C = P^2/4A$, where P is the perimeter of the sinkhole and A is the area of a circle (Montero and Bribiesca, 2009). The area of the sinkhole has to be measured independently to use either of the indices cited above. The majority of features described in this paper are frequently too new to be included in available photography and, further, are too small to be found on the same. An alternative method was needed. The Riley Sphericity (Folk, 1974) was used, where the $D_c$ is the diameter of the smallest circle circumscribing the collapse and $D_i$ is the diameter of the largest inscribed circle. By substituting the axis length for the diameters, $C = \sqrt{}$ (short axis/long axis), that is used in this paper.

Although the depth is also an important parameter, the true depth of the cover collapse can seldom be measured because the bottom of void is typically obscured by the pile of soil and vegetation from the collapse of the arch. The overall depth of any cover collapse is constrained by relatively thin soils over the carbonate bedrock in the karst areas of Kentucky.

### Statistical Analysis

Statistical analysis consisted of descriptive statistics, population testing with Student's T-tests, and GIS correlation. Multiple-variable analyses were also conducted to confirm results of the Student's *t*-tests. The analysis was conducted

**Table 1. Descriptive statistics for cover collapse reported in Kentucky.**

| Parameters | Sample Size | Arithmetic Mean | Standard Deviation of Arithmetic Mean | Maximum | Geometric Mean |
|---|---|---|---|---|---|
| Length of long axis (m) | 219 | 2.74 | 3.85 | 45.72 | 0.25 |
| Length of short axis (m) | 219 | 1.85 | 2.73 | 32.31 | 0.08 |
| Observable Depth (m) | 201 | 2.32 | 2.58 | 18.9 | 0.21 |
| Diameter, $(L + W)/2$ (m) | 250 | 2.38 | 3.42 | 39.01 | 0.19 |
| Asymmetry, $(L/W)$ | 219 | 1.96 | 2.11 | 10.6 | 0.17 |
| Circularity, $\sqrt{(L \times S)/L^2}$ | 152 | 0.84 | 0.21 | 1.0 | −0.14 |

with Excel spreadsheet, ArcGIS software and Statgraphics Centurion XVI software. Data were grouped based on the stratigraphy and the length, width, observable depth, diameter, elongation (asymmetry), and the circularity were tested for normal distribution and the equivalency of the mean. All of the data have a logarithmic distribution and all further analyses on these data were on transformed data (Table 1). Additional analyses were performed on the data set that had been characterized as an urban setting versus a rural setting.

### Weather Data

Historical weather data from 1895 to 2015 were obtained from the University of Kentucky, College of Agriculture, AgWeatherCenter http://wwwagwx.ca.uky.edu/. Air temperature and precipitation depth was available as a statewide average for the month. An attempt was made to find data for soil temperature at any depth, dating at least to the turn of the 19th Century, but the soil-temperature data do not extend far enough into the past. I also contacted the Kentucky Climate Center at the Western Kentucky University in an attempt to locate detailed (daily or weekly) precipitation totals for an observation station nearest to the site of each cover collapse. Although detailed precipitation data were available for some sites, and a significant percentage of the data were compiled by Western Kentucky University, the amount of time needed to find and compile the entire subset of the data set exceeded the available resources. The KGS took an alternative approach and reviewed the data set again to find collapse events with a date accurate to the month of the collapse or better, resulting in 243 records. The records with a date accurate to the month were tallied irrespective of year and paired with average statewide precipitation for the calendar month.

## Results

### Cover Collapse Dimensions

Among the data sets tested by *t*-test (length, width, observable depth, diameter, elongation index [asymmetry ratio], circularity [Riley Sphericity], and an urban setting versus a rural setting) and multivariate analysis, there were only three statistically different pairs of data means. There is no statistical difference of the mean depth of cover collapse underlain by the Mississippian rocks when compared to the Ordovician carbonates (Table 2). The difference in depth between the collapses over Mississippian and Silurian-Devonian geology may be related to the overall thickness of the cover, and that, in turn, is possibly related to the thickness of the stratigraphic units. The Silurian-Devonian carbonates total 56 m in thickness, whereas the total Mississippian carbonate section ranges in thickness from 102 m to 262 m, as much as a fivefold difference. There was a measurable difference in the depths between the Ordovician (2.4 m) and Siluri-

**Table 2. Summary of results of student's t-test comparison of parameters grouped by geologic period of the underlying bedrock. All data were log transformed.**

| Parameter | Mississippian vs. Ordovician | Mississippian vs. Silurian-Devonian | Ordovician vs. Silurian-Devonian | Urban vs. Rural |
|---|---|---|---|---|
| Depth | *f*-test: M = O<br>*t*-test: M = O | *f*-test: M = S-D<br>*t*-test: M ≠ S-D | *f*-test: O = S-D<br>*t*-test: O = S-D | *f*-test: U = R<br>*t*-test: U = R |
| Diameter | *f*-test: M ≠ O<br>*t*-test: M ≠ O | *f*-test: M ≠ S-D<br>*t*-test: M ≠ S-D | *f*-test: O ≠ S-D<br>*t*-test: O ≠ S-D | *f*-test: U = R<br>*t*-test: U ≠ R |
| Elongation (Asymmetry) | *f*-test: M ≠ O<br>*t*-test: M ≠ O | *f*-test: M = S-D<br>*t*-test: M ≠ S-D | *f*-test: O = S-D<br>*t*-test: O ≠ S-D | *f*-test: U ≠ R<br>*t*-test: U ≠ R |
| Riley Sphericity (Circularity) | *f*-test: M ≠ O<br>*t*-test: M ≠ O | *f*-test: M ≠ S-D<br>*t*-test: M ≠ S-D | *f*-test: O = S-D<br>*t*-test: O ≠ S-D | *f*-test: U = R<br>*t*-test: U ≠ R |

Note: All comparisons are to a 95 % ($\alpha = 0.05$) confidence interval. *t*-test is the student's *t*-test of the equivalency of the means. *f*-test tests the equivalency of the variance. The ≠ symbol indicates the comparison of the two samples is statistically different. The = symbol indicates the two sample sets are not statistically different. M is Mississippian, O is Ordovician, and S-D is Silurian-Devonian. U is urban and R is rural.

an-Devonian (1.6 m) cover-collapse, but this is not statistically significant. The means for elongation index (asymmetry ratio) were not the same for Mississippian versus the Silurian-Devonian or the Ordovician versus the Silurian-Devonian, although the variance was equal. The only other parameter that was found to have similar variance was the circularity (Riley Sphericity) for the Ordovician versus the Silurian-Devonian, but the means of this data set were not equal.

The relationship of recent cover collapses, which were free of anthropomorphic-generated debris, to the anecdotal oral history to the contrary (e.g., there is trash in every sinkhole) was surprising. The presence of buried trash re-exposed by recent collapse strongly indicates the feature had been known for some time (years) before being filled. If the sinkhole was filled with clean rock and soil, unless there is other evidence it is reactivated, it could be assumed to be new. If this information is coupled with the findings of Hyatt (Hyatt, Wilkes, and Jacobs, 1999), which suggests that new cover collapse does not preferentially form near older sinkholes, then the relationship of new cover collapse to larger, mapped sinkholes becomes more difficult to resolve.

**Weather**

Anthropomorphic accentuation of runoff from impermeable surfaces, such as parking lots, is a common cause of collapse in urbanized areas. There are case histories in this database that involve seemingly inconsequential water sources, such as onsite sewage disposal, drips from a leaking gutter, downspouts discharging next to a foundation, and even air conditioner condensate.

The average monthly precipitation data for Kentucky from 1895 through 2015 was plotted against the number of sinkholes per month and fitted with a linear regression. The correlation coefficient was 0.56 at $\alpha = 0.05$. The comparatively weak correlation is thought to be produced by the average precipitation being too generalized. A polynomial regression drawn through all 12 monthly counts, versus precipitation, shows a modest improvement in predicting the counts over the linear regression ($r^2 = 0.77$, $\alpha = 0.05$) (Fig. 2). Because of association of concentrated runoff, the wetter months have been thought to have more frequent incidents of cover collapse.

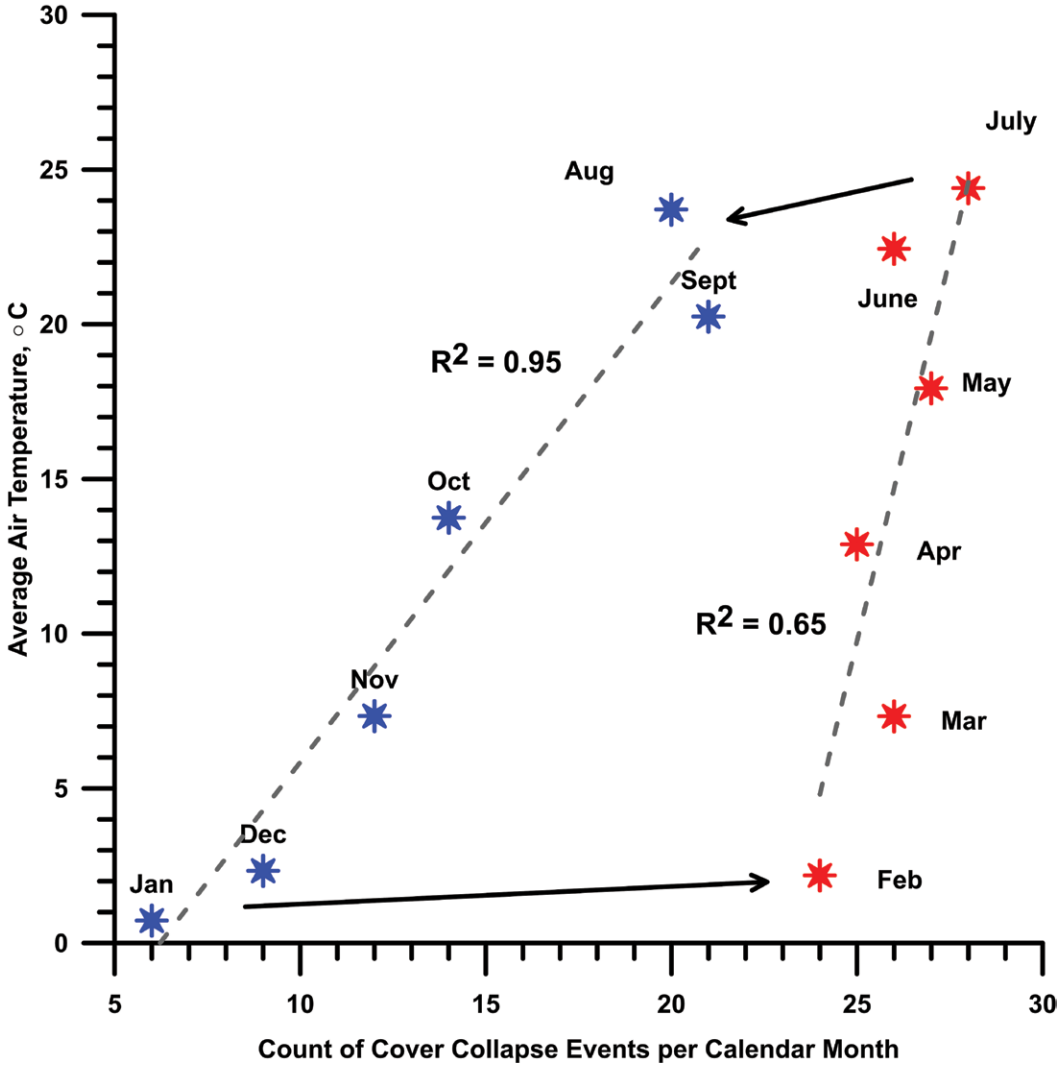


Figure 3. Trend in the tally of collapse per month compared to the monthly average air temperature.

It was also observed that the average monthly temperature and the monthly total of collapse events plotted closer to parallel than had other paired data examined during this study. The data pairs were initially plotted as a single data set with twelve pairs of observations ($r^2 = 0.50$). Then, the data were partitioned into two sub-sets, which revealed a warming period (February through July) and a cooling period (August continuing into January) (Fig. 3). The correlation coefficient of the cooling subset is strongly improved ($r^2 = 0.95$) over the 12-month data set,

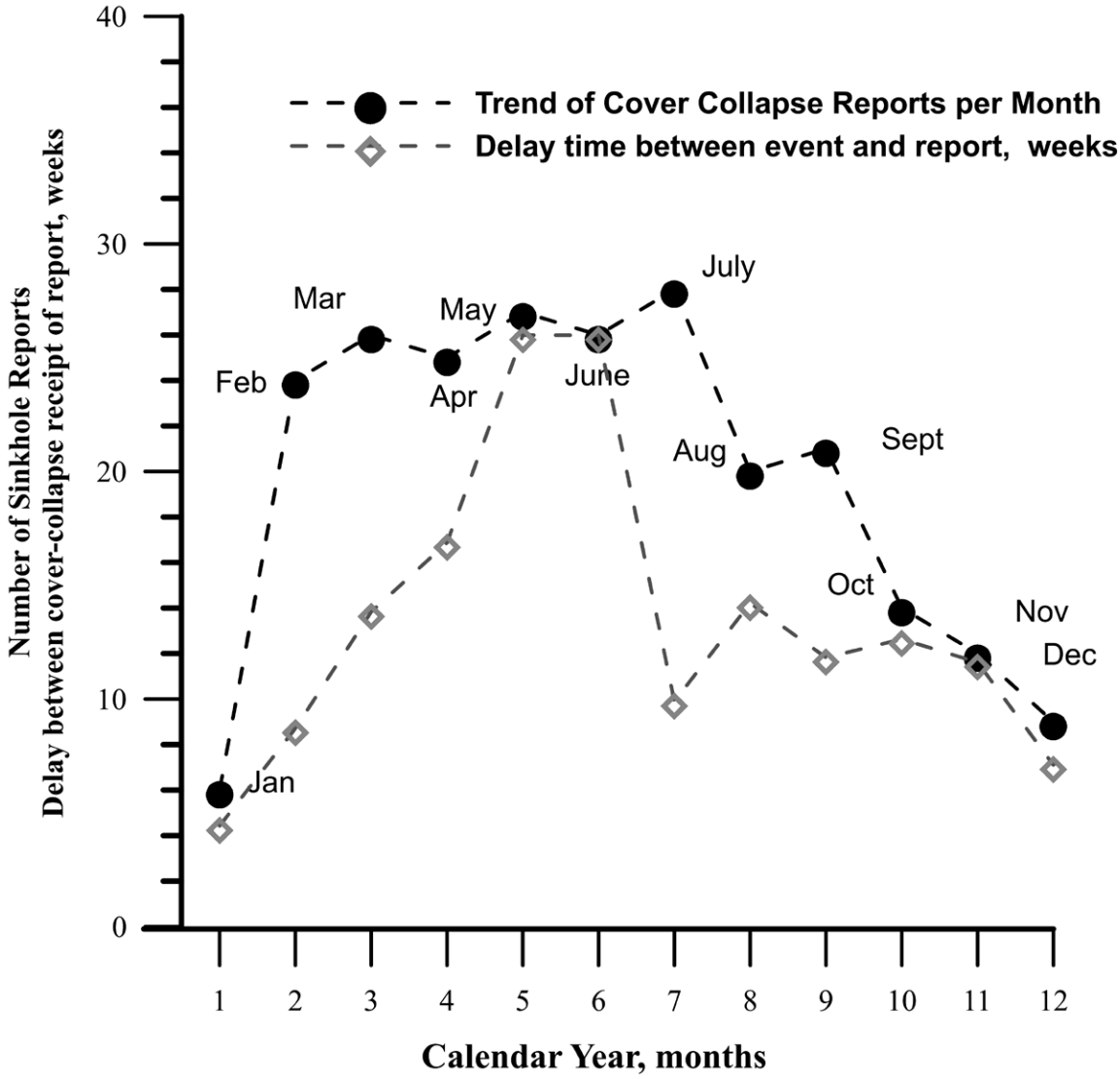


Figure 4. Delay between the estimated date of collapse events and the date of the report, by month.

linear regression, whereas the warming trend sub set also shows a noticeable improvement ($r^2$ = 0.64). These statistics are for the total counts per month for all years, derived from no fewer than six and as many as 28 observations per month. By posting the data in subsets from February to July and August to January, the relationship of the temperature data to the collapse counts became clearer.

The comparatively few reports of collapse in December and January have prompted some criticism (William Andrews, personal communication, 2016). For example, July has six times as many collapses as February. One hypothesis to explain this was that the ground surface could be frozen from November to February. A cold front that results in a short, but especially cold period (temperatures near −10°C) may briefly freeze the soil in the shallow subsurface. When the temperature begins to warm, frozen soil inhibits infiltration of rain or snow melt (Seyfried and Murdock, 1997). Frozen soil would also add mechanical strength to an incipient cover collapse, postponing failure of the arch. Soil frozen more than 5 cm deep is very uncommon in Kentucky.

Another explanation (Drew Andrews, personal communication, 2016) is that there are fewer people actively outside during the winter to find and report a cover collapse. To address this possibility, the data set was reviewed yet again to include 164 data pairs with dates precise enough to determine the period between the event and the report to the nearest week. The graph clearly shows that the longest delays between the event and the report are, except for July, in the late spring and early summer of the calendar year (Fig. 4). The July data are skewed by a physical cluster of cover collapses, which had a similar estimated date of occurrence, a uniform date of the report, and were smaller in diameter than average. All other conditions being equal, the winter months have the shortest delay times between event and report.

In contrast, leafed-out summer foliage hides many of the cover collapse openings. Accounts of farmers driving a tractor across a field of tall crops, hay, or weeds, and driving into an obscured cover collapse that wasn't there the last time the field was harvested, are common. The same cover collapse openings would be relatively visible in the winter. The trend in the delay times strongly suggests that human observation plays a minor role in biasing the cover collapse winter data.

### Air Flow

The warming and cooling trends shown in Figure 4 suggest that above-ground temperatures are either directly involved in the cover collapse mechanism or they are promoting some other process that affects the coherency of the soil void. If air temperature is a direct cause, the air from the surface, driven by the relative density, would flow into the ground during cold weather via a large range of opening sizes (Palmer, 2007). During warm weather the flow direction reverses. The completion of an air flow circuit could explain the development of the soil arch at a specific location. Relatively warm air flowing out in winter would be laden with moisture and would be ineffective at drying the arch materials. Those less common configurations in winter where cold air is flowing into the ground would adsorb a significant mass of moisture as it warms from contact with the soil. The seasonal fall and winter desiccation and springtime wetting of the arch earth materials would eventually trigger a cover collapse.

## Conclusions

The hypothesis developed from this analysis is that the frequency (counts) of cover collapse events per month is related to the air temperature. Soil water infiltrating during the early spring rainy season, followed by air flow drying in the fall and winter, would cause desiccation cracking and spalling of the soil arch. A possible sequence of events leading to a cover collapse are:

1. Water flowing through soil macropores reaches the limestone and enlarges fractures into conduits, enough to allow turbulent flow. At this size of conduit development, discharge may not be great enough to always fill the conduit with water and some air space will become a more common condition. Eventually, all of the water will drain to a lower elevation, and the now air-filled conduit will remain connected to the surface through soil macropores created by recharge.
2. Once the flow path for air becomes established, the spalling process will become more frequent and effective. Each wetting cycle expands the soil void by putting hydraulic pressure on the compressed zone of earth material, forming the most interior band of the arch. If the hydraulic pressure is too great, the interior part of the arch will fail.
3. Each drying cycle creates cracking caused by clay in the wetted ceiling of the soil void, shrinking as the moisture is removed by airflow. Cool, dry air in the fall, its flow direction controlled by air density and the humidity by dry air from the surface, would promote the shrinking of the earth material forming the void ceiling.
4. The arch thins as the void ceiling approaches the surface. The arch becomes too thin for the internal shear strength of the remaining cover to support its own weight and it fails.

The implications of this hypothesis may go well beyond the phenomena of cover collapse. For example, it could have profound implications for the accumulation of radon in basements and crawl spaces of buildings.

Future researchers should attempt to locate and instrument a soil void well before it collapses. The research plan would begin with locating as many soil voids as possible that are at various depths. A protocol to install a variety of instrumentation would be needed to test the hypothesis. The equipment needed would include: an access port for a downhole camera, a small-diameter well for collecting water samples, if appropriate, access for two pressure transducers, a temperature sensor, and a relative humidity probe.

## Acknowledgements

The support of the Kentucky Geological Survey at the University of Kentucky is gratefully acknowledged. Dr. Stuart A. Foster, State Climatologist for Kentucky, Kentucky Climate Center at Western Kentucky University researched the site-specific precipitation data. Thanks to Mr. Chuck Taylor for his advice and encouragement.

## References Cited

Beck, B.F., 1991, On calculating the risk of sinkhole collapse, in Kasting, E.H., and Kasting, K.M., eds., Appalachian Karst, proceedings of the Appalachian Karst Symposium, Radford, Va., March 23-26, 1991: National Speleological Society, Huntsville, Ala., p. 231–236.

Brinkmann, R., Parise, M., and Dye, D., 2008, Sinkhole distribution in a rapidly developing urban environment: Hillsborough County, Tampa Bay area, Florida; Engineering Geology, v 99, p 169-184. https://doi.org/10.1016/j.enggeo.2007.11.020.

Cecil, M.C., 2015, Population and land use in Kentucky karst regions: independent study final report, Departments of Earth and Environmental Studies, Department of Geography, and Kentucky Geological Survey, 15 p.

Covington, M.D., 2016, The importance of advection for $CO_2$ dynamics in the karst critical zone: an approach from dimensional analysis *in* Feinberg, J. M., Gao, Yungli, and Alexander, E.C., Jr., eds., Caves and Karst Across Time, Special Paper 519: Boulder, Colo., Geological Society of America, p. 113-–127.

Currens, J.C., 2002, Kentucky is karst country! What you should know about sinkholes and springs: Kentucky Geological Survey, Ser. 12, IC 4, 29 p.

Currens, J.C., 2012, Cover-collapse sinkholes in Kentucky, USA: geographic and temporal distribution: carbonates and evaporites, v. 27, p. 137-142. https://doi.org/10.1007/s13146-012-0097-2.

Currens, J.C., Paylor, R.L., Beck, G.E. and Davidson, B., 2012, A method to determine cover-collapse frequency in the western Pennyroyal karst of Kentucky: Journal of Cave and Karst Studies, v. 74, no.3, p. 292–299. https://doi.org/10.4311/2011ES0247.

Dinger, J.S., Zourarakis, D.P., and Currens, J.C., 2007, Spectral enhancement and automated extraction of potential sinkhole features from NAIP imagery–Initial Investigations: Journal of Environmental Informatics, v. 10, no. 1, p. 22–29. https://doi.org/10.3808/jei.200700096.

Ford, D.C., and Williams P.W., 2007, Karst hydrogeology and geomorphology: Chichester, West Sussex, U.K., John Wiley & Sons, Ltd, 562 p.

Folk, R.L., 1974, Petrology of sedimentary rocks: Austin, University of Texas, Hemphill Publishing Co., 182 p.

Gutierrez, F., Guerrero, J. Lucha, P., 2008, A genetic classification of sinkholes illustrated from evaporite paleokarst in Spain: Environmental Geology, v. 53, p. 993-1006. https://doi.org/10.1007/s00254-007-0727-5.

Hyatt, J.A., and Jacobs, P.M., 1996, Distribution and morphology of sinkholes triggered by flooding following Tropical Storm Alberto at Albany, Georgia, USA: Geomorphology, v. 17, p. 303–316. https://doi.org/10.1016/0169-555X(96)00014-1.

Hyatt, J.A., Wilkes, H.P., and Jacobs, P.M., 1999, Spatial relationships between new and old sinkholes in covered karst, Albany, Georgia, USA, *in* Beck, B.F., Pettit, and Herring, J.G., eds., Hydrogeology and Engineering Geology of Sinkholes and Karst: Rotterdam, Netherlands, Balkema, p. 37–44.

Kambesis, P., Crawford, N., Croft, L.A., Moore, R., and Pfaff, R., 2003, Dishman Lane collapse, Bowling Green, Kentucky, *in* Sinkholes and the Engineering and Environmental Impacts of Karst, Beck, B.F., ed.: Proceedings of the Ninth Multidisciplinary Conference, Geotechnical Publication No. 122, American Society of Civil Engineers, National Groundwater Association, GEO Institute, and P.E. LaMoreaux & Associates, Inc., p. 404–737.

Montero, R.S., and Bribiesca, E., 2009, State of the art of compactness and circularity: International Mathematical Forum, 4, no. 27, p. 1305–1335.

Palmer, A.N., 2007, Cave Geology: Cave Books, Cave Research Foundation, 454 p.

Seal, L. D., 2005, Creation, analysis and evaluation of remote sensing sinkhole databases for Pinellas County, Florida [M.S. Thesis]: Tampa, University of South Florida, Department of Geology, 55 p.

Seyfried, M.S., and Murdock, M.D., 1997, Use of air permeability to estimate infiltrability of frozen soil: Journal of Hydrology, v. 202, p. 95–107. https://doi.org/10.1016/S0022-1694(97)00061-9.

Sowers, G.F., 1996, Building on sinkholes: New York, American Society of Civil Engineers, 202 p. https://doi.org/10.1061/9780784401767.

Tharp, T. M., 1999, Mechanics of formation of sinkholes: Engineering Geology, v.52, p.23–33. https://doi.org/10.1016/S0013-7952(98)00051-9.

Tharp, T. M., (2003). Sinkhole formation and soil plasticity *in* Sinkholes and the Engineering and Environmental Impacts of Karst, Beck, B. F., ed.: Proceedings of the Ninth Multidisciplinary Conference, Geotechnical Publication No. 122, American Society of Civil Engineers, National Groundwater Association, GEO Institute, and P.E. LaMoreaux & Associates, Inc., p. 110–123.

Waltham, T., Bell, F., and Culshaw, M., 2005, Sinkholes and subsidence: karst and cavernous rocks in engineering and construction: New York, Springer-Praxis Books in Geophysical Sciences, 382 p.

White, W.B., 1988, Geomorphology and hydrology of karst terrains: New York, Oxford University Press, p. 387–402.

White, W.B., 1999, Karst hydrology: recent developments and open questions: Proceedings of the 7th Multidisciplinary Conference on Sinkholes and the Environmental Impacts of Karst: Rotterdam, Netherlands, Balkema, p. 3–21.

White, W.B., and White, E.L., 1992, Sinkholes and sinkhole collapses, *in* Majundar, S.K., Forbes, E.W., and Schmalz, R.F., Eds., Natural and technological disasters: Effects and preventative measures: The Pennsylvania Academy of Science, p. 280–293.

Wilson, W.L., and Shock, E.J., (1996). New sinkhole data spreadsheet manual: Winter Springs, Fla., Subsurface Evaluations Inc., version 1.1, 34 p, appendices, 3.5 in diskette.

María Borrego-Ramos, Saúl Blanco, and Adriana Olenici. Diatoms from the Valporquero Cave (León, NW Spain), with the description of *germainiella legionensis* sp. nov. *Journal of Cave and Karst Studies*, v. 80, no. 4, p. 181-189. DOI:10.4311/2017MB0128

# DIATOMS FROM THE VALPORQUERO CAVE (LEÓN, NW SPAIN), WITH THE DESCRIPTION OF *GERMAINIELLA LEGIONENSIS* SP. NOV.

María Borrego-Ramos[1,C], Saúl Blanco[1], and Adriana Olenici[1,2]

Abstract

From a biological point of view, karst caves are important subterranean ecosystems, but remain to date relatively poorly-studied. The diversity in this kind of habitat is usually low due to scarce light availability with resulting lack of primary productivity. In the case of show caves, the artificial illumination allows the colonization by phototrophic microorganisms, which is known as *lampenflora*, including fungi, bacteria, cyanobacteria, chlorophytes, diatoms, mosses, etc. This study analyzes the diatom flora from Valporquero Cave (León, NW Spain), both epilithic on stalactites and moss-dwelling. In the samples observed, typical genera from moist, humid, aerophilous habitats were recorded, but some biogeographically noteworthy species, including an unknown *Germainiella* taxon described here as a new species, were found. Some of these species have already been reported from caves from different places around the world, giving an idea of the broad distribution pattern of many diatom taxa. The occurrence of diatom taxa in this cave could contribute to understanding the global diversity and distribution patterns in cave-dwelling taxa.

## Introduction

Caves are peculiar environments occurring throughout the world, with rather stable climatic conditions and food supplies, except for the entrance zones. Their biological communities include mostly microorganisms, but also worms, snails, arachnids, crustaceans, millipedes, insects, fishes, and salamanders (Holsinger, 1988). In these ecosystems, microorganisms frequently grow as components of entrance biofilms (Hoffmann 2002), where diatoms (Bacillariophyta) can represent around 11% of the total. Previous analysis of biofilms in other caves revealed that these communities were formed by phototrophic microorganisms, including coccal and filamentous cyanobacteria, green unicellular eukaryotic algae, diatoms, bacteria, and fungi (Urzì et al., 2010). The distance from the cave entrance is an important factor influencing the structure of these biofilms (Cuezva et al., 2009; Abdullin, 2011; Coombes et al., 2015).

In show caves, artificial illumination allows for colonization by phototrophic microorganisms, which frequently constitute macroscopic biofilms. Cyanobacteria and Chlorophyta are the first colonizers in caves, and are able to produce exopolymeric substances (EPSs), which are suitable environments for colonization by other microorganisms (Albertano, 1993). The assemblage constituted by these microorganisms is known as *lampenflora* (Dobàt, 1963), and the diversity of *lampenflora* communities has recently been reviewed (Mulec and Kosi, 2009). However, the proliferation of lampenflora is currently considered as the main threat for the conservation of show caves (Grobbelaar, 2000; Piano et al., 2015) and studies related to growth control methods have increased (Mulec et al., 2007), including physical (light control), chemical, and biological methods.

Aerophytic algae can survive in the environment only when the humidity is high enough (Mulec and Kosi, 2009). Diatoms have been found in many types of ecosystems including some in caves (Falasco et al., 2014). The most common genera of diatoms found in these types of environments are *Navicula* and *Diadesmis* (Falasco et al., 2014), together with other aerophilic taxa.

In karst regions, the formation of caves is carried out by rainwater that becomes acidic due to the interaction with carbon dioxide in the atmosphere and soil (Niemiller and Soares, 2015). Natural caves present exceptional characteristics because of their oligotrophic conditions (Holsinger, 1988; Graening and Brown, 2003; Ortiz et al., 2014; Piano et al., 2015), as well as the air temperature, which is influenced by air circulation in the proximity of entrances and it is usually stable in the deepest zones, with minimal daily and seasonal variations (Albertano, 1993). Hydrogeologically active caves show additional particularities that depend on the hydrogeological regime (Milanovic, 2007). In these types of active caves, the presence of running waters can accelerate the growth of biofilms (Mulec and Kosi, 2009). In any case, subterranean environments present relatively homogeneous, simplified natural conditions, and therefore, represent suitable habitats to study communities in relation to several factors and to predict ecological patterns on larger scales (Falasco et al., 2014), such as the effects of climate change.

The present study was carried out in Valporquero Cave (NW Spain), a hydrogeologically active cave, internally crossed by the Valporquero river (Arrese et al., 2007), which is a subterranean stream that flows through the lower level

[1] Department of Biodiversity and Environmental Management, University of León, León, Spain The Institute of the Environment, La Serna Street No. 58 24007, León, Spain.
[2] Faculty of Environmental Sciences and Engineering, Babeș-Bolyai University, 30 Fântânele Street, Cluj-Napoca, 400294, Cluj-Napoca, Romania.
[C]Corresponding Author: mborr@unileon.es

of the cave. We characterize for the first time the diatom flora from this cave. During the research, a novel population of an unknown naviculoid taxon was found, and is described here by means of a detailed light (LM) and scanning electron (SEM) microscopy-based description.

## Materials and Methods

### Study area

The Valporquero Cave (42°54'22"N 5°33'31"W, 1390 m a.s.l.) is located in NW Spain (Fig. 1), and it is considered one of the main karstic environments of the Iberian Peninsula, composed of Carboniferous Barcaliente limestones. The cave has been included under numerous environmental protection statuses, such as Natura 2000 Network (LIC Hoces de Vegacervera) or the Argüellos Biosphere Reserve.

The current appearance of the cave has been modeled by an underground hydrographic network consisting of 3524 m (known to date), of which 1300 m are modified for tourists. The annual average temperature is 7 °C and the relative humidity is around 99% (Cueva de Valporquero, 2017). From a geological perspective, this is still a dynamic cave with active speleogenesis. The Valporquero Cave has been the subject of a number of speleological and geomorphological studies (Barea et al., 1998; Arrese et al., 2007) although the inhabiting biota, apart from the entomofauna (Salgado, 1985; Bastazo et al., 1993; Petitpierre and Gómez-Zurita, 1998) remains unexplored to our knowledge.

### Sampling

Two samples of epilithic algae growing on stalactites and two samples of moss-inhabiting algae in the surroundings of two artificial light lamps were collected in April 2015 and preserved in the field with 10% formaldehyde. Epilithic diatoms were extracted and analyzed following standard methods (EN 14407 2004). Moss-dwelling diatoms were prepared following Van der Werff (1955), diatoms were cleaned by adding 37% $H^2O^2$, and the reaction was completed by addition of saturated KMnO4. Frustules were cleaned with distilled water three times. Permanent slides were mounted for light microscopy using Naphrax (refractive index of 1.74).

Diatoms were identified under 1000X LM with an Olympus BX60 equipped with DIC optics. LM photographs were taken with a Canon EOS400 camera. Greater than 400 individuals (valves) were counted and identified per slide using recent taxonomic references (Hofmann et al., 2011 and references therein). For scanning electron microscopy (SEM), the oxidized samples were filtered through polycarbonate membrane filters with a pore diameter of 1 or 3 µm, mounted on stubs, sputtered with gold (40 nm) with a Modular High Vacuum Coating System (BALZERS SCD 004, Liechtenstein) and studied with a JEOL JSM-6480 LV, operated at 20 Kv. Original and treated samples, together with LM slides and SEM stubs, are permanently stored at the Institute of the Environment (Diatom Lab, University of Leon, Spain, GBIF code 10031). Type material is stored in the LEB Herbarium (University of León, Spain).

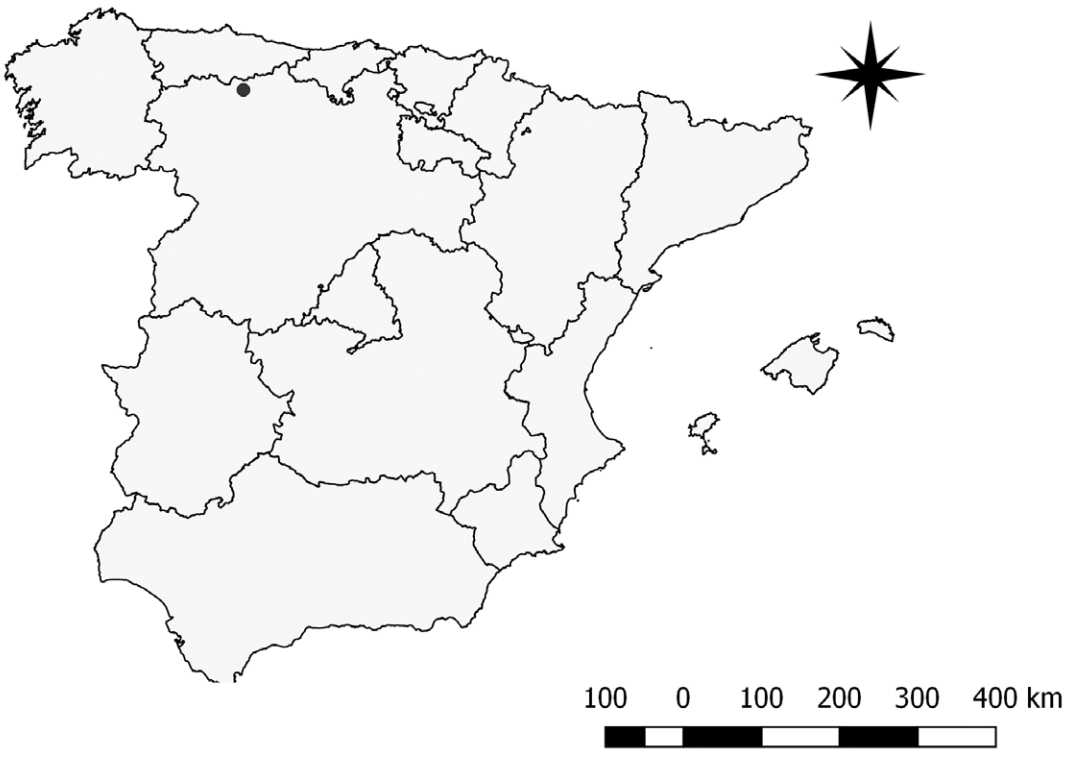


Figure. 1. Geographical location of Valporquero Cave in NW Spain. (QGIS 2017).

## Results and Discussion

A total of 26 diatom taxa were recorded in the samples collected (Table 1). Most of the species identified are common in this type of habitat (Falasco et al., 2014). The most abundant species belong to the genera *Humidophi-*

**Table 1. Checklist of the diatom species and distribution on moss-dwelling and stalactites from Valporquero Cave (León, Spain).**

| Diatom Species | Moss-Dwelling | | Stalactites | |
|---|---|---|---|---|
| | Moss1 | Moss2 | Stal1 | Stal2 |
| *Achnanthidium* F.T. Kützing | + | | | |
| *Achnanthidium rivulare* Potapova & Ponader | | + | | |
| *Adlafia bryophila* (Petersen) Moser Lange-Bertalot & Metzeltin | | + | + | |
| *Cymbopleura rupicola* (Grunow) Krammer var. *rupicola* | | | | + |
| *Diadesmis gallica* Wm. Smith | + | + | + | + |
| *Diploneis krammeri* Lange-Bertalot & Reichardt | | + | | |
| *Diploneis oculata* (Brebisson in Desmazières) Cleve | | + | | + |
| *Encyonopsis microcephala* (Grunow) Krammer | | + | | + |
| *Encyonopsis minuta* Krammer & Reichardt | | + | | |
| *Eolimna minima*(Grunow) Lange-Bertalot | | + | | |
| *Eucocconeis laevis* (Oestrup) Lange-Bertalot | | + | | |
| *Fallacia insociabilis* (Krasske) D.G. Mann | | + | + | + |
| *i =Germainiella legionensis* Blanco, Borrego-Ramos & Olenici | + | + | + | |
| *Halamphora normanii* (Rabenhorst) Levkov | + | + | + | + |
| *Humidophila contenta* (Grunow) Lowe, Kociolek, Johansen, Van de Vijver, Lange-Bertalot & Kopalová | | | + | + |
| *Humidophila dissimilis* (Moser, Lange-Bertalot & Metzeltin) Lowe, Kociolek, Johansen, Van de Vijver, Lange-Bertalot & Kopalová | | + | + | |
| *Humidophila paracontenta* (Lange-Bertalot & Werum) Lowe, Kociolek, Johansen, Van de Vijver, Lange-Bertalot & Kopalová | | + | + | |
| *Humidophila perpusilla* (Grunow) Lowe, Kociolek, Johansen,Van de Vijver, Lange-Bertalot & Kopalová | | + | + | + |
| *Mayamaea cavernicola* Van de Vijver & Cox | | + | + | + |
| *Navicula cataracta-rheni* Lange-Bertalot | | + | | |
| *Nitzschia solgensis* Cleve-Euler | | + | + | |
| *Pinnularia* C.G. Ehrenberg | | + | + | |
| *Pinnularia bartii* Metzeltin & Lange-Bertalot | | + | + | |
| *Sellaphora sp.* C. Mereschkowsky | | + | | |
| *Simonsenia delognei* Lange-Bertalot | + | | | |
| *Tryblionella debilis* Arnott ex O'Meara | + | | + | |

*la, Cymbopleura*, and *Mayamaea.* With the exception of *Cymbopleura rupicola*, all these taxa are already recorded in subterranean ecosystems.

Epilithic diatom assemblages observed in the studied samples were dominated by several *Humidophila* species such as *H. paracontenta* (Lange-Bertalot and Werum) Lowe et al., *H. perpusilla* (Grunow) Lowe et al., *Humidophila dissimilis* (Moser, Lange-Bertalot and Metzeltin) Lowe et al., together with a *Diadesmis* species (D. Wm. Smith), morphologically and ecologically close to *Humidophila*. Other accompanying species such as *Mayamaea, Humidophila,* and *Diadesmis*, are typical genera of moist, humid, aerophilous habitats (Lowe et al., 2014). These genera exhibit the same ecological preferences, and for many years remained under the same genus *Diadesmis*, although recent molecular studies split off both taxa (Andreeva et al., 2016).

The moss-dwelling diatom assemblages presented differences regarding species diversity. One of the samples was dominated by *Mayamaea cavernicola* Van de Vijver and Cox, which had been already found in small caves on Ile de la Possession, the main island of the Crozet Archipelago (the type locality (Van de Vijver et al., 2002), and according to these authors, was recorded in a lava tube cave on the Hawaiian Islands (Rushforth et al., 1984) incorrectly identified as *Navicula seminulum* var. *hustedtii* Patrick). In contrast, the second sample was dominated by *Diadesmis gallica*, which accounted for almost the total abundance.

Many *Diadesmis gallica* were found as teratological forms, as in previous studies in caves (Falasco et al., 2015). Such morphological alterations are considered common in these conditions (Falasco et al., 2015; Lund, 1945, 1946).

Most of the species found in the communities studied belong to the genus *Humidophila,* which is considered to be adapted to low light conditions (Johansen, 2010). This genus has been already reported in other karst habitats in China (Lowe et al., 2017), Spain (Del Rosal, 2016), Canada (Lauriol et al., 2006) Slovakia (Lukešová and Nováková, 2008), and Slovenia (Mulec et al., 2007), and in limestone caves in Oregon, USA (identified as *Navicula,* (St. Clair et al., 1981), and Russia (Abdullin, 2011). It has been also found in other aerophilous habitats from Europe (e.g., Werum and Lange-Bertalot 2004) and the Antarctic region (Van de Vijver et al., 2002).

Another noteworthy species found in our samples is *Pinnularia bartii* Metzeltin and Lange-Bertalot, (Figs. 2 a−f), which had been so far recorded only in the type locality (moss samples in Río de La Plata near Colonia del Sacramento, Uruguay (Metzeltin et al., 2005), with an additional population found in Reunion Island (Metzeltin et al., 2005).

## Species Description

***Germainiella legionensis*** (Figs. 3−5)

Synonyms: ?'*Nupela* sp.' in Zimmerman et al. (2010, fig. 47:10-11), ?'*Achnanthes microcephala*' *sensu* Rushforth et al. (1984, Fig. 21)

**Description:**

Frustules rectangular in girdle view, with a short pervalvar depth (Fig. 4). Valves hyaline under LM with no conspicuous features even under DIC optics, except for the narrow, straight axial area, centrally expanded in a small, roundish central area. Outline linear-lanceolate with strongly capitate apices. Valve length 9.5−10.5 µm, width 2.0−2.5

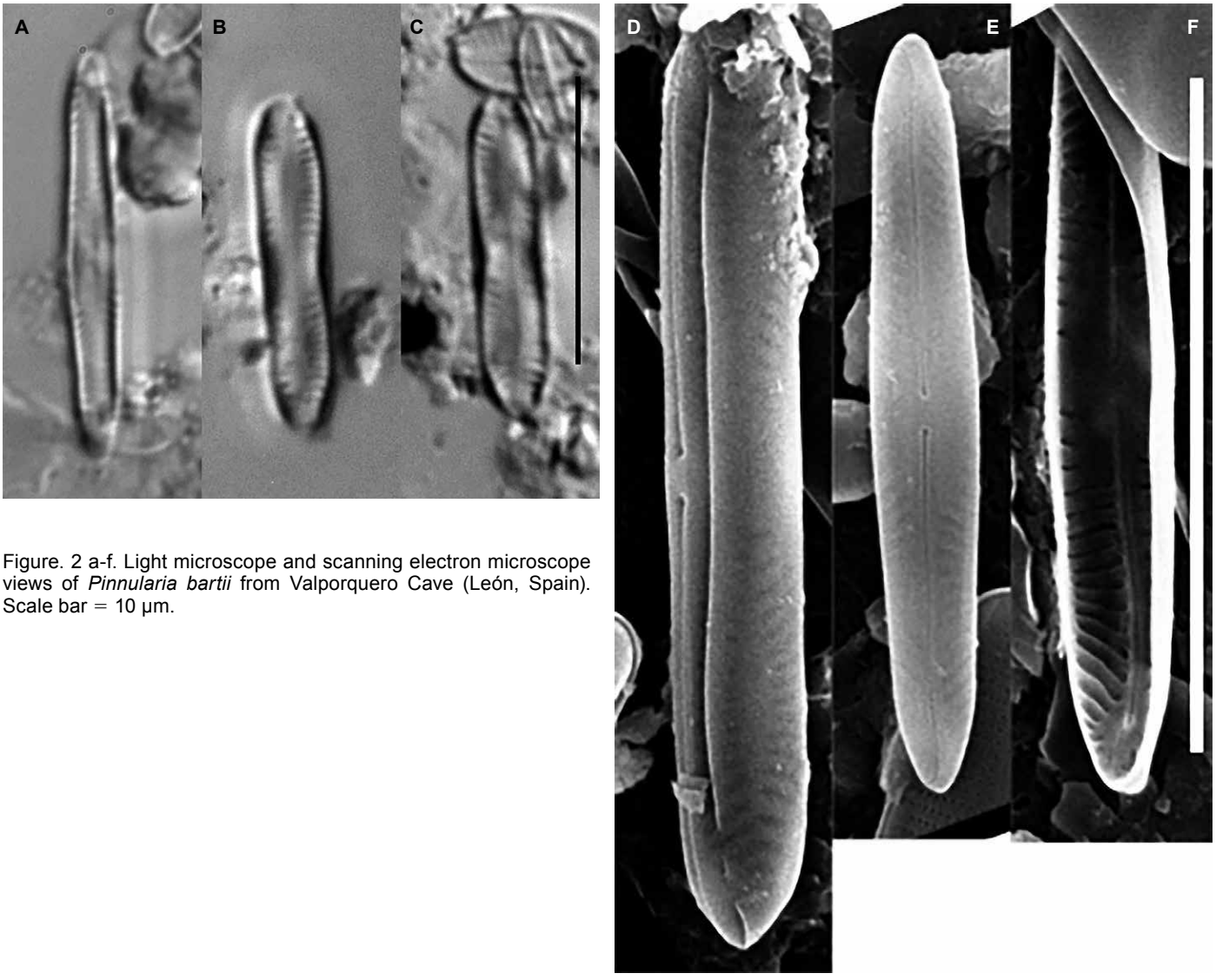


Figure. 2 a-f. Light microscope and scanning electron microscope views of *Pinnularia bartii* from Valporquero Cave (León, Spain). Scale bar = 10 µm.

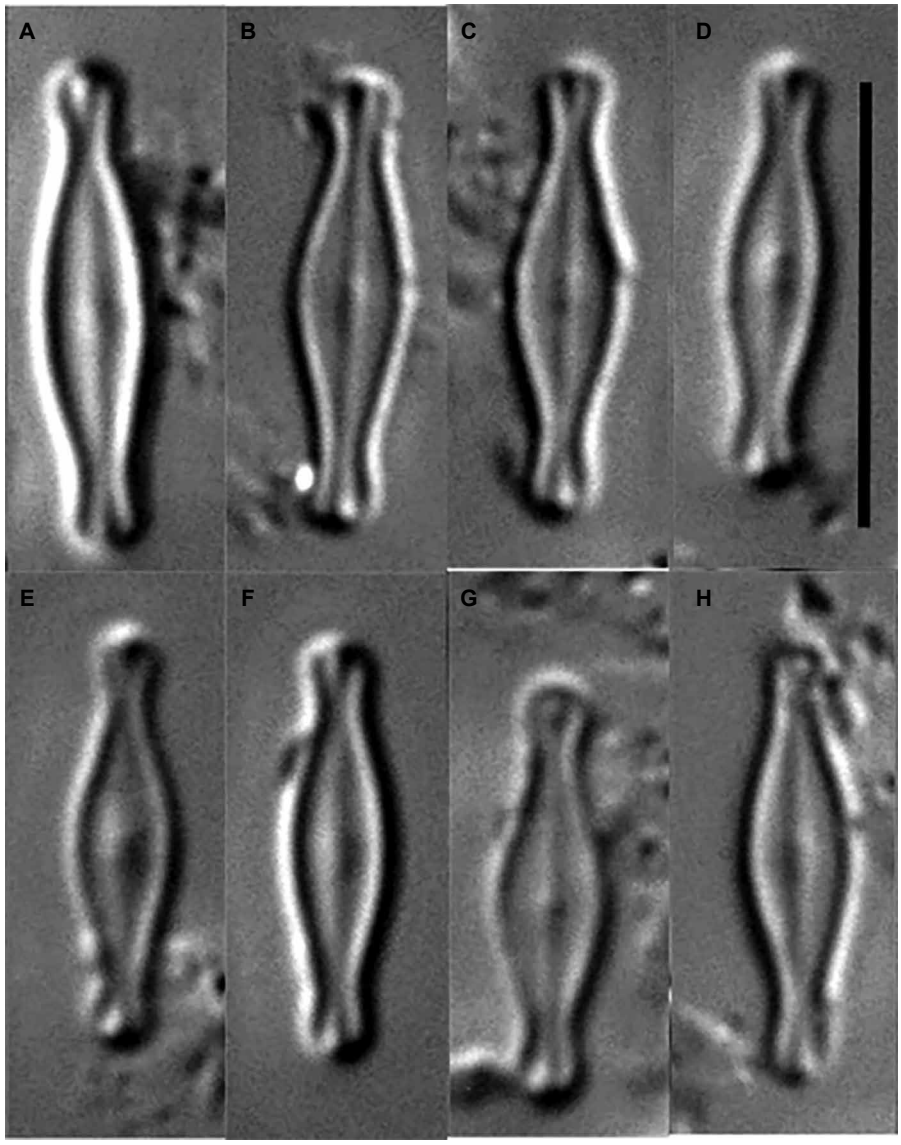


Figure. 3 a-h. Light microscope images of the new diatom taxa *Germaniella legionensis* sp. nov. from Valporquero Cave (NW Spain). Individuals from the holotype specimen. Scale bar 10 µm.

µm, and length to width ratio 4.2−4.7. SEM: Valve covered by a velum which extends towards the mantle, so that the subconopeal space is only open to the exterior through a bilateral slit near the apices (Fig. 5a, arrows). Raphe filiform, straight, with external proximal raphe endings simple, not expanded, slightly bent towards one side of the valve. Distal external raphe endings continuing onto the valve mantle, forming sickle-shaped fissures. Striae visible only in broken valves, composed of a single, transapically expanded areola (Fig. 5b), *ca.* 45 in 10 µm.

**Type**: Valporquero Cave (42°54'22"N 5°33'31"W), León, Spain. Samples collected on 20th March 2016.

**Holotype**: LEB!, microscopic slide 026. Individuals from the holotype specimen are here depicted as **Germainiella legionensis** (Figs. 3−5) **Blanco, Borrego-Ramos & Olenici**

**Etymology**: The epithet of the Species refers to the region where Valporquero Cave is located in León, Spain.

**Ecology**: *Germainiella legionensis* was collected in three samples of the Valporquero Cave, both on a stalactite and on mosses, near artificial light sources. In general, the samples are characterized by a low diversity and low abundance, as is typical in subterranean habitats (Holsinger, 1988; Falasco et al., 2014; Trajano et al., 2016) that could be explained by the particular ecological conditions and the absence of light. Compared to other studies (Falasco et al., 2014; 2015), the richness is relatively low but exhibit interesting species.

**Distribution:** Until now found in living samples in the type locality (Valporquero Cave) in León, Spain, probably also in the Thurston Lava Tube in Hawaii, and in fossil samples from Bylot Island (Canadian Arctic Archipelago), see synonyms.

Differential diagnosis: until recently, only two species had been described within *Germainiella*, the generitype *G. enigmatica* (≡ *Navicula enigmatica* ≡ *Fallacia enigmatica*), presumed to be cosmopolitan (Metzeltin et al., 2005), and the morphologically similar *G. enigmaticoides*, restricted to the type locality (Colonia, Uruguay). In 2016, a third species, *G. clandestina*, was discovered in an artificial freshwater channel inoculated with biofilms from the Garonne River (Le Cohu et al., 2016), to date not referenced elsewhere. The new taxon described here can be easily differentiated in LM from these regarding its outline, with clearly capitated valves exhibiting a narrow neck (and not subcapitate as in *G. enigmaticoides*), and the short pervalvar depth shown in frustules seen in girdle view (compare Fig. 4 with Metzeltin et al., 2005, pl 54: figs 22−27). Moreover, the stria density is the lowest recorded within the genus (ca. 45 in 10 µm and not greater than 50 in 10 µm, (Le Cohu et al., 2016)). The other morphological and morphometric features correspond to those described for *G. enigmaticoides*.

*Germainiella legionensis* may have been earlier identified as *Achnanthes microcephala* in the samples collected in the Thurston Lava Tube, Hawaii, by Rushforth et al. (1984). According to this article, this individual occurred in a com-

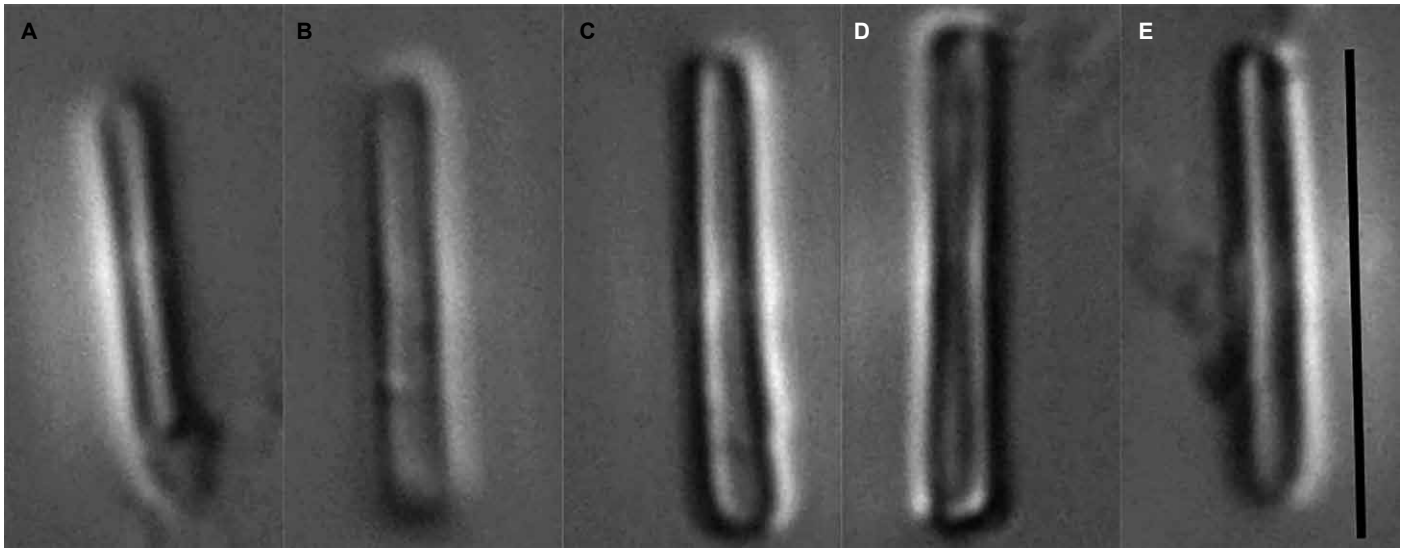


Figure. 4 a-e. Light microscope images of *Germaniella legionensis* in girdle view. Scale bar 10 µm.

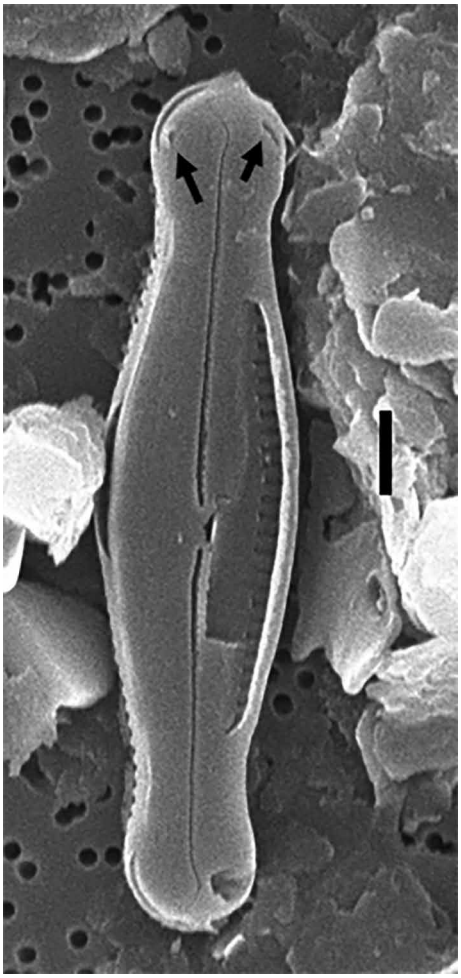

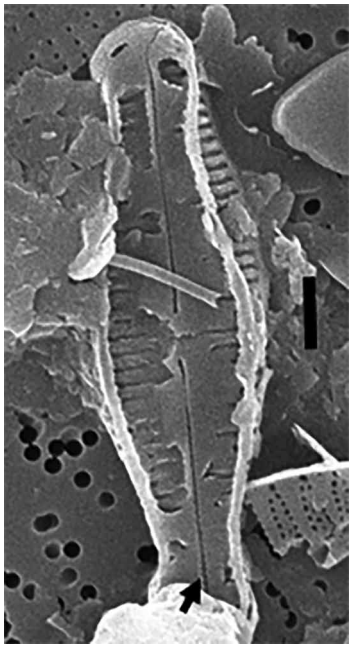

Figure. 5. Scanning electron microscope images of *Germaniella legionensis* sp. nov. Detail of the distal raphe (a) and detail of the single, transapically expanded areolae (b). Scale bar 1 µm.

parable habitat (wet mucilage and bryophytes wall). Additionally, this species is probably present also in late Pliocene sediment samples from Bylot Island (Canadian Arctic Archipelago), under the name *Nupela* cf. *wellneri* (Lange-Bertalot) Lange-Bertalot in Rumrich 2000 (Zimmermann et al., 2010).

**Taxonomical notes:** the ascription of this new species to the genus *Germainiella* can be evidenced regarding the presence of all its characteristic apomorphies (Metzeltin et al., 2005), namely i) a large conopeum that covers the entire valve, including the mantle, and ii) a series of canal apertures externally on either side of the raphe (fig 5b, arrow). Additionally, *Germainiella* frustules bear girdle bands opening at valve center (Liu et al., 2017), a character not seen in our individuals. These features separate *Germainiella* taxa from the closely related genus *Pseudofallacia* (Liu et al., 2012, Le Cohu et al., 2016) but a number of other similar small naviculoid genera have been established recently, all of them bearing a single transapically elongated areola per stria (which does not correspond to the external foramen of an alveolus, as in *Oestrupia*); all of them can be discriminated by paying attention to relatively few characteristics (Table 2). Noteworthy, many of these groups also share their ecological preferences, since *Chamaepinnularia*, *Germainiella*, *Humidophila*, *Microcostatus* and others usually inhabit subaerial, humid habitats, including cave walls.

**Biogeographical remarks**: our observations have raised some important floristic novelties, not only for the Iberian phycoflora, but also with some additions to the cave-dwelling biota recorded to date worldwide (Falasco et al., 2014). Based on the Fenchel et al. (1997) experiment, the theory “everything is everywhere” was first proposed, stating that the microbial species found in a given habitat are a function only of habitat properties and not of historical factors

**Table 2. Key to the identification of small naviculoid diatoms generally with a single external foramen per stria.**

| No. | Character | Genus |
|---|---|---|
| 1 | Areolae covered by a fine membrane | *Biremis* "type 1" *sensu* Witkowski et al. (2014) |
| 1' | Otherwise | 2 |
| 2 | Presence of microcostae along the valve face, conopea and pseudoconopea occur frequently | *Microcostatus* |
| 2' | Otherwise | 3 |
| 3 | Valves covered by a conopeum | 4 |
| 3' | Otherwise | 5 |
| 4 | Conopeum restricted to the valve face | *Pseudofallacia* |
| 4' | Conopeum extended to the valve mantle | *Germainiella* |
| 5 | Proximal raphe ends internally slightly deflected | 6 |
| 5' | Proximal raphe ends internally straight | 7 |
| 6 | Hymenes depressed in internal valve surface, girdle bands perforated | *Microfissurata* |
| 6' | Otherwise | *Chamaepinnularia* |
| 7 | Externally, distal raphe ends reach the mantle | *Pulchella* |
| 7' | Otherwise | 8 |
| 8 | With stigmata | 9 |
| 8' | Otherwise | *Humidophila* |
| 9 | Externally, distal raphe ends T-shaped | *Labellicula* |

(Fenchel and Finlay, 2004), so that their distribution patterns are driven by many features including cell size, dispersion ability, and local or population richness (Fenchel et al., 1997). The absence of biogeographical barriers has been observed in a number of microorganisms, such as Archaea (Whitaker et al., 2003) or Foraminifera, where no genetic differences were found comparing Arctic and Antarctic populations (Darling et al., 2000), as expected in a non-barrier distribution scene. On the other hand, some recent studies have criticized the ubiquity model, e.g. in the case of diatoms, whose dispersal is considered limited in space (Vanormelingen et al., 2008; Vyverman et al., 2007), based on the evidence supporting restricted distribution in the new taxa described, as is the case of *Achnanthes* species in Hawaii, 70% of which are endemic (Lowe et al., 2009). In their study analyzing a global freshwater diatom data set, Vyverman et al. (2007) found evidence in favor of the Theory of Island Biogeography, due to the probable endemism observed in diatom floras in the Southern Hemisphere. In a recent study analyzing the distribution patterns of species within a single genus in the Antarctic Region, Kopalová et al. (2015) found that most *Humidophila* taxa showed restricted biogeographical patterns. In some cases, biogeography has been used to support taxonomic identification of diatoms inhabiting different nearby islands (Van de Vijver et al., 2008). Accordingly, several papers have demonstrated highly-restricted distributions in diatom species inhabiting these islands (Van de Vijver and Beyens, 1999; Van de Vijver et al., 2002, 2008; Van de Vijver and Cox, 2013).

In contrast, Sherwood et al. (2014) carried out a large survey of the Hawaiian Islands analyzing the non-marine algae in targeted areas, such as streams, cave walls, or terrestrial habitats, with molecular methods. These authors deepened the global distribution patterns of forty-four taxa and found only 11.4% endemic species. A similar result was reported by Chattova et al. (2014) in the Ile Amsterdam (TAFF), where only 17% of species were found endemic, and other 14% were species restricted to the sub-Antarctic. In the case of cave diatoms of the Hawaiian Islands, an increasing number of endemic new species are being described (Miscoe et al., 2016); since past studies were mainly based on European floras a few species were newly described.

In view of our results, the occurrence of populations of certain diatom taxa such as *Pinnularia bartii* or *Mayamaea cavernicola* in geographically isolated, very distant regions, but in comparable habitats, may support the ubiquity model. However, the possibility that these populations (Valporquero, Canadian Arctic, and Hawaii for *Germainiella legionensis*) are actually pseudocryptic species (Mann and Evans, 2008) cannot be discarded, although this does not seem likely since these populations share the same ecological preferences, despite the geographical isolation. Currently, new advances in molecular methods are allowing detection of pseudocryptic diversity within diatoms. In the case of cave-dwelling taxa, new studies are needed in order to understand their actual diversity and distribution patterns in these singular ecosystems.

## Acknowledgements

A. Sánchez is thanked for SEM assistance. C. Wetzel (LIST, Luxembourg) and E. Falasco (Turin University) kindly helped us in taxonomic identifications.

## References

Abdullin, S.R., 2011, Effect of illumination on the distribution of phototrophic organisms in the entrance part of the Shul'gan-Tash Cave: Russian Journal of Ecology, v. 42, no. 3, p. 249–251. https://doi.org/10.1134/S1067413611030039

Albertano, P., 1993, Epilithic algal communities in hypogean environments: Plant Biosystem, v. 127, no. 3, p. 386–392. https://doi.org/10.1080/11263509309431020

Andreeva, S.A., Kulikovskiy, M.S., Maltsev, Y.I., Podunai, Y.A., and Gusev, E.S. 2016, Molecular genetic investigation of diatom genera *Diadesmis* and *Humidophila* (Bacillariophyceae): Botanicheskiy Zhurnal, v. 101, no. 6, p. 621–628.

Arrese, B., Durán, J., López-Martínez, J., Altable, O., and Vázquez, J., 2007, Estudio de parámetros ambientales en una cueva hidrogeológicamente activa: la Cueva de Valporquero, *in* Durán, J.J., Robledo, P.A., and Vázquez, J., eds., Cuevas turísticas: aportación al desarrollo sostenible: Madrid, Publicaciones del Instituto Geológico y Minero, Hidrogeología y Aguas Subterráneas, Serie Hidrogeología y Aguas Subterráneas, p. 127–136.

Barea, J., Durán, J.J., Heredia, N., Juliá, R., López-Martínez, J., Quintana, L., and Vallejo, M., 1998, Geomorfología del sistema kárstico de Valporquero (León, Cordillera Cantábrica): Investigaciones recientes de la Geomorfología española, p. 31–38.

Bastazo, G., Vela, J., and Petitpierre, E., 1993, Datos faunísticos sobre Alticinae ibéricos (Col. Chrysomelidae): Boletín de la Asociación española de Entomología, v. 17, no. 1, p. 45–69.

Chattova, B., Lebouvier, M., and Van de Vijver, B., 2014, Freshwater diatom communities from Ile Amsterdam (TAAF, southern Indian Ocean): Fottea: Journal of the Czech Phycological Society, v. 14, no. 1, p. 101–119. DOI: 10.5507/fot.2014.008

Coombes, M.A., La Marca, E.C., Naylor, L.A., Piccini, L., De Waele, J., and Sauro, F., 2015, The influence of light attenuation on the biogeomorphology of a marine karst cave: a case study of Puerto Princesa Underground River, Palawan, the Philippines: Geomorphology, v. 229, p. 125-133. https://doi.org/10.1016/j.geomorph.2014.10.007

Cueva de Valporquero, 2017, http://www.cuevadevalporquero.es [accessed on October 1, 2017]

Cuezva, S., Sanchez-Moral, S., Saiz-Jimenez, C., and Cañaveras, J.C., 2009, Microbial communities and associated mineral fabrics in Altamira Cave, Spain: International Journal of Speleology, v. 38, no. 1, p. 83-92. http://dx.doi.org/10.5038/1827-806X.38.1.9

Darling, K.F., Wade, C.M., Stewart, I.A., Kroon, D., Dingle, R., and Leigh Brown, A.J., 2000, Molecular evidence for genetic mixing of Arctic and Antarctic subpolar populations of planktonic foraminifers: Nature, v. 405, no. 6782, p. 43–47. DOI:10.1038/35011002

Del Rosal, Y., 2016, Análisis, impacto y evolución de los biofilms fotosintéticos en espeleotemas, El caso de la Cueva de Nerja [Ph.D. thesis]: Málaga, Universidad de Málaga, 336 p.

Dobàt, K., 1963, Höhlenalgen" bedrohen die Eiszeitmalereien von Lascaux: Die Höhle, Wien, v. 14, no. 2, p. 41–45.

Falasco, E., Bona, F., Isaia, M., Piano, E., Wetzel, C.E., Hoffmann, L., and Ector, L., 2015, *Nupela troglophila* sp. nov., an aerophilous diatom (Bacillariophyta) from the Bossea cave (NW Italy), with notes on its ecology: Fottea, v. 15, no. 1, p. 1–9. DOI: 10.5507/fot.2015.001

Falasco, E., Ector, L., Isaia, M., Wetzel, C.E., Hoffmann, L., and Bona, F., 2014, Diatom flora in subterranean ecosystems: a review: International Journal of Speleology, v.43, no. 3, p. 231-251. http://dx.doi.org/10.5038/1827-806X.43.3.1

Fenchel, T., Esteban, G.F., and Finlay, B.J., 1997, Local versus Global Diversity of Microorganisms: Cryptic Diversity of Ciliated Protozoa: Oikos, v. 80, no. 2, p. 220–225. DOI: 10.2307/3546589

Fenchel, T., and Finlay, B.J., 2004, The Ubiquity of Small Species: Patterns of Local and Global Diversity: BioScience, v. 54, no. 8, p. 777–784. https://doi.org/10.1641/0006-3568(2004)054[0777:TUOSSP]2.0.CO;2

Graening, G.O., and Brown, A.V., 2003, Ecosystem dynamics and pollution effects in an Ozark cave stream: JAWRA Journal of the American Water Resources Association, v. 39, no. 6, p. 1497–1507. https://doi.org/10.1111/j.1752-1688.2003.tb04434.x

Grobbelaar, J.U., 2000, Lithophytic algae: A major threat to the karst formation of show caves: Journal of Applied Phycology, v. 12, no. 3–5, p. 309–315. https://doi.org/10.1023/A:1008172227611

Hoffmann, L., 2002, Caves and other low-light environments: Aerophytic photoautotrophic microorganisms, in: Bitton, G., ed., Encyclopedia of Environmental Microbiology: New York, John Wiley & Sons, p. 835-843.

Holsinger, J.R., 1988, Troglobites: the evolution of cave-dwelling organisms: American Scientist, v. 76, p. 146–153.

Johansen, J.R., 2010, Diatoms of aerial habitats, *in* Smol, J.P., and Stoermer, E.F., eds., The Diatoms: Applications for the Environmental and Earth Sciences: Cambridge, Cambridge University Press, p. 465-472

Kopalová, K., Kociolek, J.P., Lowe, R.L., Zidarova, R., and Van de Vijver, B., 2015, Five new species of the genus *Humidophila* (Bacillariophyta) from the Maritime Antarctic Region: Diatom Research, v. 30, no. 2, p. 117–131. https://doi.org/10.1080/0269249X.2014.998714

Lauriol, B., Prévost, C., and Lacelle, D., 2006, The distribution of diatom flora in ice caves of the northern Yukon Territory, Canada: relationship to air circulation and freezing: International Journal of Speleology, v. 35, no. 2, p. 83-92. http://dx.doi.org/10.5038/1827-806X.35.2.4

Le Cohu, R., Barthès, A., Leflaive, J., and Ten-Hage, L., 2016, *Germainiella clandestina* sp. nov. (Bacillariophyta), a new species in a little known diatom genus: Fottea, Olomouc, v. 16, no. 2, p. 184–188. DOI: 10.5507/fot.2016.005

Liu, B., Williams, D.M., and Ou, Y., 2017, *Adlafia sinensis* sp. nov. (Bacillariophyceae) from the Wuling Mountains Area, China, with reference to the structure of its girdle bands: Phytotaxa, v. 298, no. 1, p. 43–54. DOI: http://dx.doi.org/10.11646/phytotaxa.298.1.4

Liu, Y., Kociolek, J.P., Fan, Y., and Wang, Q., 2012, *Pseudofallacia* gen. nov., a new freshwater diatom (Bacillariophyceae) genus based on *Navicula occulta* Krasske: Phycologia, v. 51, no. 6, p. 620–626. https://doi.org/10.2216/11-098.1

Lowe, R., Kociolek, J.P., You, Q., Wang, Q., and Stepanek, J., 2017, Diversity of the diatom genus *Humidophila* in karst areas of Guizhou, China: Phytotaxa, v. 305, no. 4, p. 269–284.

Lowe, R.L., Kociolek, P., Johansen, J.R., Van de Vijver, B., Lange-Bertalot, H., and Kopalová, K., 2014, *Humidophila* gen. nov., a new genus for a group of diatoms (Bacillariophyta) formerly within the genus *Diadesmis*: species from Hawai, including one new species: Diatom Research, v. 29, no. 4, p. 351–360. https://doi.org/10.1080/0269249X.2014.889039

Lowe, R.L., Sherwood, A.R., and Ress, J.A., 2009, Freshwater Species of *Achnanthes* Bory from Hawaii: Diatom Research, v. 24, no. 2, p. 327–340. https://doi.org/10.1080/0269249X.2009.9705805

Lukešová, A., and Nováková, A., 2008, Interactions between soil micro-flora and invertebrates in Slovak and Moravian caves, *in* Central European Workshop on Soil Zoology, 9th, České Budějovice.

Lund, J.W.G., 1945, Observations on Soil Algae: Part I. New Phytologist, v. 44, no. 2, p. 196–219.

Lund, J.W.G., 1946, Observations on Soil Algae: Part II. New Phytologist, v. 45, no. 1, p. 56–110.

Mann, D., and Evans, K., 2008, The species concept and cryptic diversity, *in* Proceedings of the 12th International Conference on Harmful Algae, Copenhagen, International Society for the Study of Harmful Algae and Intergovernmental Oceanographic Commission of UNESCO, p. 262–268.

Metzeltin, D., Lange-Bertalot, H., and García-Rodríguez, F., 2005, Diatoms of Uruguay. Compared with other taxa from South America and elsewhere: Koenigstein, Koeltz Scientific Books, Iconographia Diatomologica, v. 15, 736 p.

Milanovic, S., 2007, Hydrogeological characteristics of some deep siphonal springs in Serbia and Montenegro karst: Environmental Geology, v. 51, no. 5, p. 755–759. https://doi.org/10.1007/s00254-006-0391-1

Miscoe, L.H., Johansen, J.R., Kociolek, J.P., Lowe, R.L., Vaccarino, M.A., Pietrasiak, N., and Sherwood, A.R., 2016, The diatom flora and cyanobacteria from caves on Kauai, Hawaii: Acta Botanica Hungarica, v. 58, p. 3–4.

Mulec, J., and Kosi, G., 2009, Lampenflora algae and methods of growth control: Journal of Cave and Karst Studies, v. 71, no. 2, p. 109–115.

Mulec, J., Kosi, G., and Vrhovšek, D., 2007, Algae promote growth of stalagmites and stalactites in karst caves (Škocjanske Jame, Slovenia): Carbonates and Evaporites, v. 22, no. 1, p 6-9.

Niemiller, M.L., and Soares, D., 2015, Cave Environments, *in* Riesch, R., Tobler, M., and Plath, M., eds., Extremophile Fishes: Heidelberg, Springer International Publishing, p. 161–191.

Ortiz, M., Legatzki, A., Neilson, J.W., Fryslie, B., Nelson, W.M., Wing, R.A., Soderlund, C.A., Pryor, B.M., and Maier, R.M., 2014, Making a living while starving in the dark: metagenomic insights into the energy dynamics of a carbonate cave: The ISME Journal, v. 8, no. 2, p. 478–491. doi: 10.1038/ismej.2013.159

Petitpierre, E., and Gómez-Zurita, J., 1998, Los Chrysomelidae de León; NO de España (Coleoptera): Nouvelle Revue d'Entomologie (NS), v. 15, no. 1, p. 13–26.

Piano, E., Bona, F., Falasco, E., La Morgia, V., Badino, G., and Isaia, M., 2015, Environmental drivers of phototrophic biofilms in an Alpine show cave (SW-Italian Alps): Science of The Total Environment, v. 536, p. 1007–1018. DOI:10.1016/j.scitotenv.2015.05.089

QGIS. 2017. Quantum GIS Geographic Information System. Open Source Geospatial Foundation Project. http://qgis.osgeo.org"

Rushforth, S.R., Kaczmarska, I., and Johansen, J.R., 1984, The subaerial diatom flora of Thurston Lava Tube, Hawaii: Bacillaria, v. 7, p. 135–157.

Salgado, J., 1985, Nuevos datos sobre Catopidae (Col.) capturados en cuevas: Boletín de la Asociación española de Entomología, v. 9, p. 271–277.

Sherwood, A.R., Carlile, A.L., Neumann, J.M., Kociolek, J.P., Johansen, J.R., Lowe, R.L., Conklin, K.Y., and Presting, G.G., 2014, The Hawaiian freshwater algae biodiversity survey (2009-2014): systematic and biogeographic trends with an emphasis on the macroalgae: BMC Ecology, v. 14, no. 28. doi: 10.1186/s12898-014-0028-2

St. Clair, L., Rushforth, S., and Allen, J., 1981, Diatoms of Oregon Caves National Monument, Oregon: Great Basin Naturalist, v. 41, no. 3, p. 9.

Trajano, E., Gallão, J.E., and Bichuette, M.E., 2016, Spots of high diversity of troglobites in Brazil: the challenge of measuring subterranean diversity: Biodiversity and Conservation, v. 25, no. 10, p. 1805–1828. doi: 10.1007/s10531-012-0242-1

Urzì, C., De Leo, F., Bruno, L., and Albertano, P., 2010, Microbial diversity in paleolithic caves: a study case on the phototrophic biofilms of the Cave of Bats (Zuheros, Spain): Microbial ecology, v. 60, no. 1, p. 116–129. doi: 10.1007/s00248-010-9710-x.

Van de Vijver, B., and Beyens, L., 1999, Biogeography and ecology of freshwater diatoms in Subantarctica: a review: Journal of Biogeography, v. 26, no. 5, p. 993–1000.

Van de Vijver, B., and Cox, E.J., 2013, New and interesting small-celled naviculoid diatoms (Bacillariophyceae) from a lava tube cave on Île Amsterdam (TAAF, Southern Indian Ocean): Cryptogamie, Algologie, v. 34, no. 1, p. 37–47. https://doi.org/10.7872/crya.v34.iss1.2013.37

Van de Vijver, B., Frenot, Y., and Beyens, L., 2002, Freshwater Diatoms from Ile de la Possession (Crozet - Archipelago, Subantarctica): Berlin, J. Cramer in der Gebrüder. Borntraeger Verlagsbuchhandlung, Bibliotheca Diatomologica, v. 46, p. 412.

Van de Vijver, B., Gremmen, N., and Smith, V., 2008, Diatom communities from the sub-Antarctic Prince Edward Islands: diversity and distribution patterns: Polar Biology, v. 31, no.3, p. 795–808. https://doi.org/10.1007/s00300-008-0418-z

Van der Werff, A., 1955, A New Method of Concentrating and Cleaning Diatoms and Other Organism: Verhandlungen der Internationalen Vereinigung für theoretische und angewandte Limnologie, v. 12, p. 276–277.

Vanormelingen, P., Verleyen, E., and Vyverman, W., 2008, The diversity and distribution of diatoms: from cosmopolitanism to narrow endemism: Biodiversity and Conservation, v. 17, no. 2, p. 393–405. https://doi.org/10.1007/s10531-007-9257-4

Vyverman, W., Verleyen, E., Sabbe, K., Vanhoutte, K., Sterken, M., Hodgson, D.A., Mann, D.G., Juggins, S., Vijver, B.V. de, Jones, V., Flower, R., Roberts, D., Chepurnov, V.A., Kilroy, C., Vanormelingen, P., and De Wever, A., 2007, Historical processes constrain patterns in global diatom diversity: Ecology, v. 88, no. 8, p. 1924–1931.

Werum, M., and Lange-Bertalot, H. 2004, Diatomeen *in* Quellen unter hydrogeologischen und anthropogenen Einflüssen in Miitteleuropa und Anderen Regionen: Koenigstein, Gantner Publishing, Iconographica Diatomologica, v.13, 417 p.

Whitaker, R.J., Grogan, D.W., and Taylor, J.W., 2003, Geographic Barriers Isolate Endemic Populations of Hyperthermophilic Archaea: Science, v. 301, no. 5635, p. 976–978. DOI:10.1126/science.1086909

Zimmermann, C., Poulin, M., and Pienitz, R., 2010, Diatoms of North America: The Pliocene-Pleistocene freshwater flora of Bylot Island, Nunavut, Canadian High Arctic: Koenigstein, Gantner Publishing, Iconographia Diatomologica, v. 21, 407 p.

Rouhollah Adinehvand and Ezzat Raeisi. Characterization of a karst aquifer in a complex tectonic region, Southwestern Iran. *Journal of Cave and Karst Studies*, v. 80, no. 4, p. 190-205. DOI:10.4311/2017ES0107

# CHARACTERIZATION OF A KARST AQUIFER IN A COMPLEX TECTONIC REGION, SOUTHWESTERN IRAN

Rouhollah Adinehvand[1] and Ezzat Raeisi[2,C]

ABSTRACT

Characterization of karst aquifers is not unique and depends on geological and structural settings, relief, precipitation, and the interactions of these parameters. Therefore, the characterization of a highland karst aquifer in tectonized geological settings is still a challenge, especially in a region with scarce hydrogeological data. In this study, we characterize an inaccessible highland karst aquifer under the severe compressional stresses of two thrust faults, using extensive hydrogeological data by an integrated approach. The Malagha karst aquifer is located in the southern limb of the Malagha Anticline in a tectonized highland zone and is bounded by the Malagha and Qale-Tol thrust faults. Dam construction-related data including hydrochemical data, stable isotopes, water table levels, geological logs, permeabilities, fracture zones from numerous boreholes, and data from three dye tracer tests were used to evaluate the aquifer behavior. The exposed breccia zones and the significant water table differences on both sides of the Qale-Tol thrust fault core confirm the barrier behavior of the fault. The damage zone is highly fractured based on the geological logs, resulting in a relatively uniform water level distribution. The karst water flows through the extensive fracture networks inside the damage zone with no evidence of converging toward any main conduit. The type of flow is most probably diffuse, based on two dye tracer tests, the flat water table, and continuous high permeabilities up to a length of 140 m. The general flow direction is parallel to the fault strike, toward the downstream alluvium bounded between two impermeable formations. This conclusion is based on water balance, geological settings, and $\delta^{18}O$ and $\delta^{2}H$ data. Due to the flatness of the water table, such conditions as the mound below the Abolabbas River, bedding plane dips, and fractures and joints may locally control the flow direction. The footprint of the karst water and the recharge from the Abolabbas River are distinguishable by the hydrochemical and isotopic data.

## Introduction

A karst aquifer is a complex heterogeneous medium because its characteristics are controlled by several factors including tectonic and stratigraphic settings, precipitation, temperature, and local and regional base levels. These parameters vary significantly between different karst aquifers, especially in active tectonic zones. Deep knowledge of karst aquifers is very important for drinking, industrial, and agricultural karst water uses and selection of dam sites or tracing contaminants.

Reviewing research on the effects of faults on non-karstic formations is required to understand the actions of the faults on karst aquifers. Faults control the aquifer hydraulic behavior and the groundwater flow pattern (Bense et al., 2008; Mayer and Sharp, 1998; Bense and Person, 2006; Mayer et al., 2007) Fault zones usually consist of a fault core that is surrounded by a damage zone cutting through the un-deformed host-rock, or protolith (Chester and Logan, 1986; Caine et al., 1996; Bense et al., 2013). The protolith may contain background joints, not primarily related to the fault zone (Bense et al., 2013). The fault core is the zone of the most intense strain and refers to intensely deformed materials which strongly reduce porosity and permeability compared to the adjacent damage zone and protolith (Chester and Logan, 1986; Antonellini et al., 1994; Goddard and Evans, 1995). Therefore, fault cores may act as low-flow or no-flow boundaries (Caine et al., 1996). The damage zone has secondary structures such as fractures and minor faults which take up the remainder of the strain within the fault zone (Bense et al., 2013) and causes heterogeneity and anisotropy in the permeability of the fault zone (Bruhn et al., 1994; McGrath and Davison, 1995). The secondary structures enhance permeability relative to the fault core and the host-rock (Chester and Logan, 1986; Goddard and Evans, 1995; Bense et al., 2013; Solum and Huisman, 2016). The damage zones form permeable fractures which are mostly oriented parallel to the fault plane (Caine et al., 1996). The permeability of the damage zone is significantly increased due to high fracture density and connectivity and is generally higher than that of the protolith (Bense et al., 2013).

Structural geologists use various methods, such as outcrop mapping of fault zones (Caine and Forster, 1999; Jourde et al., 2002; Shipton et al., 2005), mineralogy and geochemistry studies (Caine and Minor, 2009; Koukouvelas and Papoulis, 2009) , and porosity and permeametry measurements on cores in the laboratory or in the field (Antonellini et al., 1994; Faoro et al., 2009). Hydrogeological methods of studies of the fault zones include subsurface studies such as permeability by pumping tests (Anderson and Bakker, 2008), determination of hydraulic gradients on both sides of the fault core (Bense and Van Balen, 2004), artificial environmental tracer delineating fluid flow paths (Rugh and Burbey,

[1] Department of Earth Sciences, Shiraz University, Shiraz, Fars Province, Iran; radinehvand66@yahoo.com
[2] Department of Earth Sciences, Shiraz University, Faculty of Science, 7146713565; Shiraz, Fars Province, Iran,;
[C]Corresponding author: e_raeisi@yahoo.com

2008; Leray et al., 2012) and numerical models (Caine and Forster, 1999; Jourde et al., 2002; Surrette and Allen, 2008). Hydrogeologists often characterize karst aquifer hydrodynamics without a specific focus on fault zones (Celico et al., 2006; Doan and Cornet, 2007; Apaydin, 2010), in contrast to structural geologists who are mainly focused on fault zone characteristics (Caine et al., 1996; Billi et al., 2003). In literature, the links between the hydrogeological and structural viewpoints, especially in highland tectonized zones, are limited. Bense et al. (2013) extensively reviewed the hydrogeology of fault zones based on both structural and hydrogeological approaches.

In carbonate rocks, cataclasite, ultracataclasite, fault gouge (Agosta and Kirschner, 2003; Billi et al., 2003; Ferrill and Morris, 2003; Kostakioti et al., 2004; Micarelli et al., 2006; Benedicto et al., 2008; Billi, 2010; Tesei et al., 2013), clay smear and fluid flow cementation (Micarelli et al., 2006; Kim and Sanderson, 2010) reduce permeability of the fault cores. In karstic carbonate aquifers, the impermeable fault cores impede the flow perpendicular to the core and direct the flow parallel to the fault plane in the damage zone, creating a significant head difference, for example 5 m to 7 m (Celico et al., 2006) and 40 to 100 m (Cappa et al., 2005, 2007; Hamaker and Harris, 2007; Micarelli et al., 2006; Doan and Cornet, 2007; Apaydin, 2010 on both sides of the fault cores. Faults in carbonate rocks display a complex hydrogeological behavior, from barriers by secondary cementation or smearing of low permeability material in the core to conduits developed by the dissolution process in fractured dominantly damage zone (Bense et al. 2013). The productive Edwards Aquifer in south-central Texas, USA, formed in Cretaceous limestones is another example of active karst regions (Maclay, 1995; Ferrill et al., 2004). The karst groundwater flow in the aquifer is controlled by the Balcones fault system, a system of high-angle normal faults (Ferrill et al., 2004). Faulting had a critical role in the aquifer evolution (Lindgren et al., 2004), through solution enlargement of fractures and forming caves along faults (Hovorka et al., 1998). The faults strongly control cave orientation (Wermund et al., 1978; Alexander, 1990) and flow direction (Lindgren et al., 2004). Alpine karst in Europe can be divided into two main karst type, the plateau-like karst massifs (deep karst) and the folded alpine karst (shallow karst) based on geological and tectonical structures (Goldscheider and Hoetzl, 1999). As part of the Alpine fold and thrust belt, the strata are affected by polyphase deformation and the tectonics is very complex in high alpine karst plateaus (Plan et al., 2009). Faults are a main factor controlling drainage patterns of thick carbonate sequences in the south of Alpine and Austroalpine zones (Hoetzl, 1998; Goldscheider and Neukum, 2010) . Cave patterns and groundwater flow paths often follow faults and fractures within the karst limestones (Goldscheider, 2005; Goldscheider and Neukum, 2010) and cross-formational flow between karst aquifers separated with marl formations is demonstrated (Gremaud et al., 2009).

The studied karstic Malagha Aquifer is located in the High Zagros Zone in southwestern Iran, a tectonized highland zone, which is characterized by northwest-trending asymmetric anticlines, synclines and high-angle reverse faults. The Malagha Aquifer is formed in the highly fractured karstic Asmari Formation (AF) of the overturned southern limb of the Malagha Anticline (Fig. 1a and Fig. 1b). The objective of this study is to investigate the hydrogeological behavior of the Malagha karst aquifer within a highly tectonized region, using integration of extensive hydrogeological data. The combination of these specific methods finally enables us to propose a conceptual model of the aquifer.

## Hydrogeological Settings

The karstified carbonate rocks crop out on about 23 % of the Zagros Mountains in the south-central regions of Iran (Nassery, 1991; Raeisi and Kowsar, 1997). The Zagros Mountain ranges have been divided into three zones: High Zagros, Simply Folded Belt, and Khuzestan Plane (Stocklin, 1968; Falcon, 1974; Berberian and King, 1981) . In these regions, most of the hydrogeological and hydrochemical studies on karst aquifers are on the Simply Folded Belt (Raeisi and Karami, 1997). The study area is located on the border between the High Zagros Zone and the Simply Folded Belt inside the Izeh Zone, a tectonized complex zone (Sepehr and Cosgrove, 2004; Sherkati and Letouzey, 2004; Sherkati et al., 2005) and its relationship to sedimentary facies and the evolution of sedimentary depocenters since Late Cretaceous times have been studied, on the basis of one regional balanced transect and several updated isopach maps, in the Izeh zone and the Dezful Embayment, central Zagros. This study relies on fieldwork data, existing geological maps, seismic data and well information. A new structural classification for part of the Zagros sedimentary cover is presented to highlight the different mechanical behavior of the formations in the stratigraphic column. It shows the existence of several local decollement levels activated during folding. These decollement levels separate lithotectonic units, which accommodate shortening in different ways. The Lower Paleozoic is the basal decollement level throughout the studied area. Triassic evaporites, Albian shales, Eocene marls and Miocene evaporites can act as intermediate decollement levels, and present variable facies in the Central Zagros. Lateral facies and thickness variations, the sedimentary overburden and the close relationship with inherited fault patterns influenced the wavelength, amplitude and style of folding in the study area. Furthermore, surface structures do not necessarily coincide with deeper objectives where these disharmonic levels are involved in folding. The evolution of sedimentary depocenters from the Late Cretaceous (obduction episode. The High Zagros Zone is bounded to the northeast by the Main Zagros thrust fault, and in the southwest, it is separated from the Zagros Simply Folded Belt by the seismically active High Zagros Fault (Berberian, 1995). To the southwest,

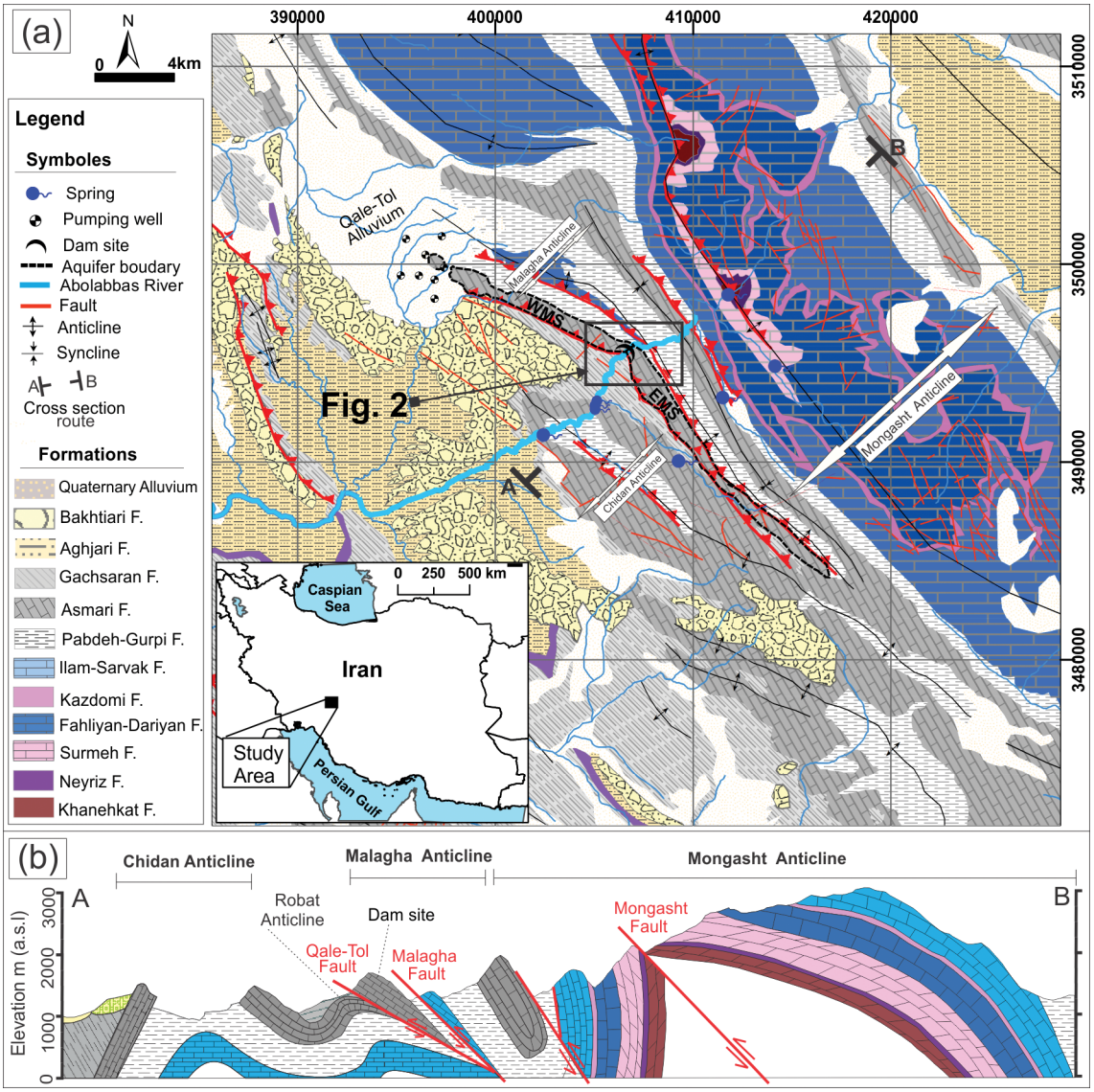


Figure 1. (a) General geological map of the study area. The boundary of the Malagha Aquifer is shown with dashed lines and its western and eastern sub-aquifers (WMS and EMS) in both sides of the Abolabbas River are pointed out in the figure. (b) A geological cross section near the dam site perpendicular to the Malagha Anticline has been drawn, showing the impact of faults on the formation of structures near the dam site and the surrounding geology.

the Zagros Simply Folded Belt is separated from the Khuzestan Plane by the Mountain Front Fault (Falcon, 1961). The Khuzestan Plain is composed of flat alluvial planes. The Simply Folded Belt is distinguished by long, linear, asymmetrical folds having a northwest to southeast trend. The anticlines are well-exposed and separated by broad valleys (Miliaresis, 2001; Ashjari and Raeisi, 2006). The faulting and thrusting in the High Zagros Zone has caused intensive rock deformation, crushing, elevated topography (up to 4000 m above sea level (a.s.l.)), and exposure of the oldest formations (Sherkati and Letouzey, 2004; Emami, 2008). Shortening, closed recumbent folds, and increasing faulting frequency are other characteristics of the High Zagros Zone (Berberian, 1995).

The climate of the study area is semiarid. The minimum, maximum and average annual precipitation are 379 mm, 907 mm, and 622 mm, respectively. Annual average evaporation is 1457 mm and daily temperature ranges from −1 °C to 41 °C (Mahab Ghodss Consulting Engineers, 2004). All precipitation occurs during November to May, mostly in the form of rain or snowfall (Najmeddin et al., 2017). The main exposed formations, in decreasing order of age, are Surmeh limestone (Oxfordian-Tithonian), Fahliyan-Dariyan limestone (Berriasian-Aptian), Sarvak-Ilam limestone (Cenomanian-Campanian), Pabdeh-Gurpi marl with thin interbeds of marly limestone (Paleocene-Oligocene), Asmari limestone (Oligocene-Miocene), Gachsaran marl, anhydrate, gypsum and salts (Lower Miocene), Aghajari marl and sandstone (Upper Miocene), and Bakhtiari conglomerates (Pleistocene) (Fig. 1a). In the study area, there are three anticlines as the main geological structures, namely the Mongasht, Malagha and Chidan (Fig. 1a). Three main reverse faults, Mongasht, Malagha, and Qale-Tol, parallel to the anticlines' axis, have been formed by compressional forces (Fig. 1b). The Mongasht Anticline, with the highest elevation in the study area, is an asymmetric tight fold with a short wavelength. The cores of the Mongasht and Malagha Anticlines are exposed due to faulting and erosion processes, in a way that the northern and southern limbs are disconnected and the older formations outcrop at the surface (Fig. 1a). The southern limbs of these two anticlines are overturned. The syncline between the Mongasht and Malagha Anticlines

is an overturned close fold. The Chidan Anticline is located near the border of the Simply Folded Belt. The Mongasht and Malagha are tight folds with short wavelengths compared to the Chidan Fold. The Robat Anticline is a small subsurface asymmetric anticline located between the Malagha and Chidan Anticlines (Fig. 1b).

Intensive tectonic activity has formed several parallel independent aquifers in the karstic Asmari, Fahliyan-Dariyan, and Sarvak-Ilam Formations at the northern and southern limbs of the Mongasht and Malagha Anticlines (Fig. 1a). The karst waters of these independent aquifers are mainly discharged through several springs (Adinehvand, 2017). The AF of the overturned southern limb of the Malagha Anticline has formed karstic Malagha Aquifer (Fig. 1a). The AR divided the Malagha Aquifer into the western and eastern parts or sub-aquifers. The parts of the Malagha Aquifer on the left and right sides (banks) of the AR and Malagha Gorge are named the Eastern and Western Malagha sub-aquifers, respectively (Fig. 1a). No springs emerge from the Malagha Aquifer. The karst waters of the aquifer discharge into the Qale-Tol alluvial aquifer at the western plunge of the Malagha Anticline, being exploited by several pumping wells (Fig 1a). The boundaries of the Malagha Aquifer are limited to impermeable Pabdeh-Gurpi and Gachsaran Formations from the northern and southern sides, and to the Qale-Tol alluvial aquifer and Chidan Anticline at the western and eastern plunges, respectively (Fig. 1a). There are no sinkholes, shafts, big caves, nor springs in the Malagha Aquifer. The karst features are grikes, rillenkarren, and rain pits. The sources of karst waters are autogenic recharge from precipitation through thin soil covers, fractures, grikes, and seepage from the AR bed. Parts of the Malagha Aquifer and Robat Anticline, upstream and downstream of the Qale-Tol thrust fault bounded by boreholes, are named the Dam-site Malagha Aquifer (DMA) and the Local Robat Aquifer (LRA), respectively (Fig. 2). The DMA is located in parts of the As1, As2 and As3 Units of the overturned southern limb of the Malagha Anticline (Fig. 2). The LRA is a small aquifer with an exposed area of about 0.05 km$^2$, formed in the As3 Unit of the northern limb of the Robat Anticline (Fig. 2). Both of these aquifers are unconfined.

The Abolabbas Dam under study, with a reservoir capacity of 113.4 Mm$^3$ and height of 138 m, is located inside the Malagha Gorge on the AF (Fig. 3). The dam will be constructed across the AR. The sources of the AR are three large karst springs, flood waters, and snowmelt from the Mongasht Anticline and the northern limb of the Malagha Anticline (Fig. 1a). The minimum, maximum and average discharges of the AR at the dam site are about 1 m$^3$/s, 8.8 m$^3$/s, and 2 m$^3$/s, respectively. Parts of Malagha Aquifer have been studied in detail already in order to design the Abolabbas Dam. The Mahab Ghodds Consulting Engineers (2004) classified the AF of the Malagha Aquifer into three units, namely the lower (As1),

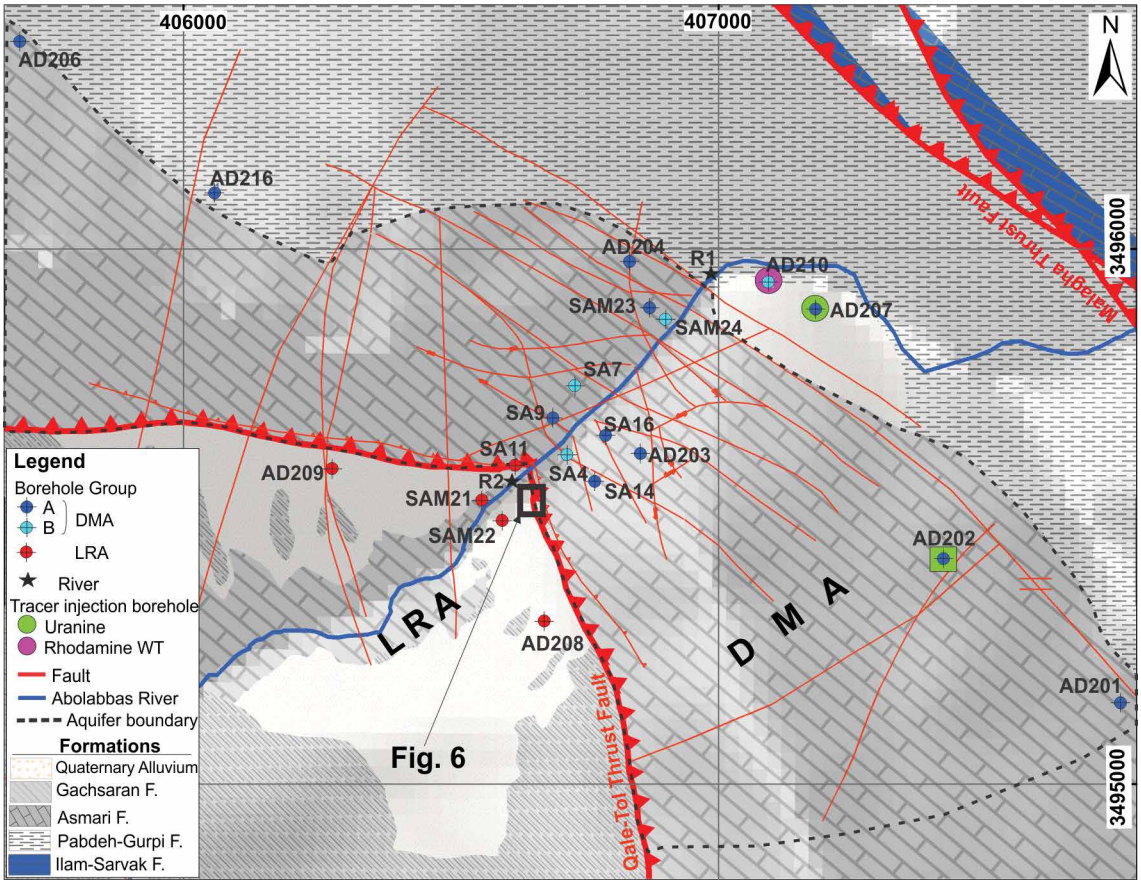


Figure 2. Geological map of the dam site and the location of the DMA and LRA boreholes. All the boreholes were used for water table monitoring and water sampling in the hydrogeochemical analyses and tracer tests. Dye injection boreholes are pointed out in the figure (green circle for the first test (uranine); the cyan circle for the second test (rhodamine WT); and the green square for the third test (uranine)). See also Figure 1a in for the location of Figure 2.

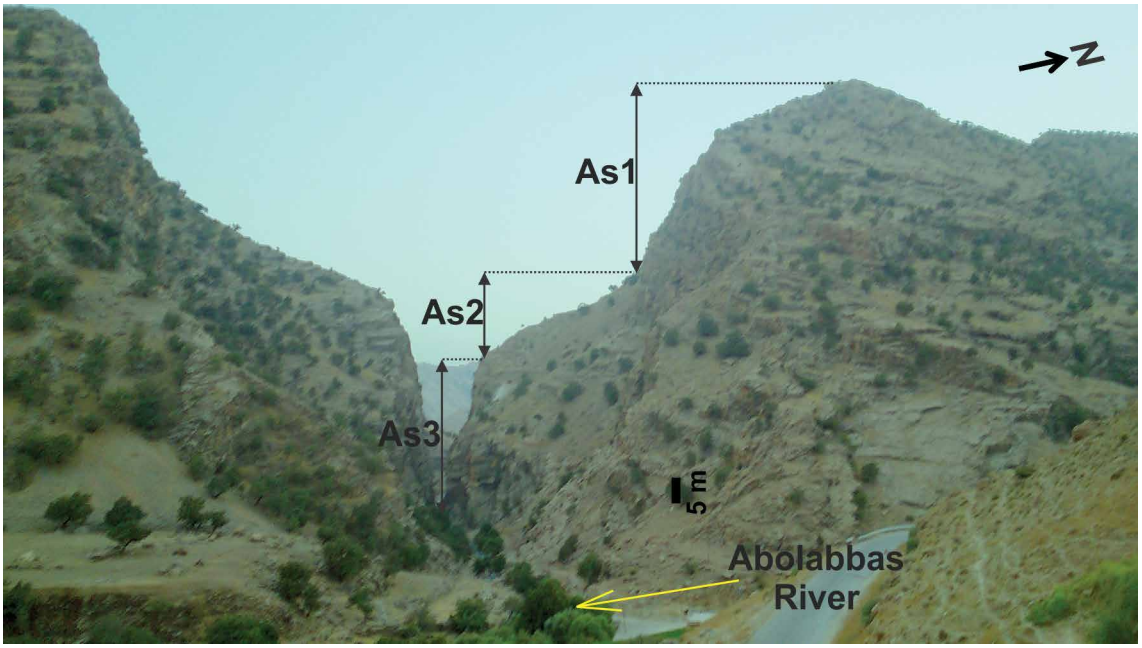


Figure 3. A photograph from the As1, As2 and As3 Units at the Malagha Gorge, where the Abolabbas Dam is planned to be constructed. The As2 Unit containing more marly limestone and limy marlstone formed a smooth topography between As1 and As3 Units.

middle (As2) and upper (As3) Asmari, in decreasing order of age, based on morphological, lithological, and hydrogeological characteristics (Fig. 3). The As1 and As3 Units make cliffs, while As2 unit makes a gentle topography (Fig. 3). The As1 Unit, with a thickness of 110 m, is composed of thick to massive limestones. The main characteristics of this unit are intensive fracturing and jointing. The As2 Unit is divided into the As2-a, As2-b and As2-c Subunits. The As2-a Subunit, with a thickness of 33 m, is composed of thin to medium bedded limestones with marly limestone interbeds. The As2-b Subunit consists of 21 m of marly limestone to marlstone. The As2-c Subunit has a thickness of 26 m of sandy limestones, thin to medium-bedded crystalline limestone with marl interbeds. The As3 Unit, with 150 m thickness, is composed of thin to thick-bedded and massive microcrystalline limestones with intensive fracturing. The dam is planned to be constructed on this unit.

## Materials And Methods

The hydrogeology of the area was studied by Shiraz University from 2010 to 2015 (Majd, 2011; Adinehvand, 2017). The boundaries of the Malagha Aquifer (Fig. 1a) was estimated using geological settings, water balances, and $\delta^{18}O$ and $\delta^{2}H$ compositions (Adinehvand, 2017). The average aquifer recharge was estimated using the following equation

$$V = \frac{A \times P \times I}{t} \quad (1)$$

where $V$ is the volume of recharge by precipitation ($m^3$/year), $A$ is the aquifer surface area ($10^{-6}$ $km^2$), $P$ is the mean annual precipitation depth ($10^3$ mm), $I$ is the recharge coefficient and $t$ is one hydrological year. The precipitation depth (mm) at a specific elevation (m a.s.l.) was calculated using the precipitation-elevation relationship from 10 neighboring meteorological stations as follows,

$$P = 293.08 \ln H - 1356.7 \quad (2)$$

The mean annual precipitation ( ($10^3$ mm)) over a specific area is calculated as follows,

$$\bar{P} = 10^{-3} \sum_{i=1}^{n} 293.08 \ln H_i - 1356.7 \quad (3)$$

where $n$ is the number of 30 m by 30 m cells of the Digital Elevation Model (DEM) and $H$ is the topographic elevation of each cell. The depth to the water level is at least 40 m below ground surface and therefore, evaporation from groundwater in neglected in the above calculations.

The flow rate of the AR was measured four times by a current-meter at the beginning and the end of the Malagha Gorge to determine the seepage from the river bed inside the Malagha Aquifer. Twenty boreholes were constructed on the eastern and western sides of the AR (Fig. 2; Table 1) by the Khuzestan Regional Water and Power Authority within the DMA and LRA and hydrogeological data were collected (Majd, 2011; Adinehvand, 2017). The lithology, permeability (lugeon) and fractures were measured at 5 m steps in these borehole logs.

**Table 1. Hydrogeochemical data of the water samples.**

| Name | HCO3 (epm) | Ca (epm) | Mg (epm) | SO4 (epm) | Cl (epm) | Na (epm) | K (epm) | CO3 (epm) | TDS (mg/L) | EC (uS/cm) | Water-Type |
|---|---|---|---|---|---|---|---|---|---|---|---|
| Abolabbas River | 3.40 | 3.06 | 1.69 | 0.97 | 0.38 | 0.05 | 0.02 | 0.05 | 226 | 290 | Ca-$HCO_3$ |
| Dam-site Malagha Aquifer | | | | | | | | | | | |
| Group A | | | | | | | | | | | |
| AD201 | 3.32 | 2.12 | 1.91 | 0.34 | 0.53 | 0.10 | 0.02 | 0.04 | 180 | 262 | Ca-$HCO_3$ |
| AD202 | 3.02 | 2.14 | 1.76 | 0.67 | 0.58 | 0.10 | 0.03 | 0.01 | 191 | 274 | Ca-$HCO_3$ |
| AD203 | 4.84 | 3.42 | 2.42 | 0.60 | 0.66 | 0.09 | 0.03 | 0.00 | 307 | 442 | Ca-$HCO_3$ |
| AD204 | 3.05 | 2.40 | 1.65 | 0.63 | 0.75 | 0.14 | 0.07 | 0.00 | 200 | 263 | Ca-$HCO_3$ |
| AD216 | 2.30 | 1.50 | 1.70 | 0.45 | 0.80 | 0.11 | 0.08 | 0.00 | 152 | 234 | Mg-$HCO_3$ |
| AD206 | 3.07 | 2.49 | 1.87 | 0.64 | 0.43 | 0.11 | 0.03 | 0.01 | 209 | 308 | Ca-$HCO_3$ |
| AD207 | 3.93 | 3.03 | 2.03 | 0.67 | 0.51 | 0.10 | 0.03 | 0.01 | 242 | 333 | Ca-$HCO_3$ |
| SA14 | 3.23 | 2.68 | 1.45 | 0.59 | 0.70 | 0.06 | 0.03 | 0.01 | 192 | 273 | Ca-$HCO_3$ |
| SA16 | 2.79 | 2.46 | 1.29 | 0.63 | 0.55 | 0.09 | 0.03 | 0.11 | 197 | 272 | Ca-$HCO_3$ |
| SA9 | 2.90 | 2.35 | 1.58 | 0.62 | 0.70 | 0.07 | 0.03 | 0.00 | 205 | 288 | Ca-$HCO_3$ |
| SAM23 | 3.10 | 2.70 | 1.80 | 0.48 | 0.65 | 0.07 | 0.04 | 0.00 | 225 | 315 | Ca-$HCO_3$ |
| Group B | | | | | | | | | | | |
| AD210 | 3.80 | 3.28 | 1.58 | 1.14 | 0.53 | 0.15 | 0.03 | 0.07 | 236 | 340 | Ca-$HCO_3$ |
| SA7 | 2.99 | 2.53 | 1.76 | 0.96 | 0.66 | 0.08 | 0.03 | 0.00 | 197 | 285 | Ca-$HCO_3$ |
| SA4 | 3.77 | 3.00 | 1.77 | 1.04 | 0.67 | 0.09 | 0.07 | 0.00 | 227 | 329 | Ca-$HCO_3$ |
| SAM24 | 3.74 | 3.20 | 1.87 | 0.99 | 0.58 | 0.06 | 0.02 | 0.00 | 235 | 331 | Ca-$HCO_3$ |
| Local Robat Aquifer | | | | | | | | | | | |
| AD209 | 3.30 | 2.70 | 1.50 | 0.67 | 0.50 | 0.09 | 0.04 | 0.00 | 216 | 332 | Ca-$HCO_3$ |
| AD208 | 3.44 | 6.03 | 2.50 | 4.58 | 0.64 | 0.13 | 0.03 | 0.02 | 515 | 625 | Ca-$SO_4$ |
| SA11 | 2.93 | 2.62 | 1.58 | 1.11 | 0.52 | 0.07 | 0.03 | 0.03 | 237 | 321 | Ca-$HCO_3$ |
| SAM21 | 1.60 | 1.22 | 0.82 | 0.08 | 0.58 | 0.35 | 0.08 | 0.12 | 119 | 141 | Ca-$HCO_3$ |
| SAM22 | 2.07 | 1.60 | 1.10 | 0.14 | 0.60 | 0.10 | 0.03 | 0.00 | 138 | 174 | Ca-$HCO_3$ |

The water table levels were measured 19 times during the study period (2010 – 2015) in most of the DMA and LRA Boreholes (Fig. 2). The waters of the boreholes (DMA and LRA) and AR at the Malagha Gorge (Fig. 3) were sampled during the study period using USEPA (2007) and USGS (2006) guidelines. The pH, EC, and temperature were measured in the field, using portable instruments (WTW). The major anions and cations concentration and TDS were measured at the laboratory of the Department of Earth Sciences, Shiraz University. Major anion and cations concentration were analyzed based on methods of the American Public Health Association (APHA, 2005): sodium and potassium by flame photometer; calcium, carbonate, bicarbonate, and chloride by titration, while magnesium was calculated from the calcium contents, and the sulfates were estimated using the turbidity method. Stable isotope $^{18}O$ and $^{2}H$ compositions of six boreholes (AD201, AD202, AD207, AD208, SA7, and AD206) and the AR at the beginning and end of the Malagha Gorge (R1 and R2) were measured in the dry and wet seasons at the Freiberg Laboratory, Technische Universität Bergakademie, using the double mass spectrometry method (Fig. 2).

Three dye tracer tests, using fluorescent dyes, were performed in order to study the groundwater flow path and velocity within the Malagha Aquifer. In the first tracer test, 15 kg of uranine (MERK) were injected into Borehole AD207 (Majd, 2011) (Fig. 2). This borehole intersects the As1 Unit below the water table. In the second tracer test, 86 liters of Rhodamine WT (TURNER) was injected into Borehole AD210 in June 2014 (Fig. 2). This borehole intersects the As1 Unit below the water table. Forty kg of uranine (MERK) were injected into Borehole AD202 in the third tracer test (June 2014). This borehole intersects the As3 Unit below the water table. The sampling points of these three tracer tests were all boreholes inside the Malagha Aquifer (Fig. 2) and the pumping wells of the Qale-Tol plane (Fig. 1a). In addition, all the springs of the Chidan Anticline, as well as nine sections along the AR passing through the Malagha Gorge and Chidan Anticline, were also sampled (Fig. 1a). The time intervals of the samplings were once every hour and six hours from the sampling points near to and far from the injection wells, respectively, on the first day, which were gradually extended. The dye concentration was measured by a Shimadzu Spectrofluorophotometer, RF-5301PC, at the laboratory of the Department of Earth Sciences of Shiraz University.

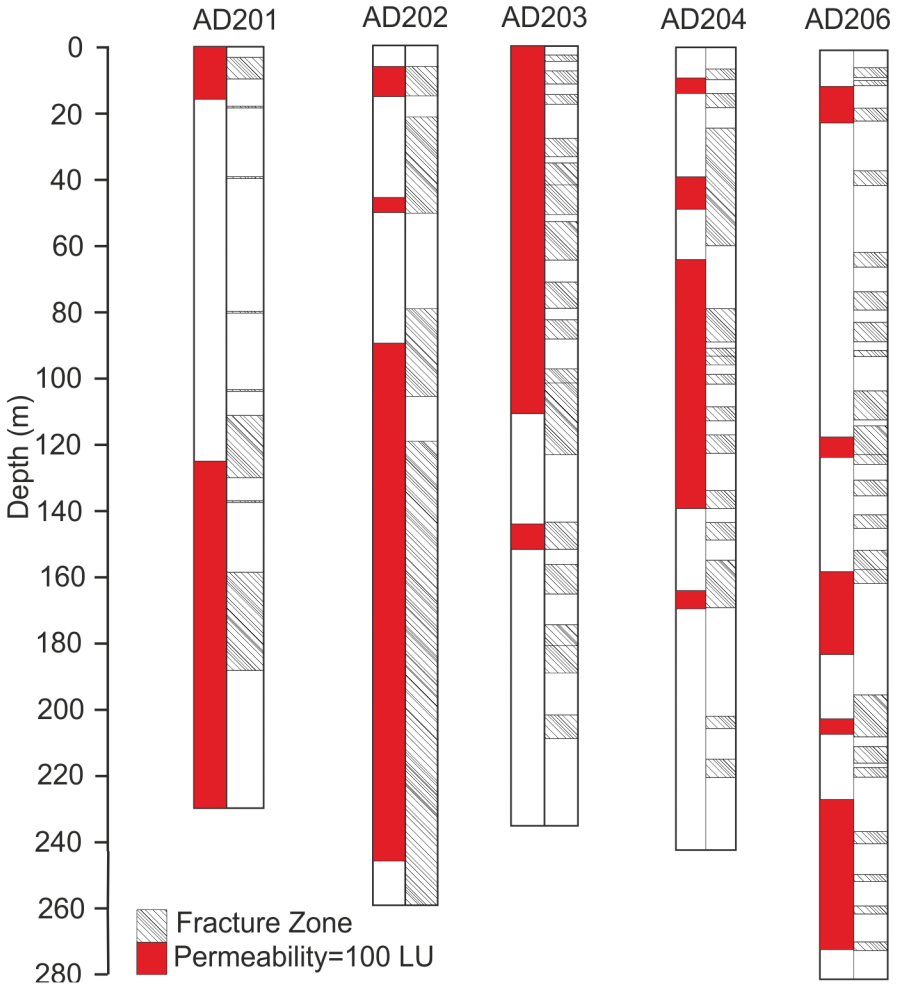


Figure 4. Permeability (lugeon) and fracture zones in the DMA boreholes.

## Results

### Aquifer recharge

Autogenic recharge from precipitation and seepage from the AR bed are the sources for karstic waters of the Malagha Aquifer. The areas of the Eastern and Western Malagha sub-aquifers are 11.2 $km^2$ and 8.0 $km^2$, respectively (Fig. 1a). The recharge coefficient *I* is estimated to be 50 ± 10 % based on the studies of the water balance in similar AF aquifers in the south west of Iran (Pezeshkpour, 1991; Rahnemaie, 1994) and other Mediterranean karst regions (Hartmann et al., 2014). Using Equation (1), the average annual recharge from precipitation on the Eastern and Western Malagha sub-aquifers, and the Malagha Aquifer are estimated to be 4.7 $Mm^3$, 2.9 $Mm^3$, and 7.6 $Mm^3$, respectively. The AR seeps into the karstic Malagha Aquifer along the Malagha Gorge. Four measurements of the AR flow rate at the beginning and end of the Malagha Gorge indicate an average seepage of about 83 $Ls^{-1}$ (2.6 $Mm^3y^{-1}$) (Adinehvand, 2017). Therefore, the total recharge into the Malagha Aquifer is about 10.2 $Mm^3y^{-1}$.

### The hydrogeology of the thrust faults

The hydrogeology of the DMA and LRA is controlled by the actions of Malagha, and especially the Qale-Tol thrust fault (Fig. 1b). The DMA is located in the damage zone of the Qale-Tol and Malagha thrust faults and LRA is located in the damage zone of the Qale-Tol thrust fault. The activity of these two thrust faults has resulted in extensive joints, fracture zones, and minor faults (Fig. 2). The extensive fracture zones are observed in some of the boreholes (Fig. 4) and limestone exposed areas (Fig. 5). The fracture zones in the boreholes have a significant correlation with continuous high permeabilities of 120 m length (Fig. 4). No cavity indicating a conduit was found in the high permeability sections of the boreholes (Adinehvand, 2017). The extensive fracture zones provide more pathways for groundwater flow than intact rock with less fractures which prevents the formation of a main flow pathway. Nonhomogeneous stress intensity causes a heterogeneity in the fracture zone distributions (Fig. 4) resulting in flow within the aquifer focus in the high permeability sections with extensively fractured zones. The Qale-Tol thrust fault core consists of breccia, gauge, cataclasite, and alterations in the exposed area (Fig. 6). The core of the Qale-Tol thrust fault acts as a barrier, disconnecting the hydraulic connection between the two sides of the fault core. The groundwater level differences in the LRA boreholes (AD209, SA11, SAM21, and SAM22) and in all boreholes of the DMA on both sides of the Qale-Tol thrust fault core are 10 m to 30 m (see the next section) which confirm the impermeable behavior of the fault core.

### The Dam-site Malagha Aquifer (DMA) and Local Robat Aquifer (LRA)

Hydrogeochemistry

The chemical composition data in Table 1 gives an overview of the hydrogeochemical characteristics of groundwater in the DMA and LRA. The groundwater samples from DMA, LRA, and Abolabbas River are CaMg-$HCO_3$ type with TDS below 307 mg/L, EC of 442 $\mu Scm^{-1}$, pH of 7.3, and temperature of 19.0 °C. The exception is AD208 in which the water type is Ca-$SO_4$ and TDS is 515 mg/L due to gypsum bearing veins in the borehole log. Groundwater temperature is almost constant in all water samples of the AR, DMA, and LRA.Groundwater samples from LRA show a significant

Figure 5. A photograph showing fracture zones on the limestones in the left side of the Malagha Gorge.

difference in hydrogeochemistry (Table 1). Even though the water type is mostly Ca-$HCO_3$, the EC varies from 141 to 625 µScm$^{-1}$. The lowest ion concentrations were found in SAM21 and SAM22 boreholes (Table 1). For all of the measurements during the monitoring period, the EC in both SAM21 and SAM22 boreholes was about 150 µScm$^{-1}$, which is at least 100 µScm$^{-1}$ less than those of all the other boreholes and the AR (Table 1). The $SO_4$/Cl ratio of the water samples of the two boreholes is less than 1 and the major ions' concentrations are less than those of the AR and all of the other boreholes. The distances of the boreholes SA11, AD208, and AD209 from the AR are about 30 m, 150 m, and 230 m, respectively, and the $SO_4$/Cl ratio is higher than 1 similar to the AR. Based on the $SO_4$/Cl ratio in the water samples of the DMA boreholes, A and B groups can be distinguished (Fig. 7a, 7b). The $SO_4$/Cl ratio in the water samples of Group B boreholes is equal to or less than 1 (Fig. 7a) while in Group B boreholes it is higher than 1 (Fig. 7b). Group B boreholes have the closest distances from the AR and similar to the AR, the $SO_4$/Cl ratio is higher than 1 (Fig. 7b).

Stable isotopes

Stable isotope compositions for $\delta^{18}O$ and $\delta^{2}H$ in water samples of the AR (R1 and R2), DMA (AD201, AD202, AD203, AD206, AD207, and SA7) and LRA (AD208) in dry and wet seasons are shown in Fig. 8. All the water samples in the $\delta^{18}O$ and $\delta^{2}H$ diagram can be placed into two distinct groups of A and B. Group B consists of the boreholes of the DMA which are close to the river, LRA, and river water. The $\delta^{18}O$ values of Group B change from -6.2‰ to -6.2‰ and $\delta^{2}H$ values change from −26.4 ‰ to −23.4 ‰ (Fig. 8). Group A includes water samples of the DMA boreholes which are further from the river (Fig. 2). The $\delta^{18}O$ values of Group B evolve from −5.7 ‰ to −4.3 ‰ and $\delta^{2}H$ values from −20.8 ‰ to −12.3 ‰ (Fig. 8). Most of the water samples fall above global meteoric water line (GMWL) and close to the local meteoric water line (LMWL) (Fig. 8). The river water originates from Mongasht Anticline in the north which has the highest elevations in the study area and its water samples tend to have the most depleted $\delta^{18}O$ and $\delta^{2}H$ compositions (Fig.

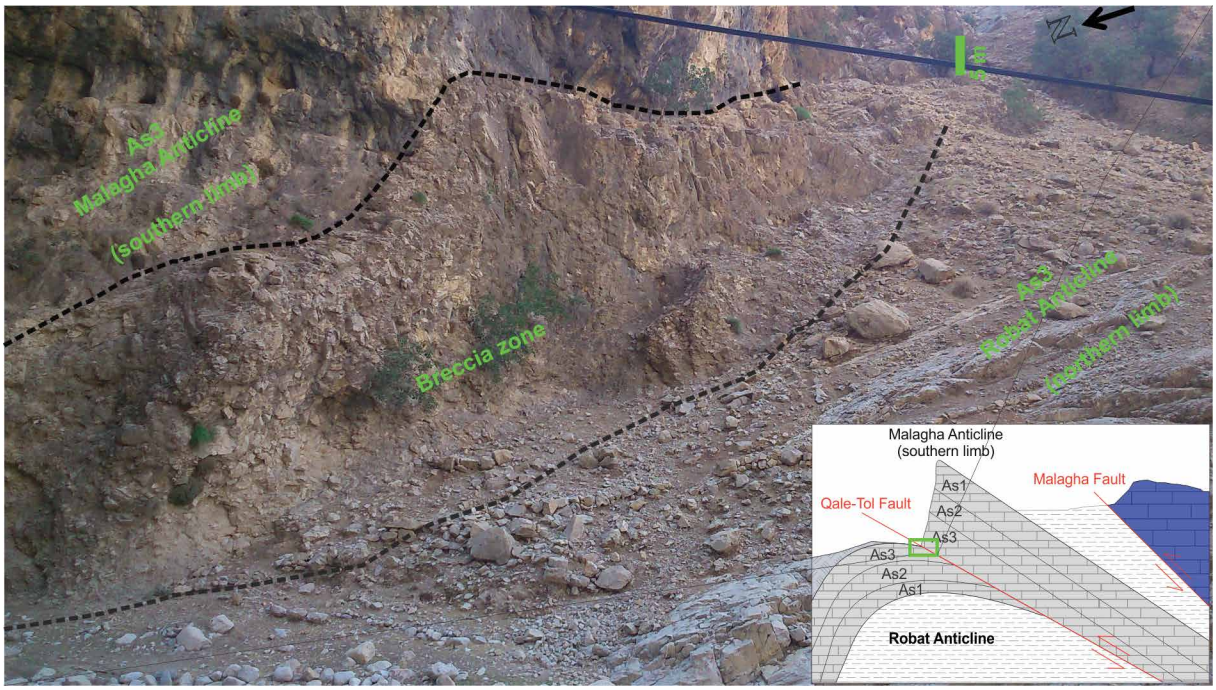


Figure 6. A photograph from breccia zone of the Qale-Tol Fault at the end of the Malagha Gorge. See Figure 2 for the location of Figure 6.

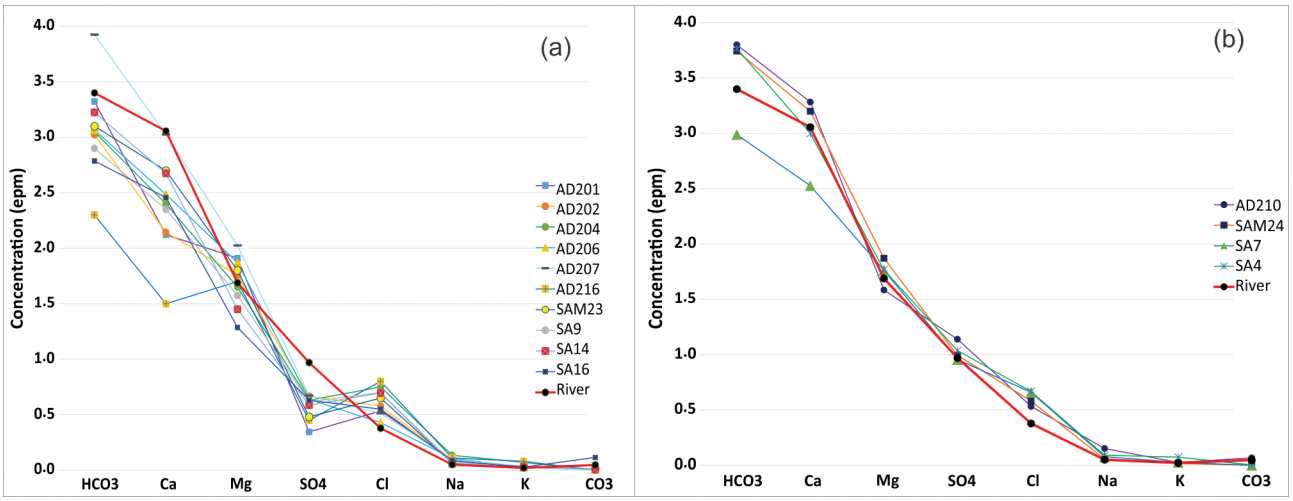


Figure 7. Water table map of the DMA and LRA boreholes. Major ion concentrations of the DMA boreholes; a) Group A, b) Group B.

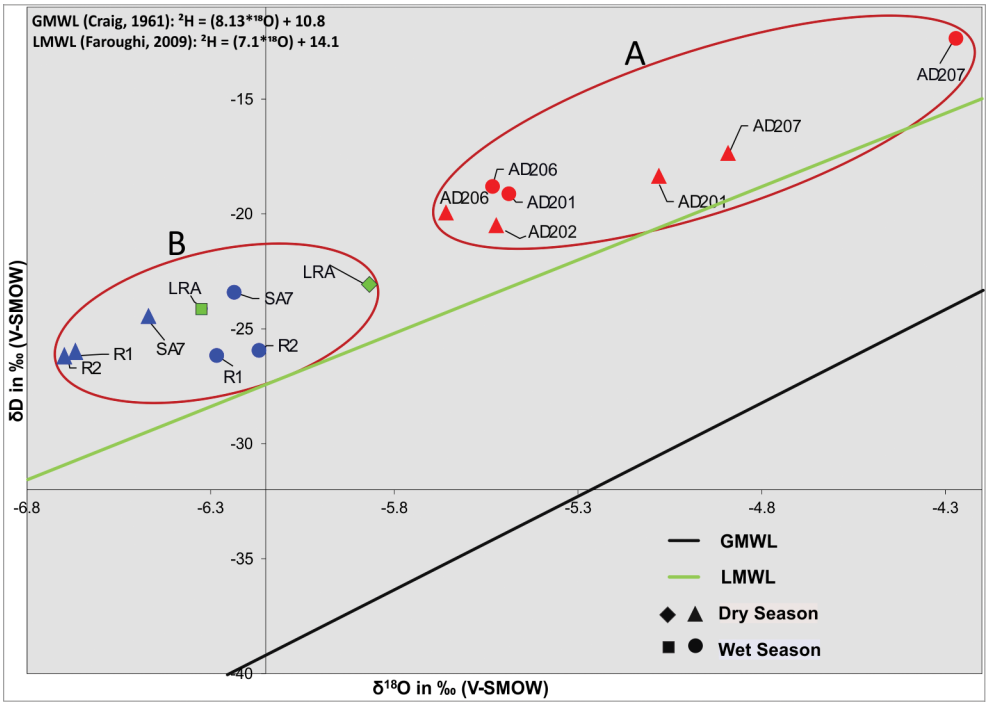


Figure 8. Stable isotope diagram of the DMA and LRA borehole water samples in dry and wet seasons. River water was also sampled at the entrance (R1) and exit (R2) of the Malagha Gorge. GMWL: global meteoric water line (Craig, 1961); LMWL: local meteoric water line (Faroughi, 2009).

8). Among the LRA boreholes, the $\delta^{18}O$ and $\delta^{2}H$ compositions were measured only for AD208. The $\delta^{18}O$ and $\delta^{2}H$ values are depleted and are in the range of the AR in the wet season and show a mixing component (Fig. 8). The water samples of the DMA boreholes which are close to the river show a mixing component and fall in the same group as the river (Group B) (Fig. 8). The waters of Group A tend to have more enriched compositions in $\delta^{18}O$ and $\delta^{2}H$ than those of Group B.

## Water level distribution and fluctuation

Water level data were collected from all DMA and LRA boreholes with different time resolution measurements between June 2010 and August 2015 (Fig. 9). The DMA boreholes for water level monitoring include Group B boreholes (AD210, SA7, SA4, and SAM24), which are located close to the river, have slightly higher water levels, and may be affected by the river seepage, and Group A boreholes (AD201, AD202, AD203, AD204, AD216, AD206, AD207, SA14, SA16, SA9, and SAM23), which are farther from the river (Fig. 2). The LRA boreholes (SAM21, SAM22, SA11, AD208, and AD209) are located downstream of the Qale-Tol fault core, inside the gentle-dip bedding planes of the northern limb of the Robat Anticline (Fig. 1b, Fig. 2). The variations of the water level in each aquifer (DMA and LRA) differ. The water level in the LRA boreholes is 10 to 30 m higher than that of DMA (Fig. 9). The bottom elevations of all LRA boreholes are below the minimum DMA water table level. Therefore, the LRA boreholes are not located in a perched water table aquifer. The minimum, maximum, and average water level differences of the LRA boreholes are 13.4 m, 21.2 m, and 18.2 m, respectively, at a specific time during the monitoring period (Fig. 9). The boreholes SAM21 and SAM22 are located on both sides of the AR, with distances of less than 30 m (Fig. 2). The average of the water table levels of these boreholes is 989.50 m a.s.l., which is the highest among the LRA boreholes (Fig. 9). Groundwater level distributions in the LRA boreholes are highly variable, which is common in a karst aquifer.

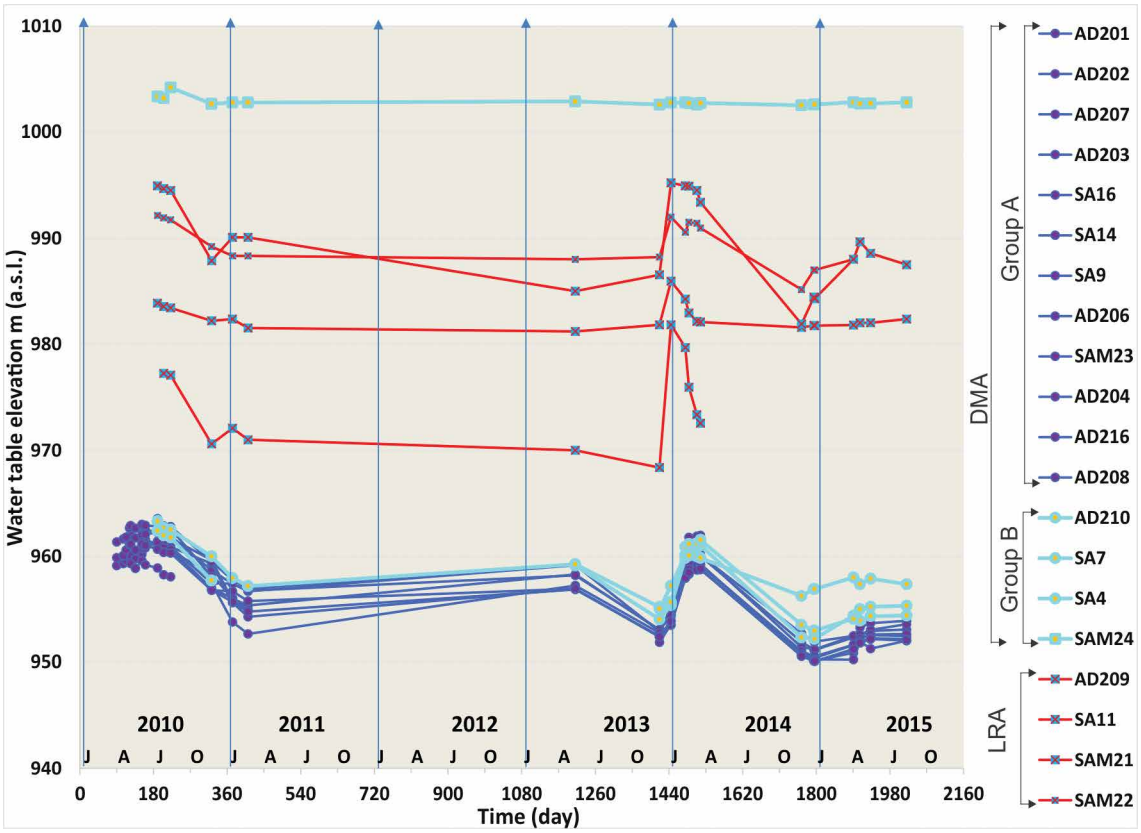


Figure 9. Water level elevation hydrographs in the DMA (Groups A and B) and LRA boreholes.

The water levels of the DMA boreholes are about 60 m below the river bed elevation. The minimum, maximum, and average water level differences of the DMA are 1.2 m, 4.7 m, and 2.8 m, respectively, at a specific time during the monitoring period (Fig. 9). The distances of Group B boreholes from the AR are less than 30 m, while the distances of Group A boreholes from the AR are more than 30 m (Fig. 2). The water table levels in Group B are always slightly higher than those of Group A during the monitoring period (Fig. 9), except for Borehole SAM24 in which the water table level is 45 m higher than that of Group A since it has the closest distance to the AR and has the lowest permeability. Although all of the boreholes of Groups A and B intersect with As1 and/or As3 below the water level, the water-level topography in the DMA is almost flat and shows an almost uniform distribution (Fig. 10a and 10b) similar to granular aquifers. Even though groundwater level measurements are relatively infrequent in time and also have different time resolutions, they can give some valuable information on aquifer homogeneity in space. To show the aquifer heterogeneous behavior more, simultaneous groundwater levels are drawn in the form of a cross-section connecting piezometers AD201 to AD206 as shown in Fig. 10a. The topography of water level is almost flat. To have a better understanding of flow direction in space, a groundwater elevation map for a specific time (July 30, 2014) is also drawn (Fig. 10b). The water level differences are less than 2.5 m and there is no preferential flow direction which shows the effect of the local heterogeneity in permeabilities within the aquifers (Fig. 4). The local flow has different and occasionally opposite directions (Fig. 10b).

### Tracer tests

An overview of the locations and results of the three tracer tests is given in Table 2. In the first tracer test, uranine dye was injected into the Borehole AD207, intersecting the As1 Unit below the water table (Fig. 3), but it was not detected in any of the sampling points (Majd, 2011) (Table 2). The new Borehole AD210, intersecting the As1 Unit, was constructed for the second tracer test (Fig. 2). In the second tracer test, rhodamine WT dye was injected into Borehole AD210 and it was detected only in Borehole AD207 with a maximum velocity of 0.40 m/h, indicating a laminar flow regime (Table 2). In the third test, uranine dye was injected into the Borehole AD202 (Fig. 2), intersecting As1 and As2 from above, and As3 from below the water table level. The dye was only detected in Borehole AD207 at a distance of 550 m from the injection point (Fig. 2). The first and peak dye appearances occurred 76 days and 215 days after the dye injection, respectively. The maximum velocity was 0.62 m/h (Table 2), indicating a laminar flow regime.

## DISCUSSION

### The Dam-site Malagha Aquifer (DMA) and Local Robat Aquifer (LRA)

The hydrogeological study of the DMA and LRA is a suitable method to recognize the behavior of aquifers in a complex tectonic region. Part of the AR water seeps vertically into the DMA and forms a mound below the river and it

**Table 2. Summary of qualitative and quantitative analysis tracer-tests.**

| Tracer Test | Dye Type | Injection Borehole | Detection Point | Migration Distance (m) | Maximum Velocity (m/h) | Peak Velocity (m/h) |
|---|---|---|---|---|---|---|
| First | Uranine | AD207 | N/A | ... | ... | ... |
| Second | Rhodamine WT | AD210 | AD207 | 85 | 0.40 | 0.31 |
| Third | Uranine | AD202 | AD207 | 520 | 0.62 | 0.14 |

Sampling Stations: AD201, AD202, AD203, AD204, AD216, AD206, AD207, SA14, SA16, SA9, SAM23, AD210, SA7, SA4, SAM24, AD209, AD208, SA11, SAM21, SAM22, Abolabbas River (see Fig.2), Qale-Tol wells and Chidan springs (see Fig.1a).

is expected that the boreholes near the AR are under the influence of the mound. The sources of water of the DMA are seepage from the AR and precipitation recharge. The mixing of the AR with Eastern Malagha sub-aquifer water is a very complex process in a heterogeneous karst system. The boreholes of the DMA are classified into the two groups of A and B based on the share of the AR seepage (Fig. 3). Group A consists of boreholes AD201, AD202, AD203 AD207, SA14, SA16, SA9, SAM23, AD204, AD216, and AD206 while the boreholes of Group B are AD210, SA4, SAM24, and SA7 (Fig. 3). The water source of the boreholes of Group A is mainly recharge from precipitation, but the boreholes of Group B are dominantly under the direct influence of river seepage due to the following reasons:

1. The boreholes of Group B have shorter distances to the AR than the boreholes of Group A (Fig. 2).
2. The water table levels in Group B are always slightly higher than those of Group A (Fig. 9).
3. Similar to the AR, the ratio of $SO_4$/Cl in all water samples of Group B is more than 1, whereas, in Group A, it is less than or near 1 (Fig. 7).
4. The $\delta^{18}O$ and $\delta^{2}H$ compositions of the AR with a higher elevation than the Malagha Aquifer and Group B boreholes have the same range on the $\delta^{18}O$ and $\delta^{2}H$ diagram (Fig. 8), while they are enriched in Group A.

Group B boreholes are mainly located in the AR mound area. The mound is formed because the vertical flow of the AR seepage requires an extra head. Because of this, the water table levels of Group B boreholes cannot be used to determine the general flow direction of the DMA. The water table levels of Group A boreholes in the DMA are undulated without any trend to determine the flow direction. The extensive fracture zones caused a large cross-sectional area of flow, resulting in a low hydraulic gradient in the DMA. The uniform distribution and almost flat water-level topography in the DMA (Fig. 10a and 10b) indicate that the DMA has a behavior similar to those of the aquifers with more homogenous media (Bonacci, 1995; Bonacci and Roje-Bonacci, 2000; Kresic, 2010).

In all three dye tracer tests, the dye was not detected in the AR because the water levels in all of the sampling points were less than those of the river bed. The dye was not detected in any of the sampling points in the first tracer test (Majd, 2011). The reasons were the lack of any boreholes in the As1 Unit, and the time of injection being during the dry season (August 23, 2010) and a dry year. The closest boreholes (AD203) were located in the As3 Unit with a straight-line distance of more than 500 m from the injection borehole (AD207) which is located in the As1 Unit. This may indicate that there is no flow through the As3 Unit towards the AD203 Borehole and the dye probably flows only in the As1 Unit. The dye probably diluted and was absorbed by the rock matrix due to the long residence time of a laminar flow and fine materials of the crushed zones (Adinehvand, 2017). In the third tracer test, the dye may have flowed in the direction of the bedding planes slope through the As3, As2, and As1 Units and was detected in Borehole AD207 (Fig. 3). The dye was not expected to flow through the As2 Unit because it was composed of 21 m of marly limestone to marlstone, but this unit is permeable and does not act as an impermeable layer due to extensive fracturing. The dye has most probably been diluted and absorbed by fine crushed-materials in the media, similar to the first tracer test. It was expected that the dye in the third tracer test would flow parallel to the bedding plane strike in the As3 Unit and would be detected in borehole SA16, 600 m away from the injection borehole. The lack of dye detection in this borehole implies that there is no conduit flow in this direction.

The significant lower concentration of the major ions and EC in both of SAM21 and SAM22 boreholes than those of all the other boreholes and AR as well as the $SO_4$/Cl ratio which is less than 1 indicate that the source of the water is not the AR. The chemical characteristics of the water samples in SAM21 and SAM22 indicate that the source of water is probably local precipitation near the boreholes without a significant modification by water-rock interaction (Adinehvand, 2017). The unpredicted behavior of these two boreholes in such a complex tectonic setting merits further research. Despite their long distances from the AR, the main water source of the Boreholes SA11, AD208, and AD209 is probably the AR because: a) similar to the AR, the $SO_4$/Cl ratio is greater than 1; b) the exposed area of the LRA is limited; c) the Robat Anticline is covered by the impermeable Gachsaran Formation, and therefore, there is no recharge from precipitation, and; d) there is no flow from the DMA due to the Qale-Tol impermeable fault core and the DMA has a lower water table level.

## Conceptual model and general flow direction

A conceptual model is proposed for the general flow direction and karst development of the DMA.

In a karst aquifer, groundwater in the intergranular pores in the rock matrix, fissures, fractures, and bedding planes flows towards the solutionally-connected conduits. The extensive fracture zones, continuous high permeabilities in the boreholes, flat and irregular water table, and laminar flow regime by two tracer tests imply no major conduit development and the karst water most probably flows in a network of solutionally-connected fractures. As mentioned earlier, extensive fracture zones were observed in the boreholes (Fig. 4) and several boreholes have a continuous permeability, up to 140 m length and 100 lu[1] (Fig. 4). There was no cavity in the high permeability sections of the boreholes (Adinehvand, 2017). The permeability of 100 lu in the boreholes with no cavity which have continuous lengths of 40 m to 140 m, indicating a distributed flow in the fracture zones. The extensive fracture zones with high permeabilities and no cavity reveal that no conduit has been developed to concentrate the karst water. In all the borehole logs no cavity, indicating the presence of conduits, was found, (Adinehvand, 2017). The water levels are irregular, which is expected in a karst aquifer. However, the differences between the DMA water levels are very low (Fig. 10a and Fig. 10b), and without any preferential direction toward channels or conduits. The almost flat, irregular, and uneven water table of the DMA implies a lack of large conduits to drain the karst water. The main reason is most probably the existence of extensive fracture networks in the DMA which make impermeable marly layers (AS2) more permeable, allow a cross-unit flow, and cause a flat water level by creating a large area of groundwater movement through joints and fractures. The extensive fracture and joints have caused the As2 Unit with a 21 m impermeable marly layer to lose its barrier role making this unit probably permeable because a) there were several boreholes intersecting the As2 Unit above the water table but there was no perched water table; b) dye moved from As3 Unit and then passed through As2 Unit in the form of a cross-unit flow and appeared in the As1 Unit (AD207 Borehole) in the third tracer test, and c) none of the boreholes showed a low permeability in the As2 Unit representing an impermeable marly layer. The existence of extensive fracture zones makes the media more permeable and creates more pathways for water movement. It causes the water to flow mainly through numerous fractures, preventing channelization of the water and formation of main karstic conduits. It seems that the flow is similar to those of alluvial aquifers but the water mainly flows through numerous solutional fractures instead of intergranular pores. The flow regime is laminar in spite of the high permeability of the dye injection and detection boreholes below the water table in the second and third tracer tests. The total area of intensive solutional fractures is so large that it reduces the discharge per unit area and velocity, resulting in a low hydraulic gradients and laminar flow regime. The results of the laminar flow regime in the DMA are compatible with the results from the semi-distributed model of Adinehvand et al. (2017).

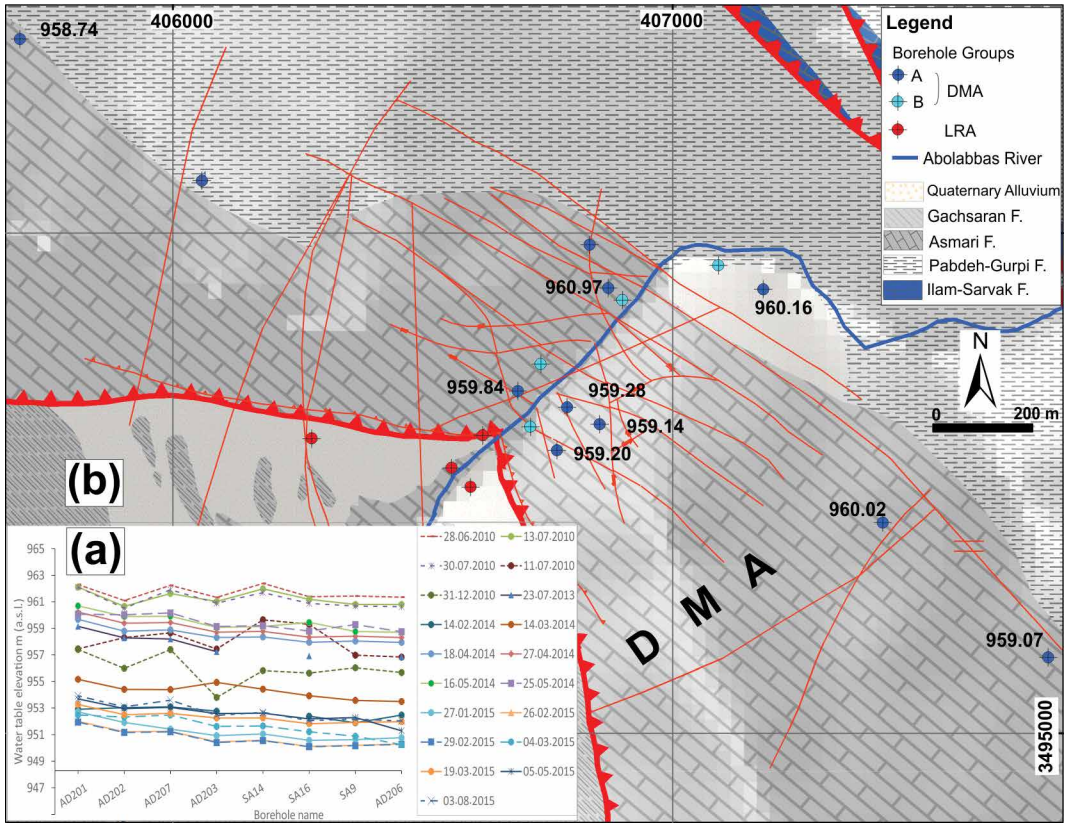


Figure 10. (a) Cross-sections of the simultaneous water levels in the direction of the general flow; (b) Water table elevation map for one of the simultaneous water level measurements shows an almost flat water table and a uniform distribution in the DMA.

The general flow direction is almost parallel to the Malagha Anticline bedding planes strike, toward the Qale-Tol alluvial aquifer (Fig. 11a). The karst water of the Eastern Malagha sub-aquifer is mixed with the AR and

[1] Editor's note: lu = Lugeon; 1 Lugeon Value (lu) = 1 Lmin$^{-1}$ per meter of test interval under a reference pressure of 1 MPa.

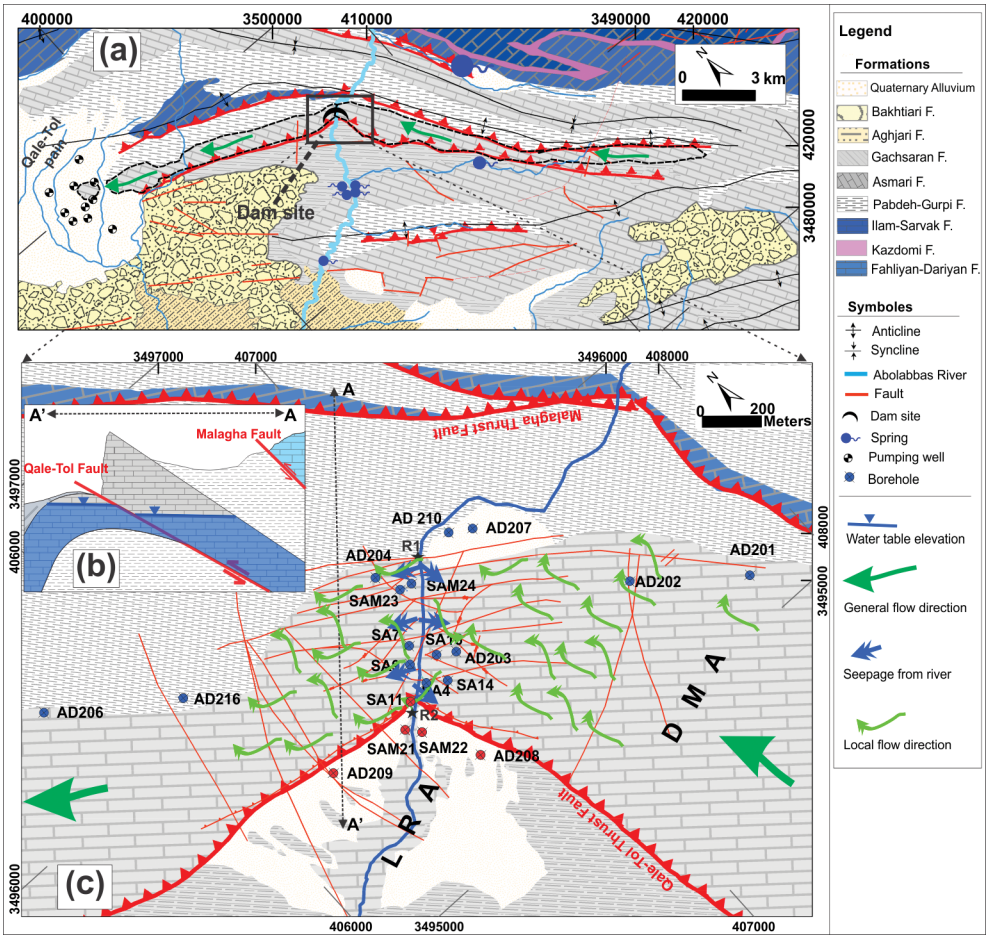


Figure 11. A schematic conceptual model proposing, (a) General flow direction in the Malagha Aquifer, (b) Water level in both sides of the Qale-Tol Fault core, and (c) General and local flow directions in the DMA.

the Western Malagha sub-aquifer, finally discharging into the Qale-Tol alluvial aquifer and is exploited by several wells. The following discussions confirm the proposed general flow direction. The flow direction across the Qale-Tol thrust fault is unlikely for two reasons. First, the core of the Qale-Tol thrust fault is impermeable and acts as a barrier and water levels in the DMA are lower than those in the LRA (Fig. 11b). Second, the water budget of the Chidan Aquifer indicates a balance between the recharge and discharge components (Adinehvand, 2017). The karst water of the Malagha Aquifer cannot be transferred toward the AF of the northern limb of the Malagha Anticline because: a) the connection of the northern and southern limbs is disconnected by the Malagha thrust fault and the impermeable Pabdeh-Gurpi Formations (Fig. 11a and Fig. 11b); b) the contact elevations of the northern limb of the Malagha Anticline with the adjacent Pabdeh-Gurpi Formations are significantly higher than those of the DMA water table. The flow direction is not toward the east because the contact elevations of the Malagha Aquifer with the Pabdeh-Gurpi and Gachsaran Formations are higher than the DMA water table and no springs emerge from the contact. Therefore, the karst water flow path is only toward the west, which is discharged by several exploitation wells in the Qale-Tol alluvial aquifer (Fig. 11a). In addition, the water levels of the DMA are about 110 m higher than those of the Qale-Tol Aquifer (Adinehvand, 2017), providing enough energy for groundwater movement. In spite of the general flow direction parallel to the Malagha Anticline axis, the karst water flow path may be locally controlled by the karst media heterogeneity of fracture networks (Fig. 4) and the river mound. Heterogeneities within the aquifer media may be evident in the form of different fracture intensities and permeabilities (Fig. 4). In such conditions, the flow direction may locally affect water flows towards nearby fractures with larger widths or areas with higher permeabilities and lead the water to flows in multiple directions (Fig. 11c). These factors are prominent, especially in an aquifer with a flat water table and low hydraulic gradient. The flow in the third tracer test is toward the contact of the Pabdeh-Gurpi Formations with low velocity, instead of towards the Malagha Gorge. The main reason is the greater thickness of the river mound below the AR than the thickness of the river mound below the impermeable Pabdeh-Gurpi Formations with further distances from the river. The existence of the mound under the AR may cause water to move towards parts of the DMA below the Pabdeh-Gurpi Formations which have a negligible mound.

## Conclusions

This study integrated various and extensive data such as water table levels, hydrochemistry, stable isotopes, dye tracings, borehole logs (permeability and fracture zones), and geological settings to characterize a tectonized highland karst aquifer. The studied karst aquifer is located in the southern limb of the tectonized Malagha Anticline at the High Zagros Zone, bounded by the Malagha and Qale-Tol thrust faults. The impact of these two faults, the river crossing the aquifer, the mound below the river, and a flat water table have all resulted in a complex karst aquifer. The extensive

hydrological data collected for the construction of the Abolabbas Dam have provided a good basis to study the karst aquifer. The water balance of the Malagha Aquifer indicates that there was no inflow or outflow from the adjacent aquifers. The sources of the Malagha Aquifer water were recharge from precipitation and/or seepage from the Abolabbas River. The footprints of the river water, precipitation recharge, and the mix of these two sources were determined using hydrochemistry, stable isotopes ($\delta^{18}O$ and $\delta^{2}H$), and the water table levels in the boreholes.

The faults have two distinct hydrogeological impacts on the studied karst aquifer. On the one hand, Qale-Tol fault core acts as a barrier. The water table level differences on both sides of the Qale-Tol fault core and the exposed breccia confirm the barrier behavior of the fault core. On the other hand, the extensive fracture zones caused marly layers of the As2 Unit to lose their impermeability role, allowing a cross-unit flow. The existence of fracture zones resulted in more homogeneous media with relatively uniform water levels by increasing the groundwater flow cross-sectional area which are where two independent aquifers have been formed in the upstream and downstream of the fault core, respectively. The LRA is a small aquifer close to the Qale-Tol fault core probably with no hydraulic connection to the DMA. The DMA is located in a damage zone with extensive fractures crushed zones and minor faults. The two tracer tests indicated the velocities that are in the range of the laminar flow regime, and hence, a lack of main conduits. The water table levels of the DMA were almost flat and irregular, indicating that the karst water flows through extensive fractures which increases the total cross-sectional area of the flow and consequently reduces the velocity and hydraulic gradient. The extensive fracture zones, continuous high permeabilities, flat and irregular water table, and laminar flow regime by tracer tests suggested that there was no major conduit development and the karst water most probably flows through a network of solutionally-connected fractures. It seems that the karst water is distributed within extensive solutional fracture networks, similar to groundwater flow in inter-granular pores of alluvial aquifers.

The general flow direction of the DMA is parallel to the Qale-Tol thrust fault strike, towards the surrounding alluvial aquifer. However, the local heterogeneities such as fractures with larger apertures, a mound below the river, or a bedding plane dip may locally control the flow direction. Two boreholes in the vicinity of the Abolabbas River had water tables higher than the main aquifer and their electrical conductivities were significantly less than those of the Abolabbas River and the DMA, implying that the hydrological behavior near the fault core was complex due to the numerous hydrological and structural processes occurring around the fault core. Most of the research carried out on tectonized highland aquifers have focused either on the fault zones from a structural geological point of view, or on water table differences on both sides of the fault core. Research on the hydrogeology of damage zones, especially on karst aquifers under the impact of thrust faults, is limited due to the lack of borehole or exploitation well data from such elevated and rough topographies. The proposed approach can also be useful in other tectonically active regions with scarce data to characterize complex and tectonized karst systems.

## Acknowledgments

The authors acknowledge the Research Council of Shiraz University for their support of this work. We are grateful to Khuzestan Regional Power and Water Authority for their financial support. Special thanks are due to R. Averand and N. Damogh for helping with field work and data collection, to H. Zarei, M. Mahdavinejad and A. Negintaji for their cooperation on this project, and to A. Majd for providing parts of hydrogeological data and performing the first tracer test. The authors also thank Dr. Andreas Hartmann of the Institute of Hydrology, University of Freiburg for reviewing the first draft of the manuscript. Our thanks also go to the two anonymous reviewers for their constructive comments on the manuscript.

## References

Adinehvand, R., 2017, Evaluation of water leakage potential from Abolabbas Karst dam site using Hydrogeology, Modeling and Dye Tracing Methods [Ph.D. dissertation]: Shiraz, University of Shiraz, 126 p.

Adinehvand, R., Raeisi, E., and Hartmann, A., 2017, A step-wise semi-distributed simulation approach to characterize a karst aquifer and to support dam construction in a data-scarce environment: Journal of Hydrology. v. 554, p. 470 -481, doi:10.1016/j.jhydrol.2017.08.056.

Agosta, F., and Kirschner, D.L., 2003, Fluid conduits in carbonate-hosted seismogenic normal faults of central Italy: Journal of Geophysical Research: Solid Earth, v. 108, p. 1–13, doi: 10.1029/2002JB002013.

Alexander, K., 1990, Correlation of structural lineaments and fracture traces to water-well yields in the Edwards Aquifer, Central Texas [Ph.D. dissertation]: The University of Texas at Austin, https://repositories.lib.utexas.edu/handle/2152/46325.

American Public Health Association (APHA), 2005, Standard methods for the examination of water and wastewater: American Public Health Association , 20st edn. American Water Works Association (AWWA) and Water Environment Federation (WEF), Denver, New Jersey.

Anderson, E.I., and Bakker, M., 2008, Groundwater flow through anisotropic fault zones in multiaquifer systems: Water Resources Research, v. 44, no. W11433, p. 1−11, doi: 10.1029/2008WR006925.

Antonellini, M.A., Aydin, A., and Pollard, D.D., 1994, Microstructure of deformation bands in porous sandstones at Arches National Park, Utah: Journal of Structural Geology, v. 16, p. 941–959, doi: 10.1016/0191-8141(94)90077-9.

Apaydin, A., 2010, Relation of tectonic structure to groundwater flow in the Beypazari region, NW Anatolia, Turkey: Hydrogeology Journal, v. 18, p. 1343–1356, doi: 10.1007/s10040-010-0605-1.

Ashjari, J. and Raeisi, E., 2006, Influences of anticlinal structure on regional flow, Zagros, Iran: Journal of Cave and Karst Studies, v. 68, no. 3, p. 118−129. doi

Benedicto, A., Plagnes, V., Vergely, P., Flotte, N., and Schultz, R.A., 2008, Fault and fluid interaction in a rifted margin: integrated study of calcite-sealed fault-related structures (southern Corinth margin): Geological Society, London, Special Publications, v. 299, p. 257–275, doi: 10.1144/SP299.16.Bense, V.F., Gleeson, T., Loveless, S.E., Bour, O., and Scibek, J., 2013, Fault zone hydrogeology: Earth-Science Reviews, v. 127, p. 171–192, doi: 10.1016/j.earscirev.2013.09.008.

Bense, V.F., and Person, M.A., 2006, Faults as conduit-barrier systems to fluid flow in siliciclastic sedimentary aquifers: Water Resources Research, v. 42, doi: 10.1029/2005WR004480.

Bense, V.F., Person, M.A., Chaudhary, K., You, Y., Cremer, N., and Simon, S., 2008, Thermal anomalies indicate preferential flow along faults in unconsolidated sedimentary aquifers: Geophysical Research Letters, v. 35, p. L24406, doi: 10.1029/2008GL036017.

Bense, V.F., and Van Balen, R., 2004, The effect of fault relay and clay smearing on groundwater flow patterns in the Lower Rhine Embayment: Basin Research, v. 16, p. 397–411, doi: 10.1111/j.1365-2117.2004.00238.x.

Berberian, M., 1995, Master “blind” thrust faults hidden under the Zagros folds: active basement tectonics and surface morphotectonics: Tectonophysics, v. 241, p. 193–224, doi: 10.1016/0040-1951(94)00185-C.

Berberian, M., and King, G.C.P., 1981, Towards a paleogeography and tectonic evolution of Iran: Reply: Canadian Journal of Earth Sciences, v. 18, p. 1764–1766, doi: 10.1139/e81-163.

Billi, A., 2010, Microtectonics of low-P low-T carbonate fault rocks: Journal of Structural Geology, v. 32, p. 1392–1402, doi: 10.1016/j.jsg.2009.05.007.

Billi, A., Salvini, F., and Storti, F., 2003, The damage zone-fault core transition in carbonate rocks: implications for fault growth, structure and permeability: Journal of Structural Geology, v. 25, p. 1779–1794, doi: 10.1016/S0191-8141(03)00037-3.

Bonacci, O., 1995, Ground water behaviour in karst: example of the Ombla Spring (Croatia): Journal of Hydrology, v. 165, p. 113–134, doi: 10.1016/0022-1694(94)02577-X.

Bonacci, O., and Roje-Bonacci, T., 2000, Interpretation of groundwater level monitoring results in karst aquifers: examples from the Dinaric karst: Hydrological Processes, v. 14, p. 2423–2438, doi: 10.1002/1099-1085(20001015)14:14<2423::AID-HYP104>3.0.CO;2-2.

Bruhn, R.L., Parry, W.T., Yonkee, W. a, and Thompson, T., 1994, Fracturing and hydrothermal alteration in normal fault zones: Pure and Applied Geophysics, v. 142, p. 609–644, doi: 10.1007/BF00876057.

Caine, J.S., Evans, J.P., and Forster, C.B., 1996, Fault zone architechture and permeability structure: Geology, v. 24, p. 1025–1028, doi: 10.1130/0091-7613(1996)024<1025.

Caine, J.S., and Forster, C.B., 1999, Fault zone architecture and fluid flow: Insights from field data and numerical modeling: Geophysical Monograph Series, v. 113, p. 101–127, doi: 10.1029/GM113p0101.

Caine, J.S., and Minor, S.A., 2009, Structural and geochemical characteristics of faulted sediments and inferences on the role of water in deformatiion, Rio Grande Rift, New Mexico: Bulletin of the Geological Society of America, v. 121, p. 1325–1340, doi: 10.1130/B26164.1.

Cappa, F., Guglielmi, Y., Fénart, P., Merrien-Soukatchoff, V., and Thoraval, A., 2005, Hydromechanical interactions in a fractured carbonate reservoir inferred from hydraulic and mechanical measurements: International Journal of Rock Mechanics and Mining Sciences, v. 42, p. 287–306, doi: 10.1016/j.ijrmms.2004.11.006.

Cappa, F., Guglielmi, Y., and Virieux, J., 2007, Stress and fluid transfer in a fault zone due to overpressures in the seismogenic crust: Geophysical Research Letters, v. 34, doi: 10.1029/2006GL028980.

Celico, F., Petrella, E., and Celico, P., 2006, Hydrogeological behaviour of some fault zones in a carbonate aquifer of Southern Italy: An experimentally based model: Terra Nova, v. 18, p. 308–313, doi: 10.1111/j.1365-3121.2006.00694.x.

Chester, F.M., and Logan, J.M., 1986, Implications for mechanical properties of brittle faults from observations of the Punchbowl fault zone, California: Pure and Applied Geophysics, v. 124, p. 79–106, doi: 10.1007/BF00875720.

Craig, H., 1961, Isotopic variations in meteoric waters: Science, v. 133, p. 1702–1703, doi: 10.1126/science.133.3465.1702.

Doan, M.L., and Cornet, F.H., 2007, Thermal anomaly near the Aigio fault, Gulf of Corinth, Greece, maybe due to convection below the fault: Geophysical Research Letters, v. 34, p. L06314, doi: 10.1029/2006GL028931.

Emami, H., 2008, Foreland Propagation of Folding and Structure of the Mountain Front Flexure in the Pusht-E Kuh Arc (Zagros, Iran) [PhD thesis]: Barcelona, Universitat de Barcelona, 180 p., http://hdl.handle.net/2445/34914.

Falcon, N.L., 1961, Major earth-flexing in the Zagros Mountains of southwest Iran: Quarterly Journal Geological Society of London, v. 117, p. 367–376.

Falcon, N.L., 1974, Southern Iran: Zagros Mountains: Geological Society, London, Special Publications, v. 4, p. 199–211, doi: 10.1144/GSL.SP.2005.004.01.11.

Faoro, I., Niemeijer, A., Marone, C., and Elsworth, D., 2009, Influence of shear and deviatoric stress on the evolution of permeability in fractured rock: Journal of Geophysical Research, v. 114, p. B01201, doi: 10.1029/2007JB005372.

Faroughi, A., 2009, Determination of isotopic characteristics of rain in Fars province: Shiraz University, 89 p.

Ferrill, D.A., and Morris, A.P., 2003, Erratum to: “Dilational normal faults”: Journal of Structural Geology, v. 25, p. 827, doi: 10.1016/S0191-8141(02)00196-7.

Ferrill, D.A., Sims, D.W., Waiting, D.J., Morris, A.P., Franklin, N.M., and Schultz, A.L., 2004, Structural framework of the Edwards Aquifer recharge zone in south-central Texas: Bulletin of the Geological Society of America, v. 116, p. 407–418, doi: 10.1130/B25174.1.

Goddard, J. V., and Evans, J.P., 1995, Chemical changes and fluid-rock interaction in faults of crystalline thrust sheets, northwestern Wyoming, U.S.A.: Journal of Structural Geology, v. 17, p. 533–547, doi: 10.1016/0191-8141(94)00068-B.

Goldscheider, N., 2005, Fold structure and underground drainage pattern in the alpine karst system Hochifen-Gottesacker: Eclogae Geologicae Helvetiae, v. 98, p. 1–17, doi: 10.1007/s00015-005-1143-z.

Goldscheider, N., and Hoetzl, H., 1999, Hydrogeological characteristics of folded alpine karst systems exemplified by the Gottesacker Plateau (German-Austrian Alps): Acta Carsologica, v. 28, p. 87–103.

Goldscheider, N., and Neukum, C., 2010, Fold and fault control on the drainage pattern of a double-karst-aquifer system, Winterstaude, Austrian Alps: Acta Carsologica, v. 39, p. 173–186, doi: 10.3986/ac.v39i2.91.

Gremaud, V., Goldscheider, N., Savoy, L., Favre, G., and Masson, H., 2009, Geological structure, recharge processes and underground drainage of a glacierised karst aquifer system, Tsanfleuron-Sanetsch, Swiss Alps: Hydrogeology Journal, v. 17, p. 1833–1848, doi: 10.1007/s10040-009-0485-4.

Hamaker, S., and Harris, R., 2007, Fault-related ground-water compartmentalization in the East Tintic Mining District, Utah: *in:* Willis, G.C., Hylland, M.D., Clark, D.L., and Chidsey, T.C., Jr., eds, Central Utah– Diverse geology of a dynamic landscape. Utah Geological Association Publications, Salt Lake City, Utah, v. 123, p. 405–423.

Hartmann, A., Mudarra, M., Andreo, B., Marín, A., Wagener, T., and Lange, J., 2014, Modeling spatiotemporal impacts of hydroclimatic extremes on groundwater recharge at a Mediterranean karst aquifer: Water Resources Research, v. 50, p. 6507–6521, doi: 10.1002/2014WR015685.

Hoetzl, H., 1998, Karst groundwater, *in* Kass, W. ed., Tracing Technique in Geohydrology, Balkema, p. 398–426.

Hovorka, S.D., Mace, R.E., and Collins, E.W., 1998, Permeability structure of the Edwards Aquifer, south Texas: implications for aquifer management: Bureau of Economic Geology, University of Texas at Austin.

Jourde, H., Pistre, S., Perrochet, P., and Drogue, C., 2002, Origin of fractional flow dimension to a partially penetrating well in stratified fractured reservoirs. New results based on the study of synthetic fracture networks: Advances in Water Resources, v. 25, p. 371–387, //000175890300002.

Kim, Y.-S., and Sanderson, D.J., 2010, Inferred fluid flow through fault damage zones based on the observation of stalactites in carbonate caves: Journal of Structural Geology, v. 32, p. 1305–1316, doi: 10.1016/j.jsg.2009.04.017.

Kostakioti, A., Xypolias, P., Kokkalas, S., and Doutsos, T., 2004, Quantitative analysis of deformation along the fault damage zone of the Klimatia Thrust (NW Greece, Ionian Zone): Bulletin of the Geological Society of Greece, v. XXXVI, p. 1643–1651.

Koukouvelas, I.K., and Papoulis, D., 2009, Fluid involvement in the active Helike normal Fault, Gulf of Corinth, Greece: Journal of Structural Geology, v. 31, p. 237–250, doi: 10.1016/j.jsg.2008.11.018.

Kresic, N., 2010, Modeling, *in* Kresic, N. and Stevanovic, Z. eds., Groundwater Hydrology of Karst Springs, Butterworth-Heinemann, p. 573.

Leray, S., de Dreuzy, J.-R., Bour, O., Labasque, T., and Aquilina, L., 2012, Contribution of age data to the characterization of complex aquifers: Journal of Hydrology, v. 464–465, p. 54–68, doi: 10.1016/j.jhydrol.2012.06.052.

Lindgren, R.J., Dutton, A.R., Hovorka, S.D., Worthington, S.R.H., and Painter, S., 2004, Conceptualization and simulation of the Edwards Aquifer, San Antonio Region, Texas. Scientific Investigations Report 2004 – 5277, 143 p. https://pubs.usgs.gov/sir/2004/5277/pdf/sir2004-5277.pdf

Maclay, R., 1995, Geology and hydrology of the Edwards Aquifer in the San Antonio area, Texas:, https://pubs.er.usgs.gov/publication/wri954186.

Mahab Ghodss Consulting, and Engineers, 2004, Climatology Report, The first stage: Mahab Ghodss Consulting Engineers (in Farsi).

Majd, A., 2011, Hydrogeological and dye tracing studies of Abolabbas dam, Khuzestan [MS. Thesis]: Shiraz, Shiraz University, 177 p.

Mayer, A., May, W., Lukkarila, C., and Diehl, J., 2007, Estimation of fault-zone conductance by calibration of a regional groundwater flow model: Desert Hot Springs, California: Hydrogeology Journal, v. 15, p. 1093–1106, doi: 10.1007/s10040-007-0158-0.

Mayer, J.R., and Sharp, J.M., 1998, Fracture control of regional ground-water flow in a carbonate aquifer in a semi-arid region: Bulletin of the Geological Society of America, v. 110, p. 269–283, doi: 10.1130/0016-7606(1998)110<0269:FCORGW>2.3.CO;2.

McGrath, A.G., and Davison, I., 1995, Damage zone geometry around fault tips: Journal of Structural Geology, v. 17, p. 1011–1024, doi: 10.1016/0191-8141(94)00116-H.

Micarelli, L., Moretti, I., Jaubert, M., and Moulouel, H., 2006, Fracture analysis in the south-western Corinth rift (Greece) and implications on fault hydraulic behavior: Tectonophysics, v. 426, p. 31–59, doi: 10.1016/j.tecto.2006.02.022.

Miliaresis, G., 2001, Geomorphometric mapping of Zagros Ranges at regional scale: Computers and Geosciences, vol. 27: p. 775-786, doi. org/10.1016/S0098-3004(00)00168-0

Najmeddin, A., Keshavarzi, B., Moore, F., and Lahijanzadeh, A., 2017, Source apportionment and health risk assessment of potentially toxic elements in road dust from urban industrial areas of Ahvaz megacity, Iran: Environmental Geochemistry and Health, p. 1–22, doi: 10.1007/s10653-017-0035-2.

Nassery, H., 1991, Hydrogeological studies of karst springs in the catchment area of Droodzan Dam [MS. thesis]: Shiraz University, (in Farsi).

Pezeshkpour, P., 1991, Hydrogeological and hydrochemical evaluation of Kuh-e Gar-Barm- Firooz springs [MS. thesis]: Shiraz University, (in Farsi).

Plan, L., Decker, K., Faber, R., Wagreich, M., and Grasemann, B., 2009, Karst morphology and groundwater vulnerability of high alpine karst plateaus: Environmental Geology, v. 58, p. 285–297, doi: 10.1007/s00254-008-1605-5.

Raeisi, E., and Kowsar, N., 1997, Development of Shahpour Cave, southern Iran: Cave and Karst Science, v. 24, p. 27–34.

Rahnemaaie, M., 1994, Evaluation of infiltration and runoff in the karstified carbonatic rocks [MS. thesis]: Shiraz, University of Shiraz, (in Farsi).

Rugh, D.F., and Burbey, T.J., 2008, Using saline tracers to evaluate preferential recharge in fractured rocks, Floyd County, Virginia, USA: Hydrogeology Journal, v. 16, p. 251–262, doi: 10.1007/s10040-007-0236-3.

Sepehr, M., and Cosgrove, J.., 2004, Structural framework of the Zagros Fold–Thrust Belt, Iran: Marine and Petroleum Geology, v. 21, p. 829–843, doi: 10.1016/j.marpetgeo.2003.07.006.

Sherkati, S., and Letouzey, J., 2004, Variation of structural style and basin evolution in the central Zagros (Izeh zone and Dezful Embayment), Iran: Marine and Petroleum Geology, v. 21, p. 535–554, doi: 10.1016/j.marpetgeo.2004.01.007.

Sherkati, S., Molinaro, M., Frizon de Lamotte, D., and Letouzey, J., 2005, Detachment folding in the Central and Eastern Zagros fold-belt (Iran): salt mobility, multiple detachments and late basement control: Journal of Structural Geology, v. 27, p. 1680–1696, doi: 10.1016/j.jsg.2005.05.010.

Shipton, Z.K., Evans, J.P., and Thompson, L.B., 2005, The geometry and thickness of deformation-band fault core and its influence on sealing characteristics of deformation-band fault zones: Aapg Memoir, v. 85, p. 181–195, doi: 10.1306/1033723M853135.

Solum, J.G., and Huisman, B.A.H., 2016, Toward the creation of models to predict static and dynamic fault-seal potential in carbonates: Petroleum Geoscience, p. petgeo2016-044, doi: 10.1144/petgeo2016-044.

Stocklin, J., 1968, Structural historiy and tectonics of Iran: A review: The American Association of Petroleum Geologists Bulletin, v. 52, p. 11258–12229.

Surrette, M.J., and Allen, D.M., 2008, Quantifying heterogeneity in variably fractured sedimentary rock using a hydrostructural domain: Geological Society of America Bulletin, v. 120, p. 225–237, doi: 10.1130/B26078.1.

Tesei, T., Collettini, C., Viti, C., and Barchi, M.R., 2013, Fault architecture and deformation mechanisms in exhumed analogues of seismogenic carbonate-bearing thrusts: Journal of Structural Geology, v. 55, p. 167–181, doi: 10.1016/j.jsg.2013.07.007.

Wermund, E., Cepeda, J.C., and Luttrell, P.., 1978, Regional distribution of fractures in the southern Edwards Plateau and their relationship to tectonics and caves: Bureau of Economic Geology, University of Texas at Austin, 14 p.

Keith Muhlestein, Laurence Meissner, Richard Klar, and Ronald T. Green. Three-dimensional electrical resistivity for detection of subsurface karst associated with Friesenhahn Cave. *Journal of Cave and Karst Studies*, v. 80, no. 4, p. 206-211. DOI:10.4311/2018ES0101

# THREE-DIMENSIONAL ELECTRICAL RESISTIVITY FOR DETECTION OF SUBSURFACE KARST ASSOCIATED WITH FRIESENHAHN CAVE

Keith Muhlestein[1, C], Laurence Meissner[2], Richard Klar[3], and Ronald T. Green[4]

Abstract

Electrical resistivity imaging techniques have proven to be an effective technological advancement for detecting subsurface karst features in carbonate formations. Numerous variables, such as electrode configurations, moisture conditions, carbonate lithology, and structure, can affect how effectively and accurately the generated images replicate actual underground features. This study investigates the electrical resistivity of Friesenhahn Cave and the surrounding strata and attempts to predict the morphology of what are believed to be extensions to the currently known single chamber of Friesenhahn Cave. Current observations within the known cave clearly show a collapsed entrance, which has been dated to the Pleistocene. Observations of water flow, as well as the collapse of sediments from sections of the cave floor, indicate a potentially significantly-sized additional passage extending beyond the known cave. Electrical resistivity results also provide an opportunity to determine the point of easiest access to the extension chambers so as to minimize the excavation efforts needed to obtain physical access to them from the existing cave. Assuming access to those chambers, physical measurements of the extension chambers will be used to confirm the results of the dipole-dipole array.

## Introduction

An electrical resistivity survey was conducted at the Friesenhahn Cave in north San Antonio, Texas (Fig. 1). The purpose of the survey was to identify and evaluate potential karst features (i.e., caves and solution cavities) in the shallow subsurface (i.e., to depths of approximately 40 ft) that extend beyond the extent of the known cave. An electrical resistivity survey was performed because this technique can effectively delineate areas in the subsurface, where caves and solution cavities might be present.

The electrical contrasts between competent limestone, filled voids, and karst features can create conditions favorable for high-resolution electrical resistivity surveys to detect anomalies in the electrical properties of the subsurface. Air-filled voids, which can vary in size from caves (i.e., large enough for a person to enter) to solution cavities (i.e., sub-centimeter to approximately one meter in scale), can have a distinctly different electrical signature (e.g., more resistive) relative to the surrounding limestone. Clay-filled voids also have a distinctly different electrical signature (e.g., more conductive) relative to the surrounding limestone.

Given this diversity in the electrical signature exhibited by karst features, detection of karst features using electrical resistivity can be complicated (Green, et.al., 2013). General observations can be summarized as follows:

- Large air-filled voids typically appear as electrically resistive.
- Large water-filled voids typically appear as electrically conductive.
- Small air-filled voids can appear as either electrically resistive or conductive.
- Clay-filled voids can appear as electrically conductive.
- Clay-, water-, and air-filled voids may not have an electrical signature in the survey results if the void is not sufficiently large.
- Voids are recognizable in electrical survey results when a combination of electrical contrast between the void and the host rock, and the size of the void is sufficiently large. Smaller voids may be detected in cases where the electrical contrast is greater.

The key to these observations is that signatures of the features appear as anomalies when compared with the host rock, provided the host rock has a relatively uniform electrical signature. Subsurface electrical resistivity survey results of the known cave will be compared with areas adjacent to the known cave to indicate where additional cave passages might extend. These results will be verified by excavation and drilling. Survey results will guide excavation and drilling locations, where additional unknown cave passages have been indicated.

The electrical resistivity survey was conducted using a Syscal Pro electrical resistivity system (IRIS Instruments, Orleans, France). The electrical properties of the geologic section beneath the rectangular survey areas were modeled to a depth of approximately 12 m (40 ft). The measured resistivity data were inverted to provide an interpretation of the subsurface.

[1] P.O. Box 728, Helotes, TX 78023, Keith.Muhlestein@gmail.com
[2] 450 Spring Valley St., Hutto TX 78634, laurence.meissner@concordia.edu
[3] 9108 Brigadoon, San Antonio, TX 78254, rklar@rkci.com
[4] 14255 Antonio Dr., Helotes, TX 78023, ronald.green@swri.org
[C] Corresponding Author

Figure 1. Modern entrance shaft of Friesenhahn Cave, looking up the ladder.

## Site Description

Friesenhahn Cave is located in northern Bexar County, Texas, west of US 281 and north of Stone Oak Boulevard (Fig. 2). The area is known for significant karst development and contains dozens of named caves as well as numerous unnamed sinkholes and unexplored cavities (Veni, 1988). Located within the Balcones fault zone, the cave appears to have developed adjacent to a fault plane. The cave initially formed as a phreatic chamber in the basal, nodular section of the Kainer Formation, Edwards Group. However, with the drop of the water table, the cave became subject to vadose zone processes, including significant calcite deposition.

The known portion of Friesenhahn Cave consists of a single, oval-shaped chamber, about 18 m long and 10 m wide, with a ceiling height of about 2.5 m (Fig. 3). Located about nine meters below the surface, the known chamber is accessed by a vertical shaft, approximately two meters in diameter, that was caused in part by solution and part by collapse. Narrow gaps (five to 10 cm wide) drop down approximately one meter along the edges of the cave floor walls. These openings appear to curve outward beyond view and beyond access. Significant volumes of water flow through these gaps during rain events, which adds further evidence of adjacent, yet-undiscovered chambers and a direct conduit to the aquifer.

Friesenhahn Cave is interpreted as having a paleo-entrance, now filled by natural debris comprised of breakdown and soils. The paleo-entrance, located at the northwest end of the Friesenhahn Cave,

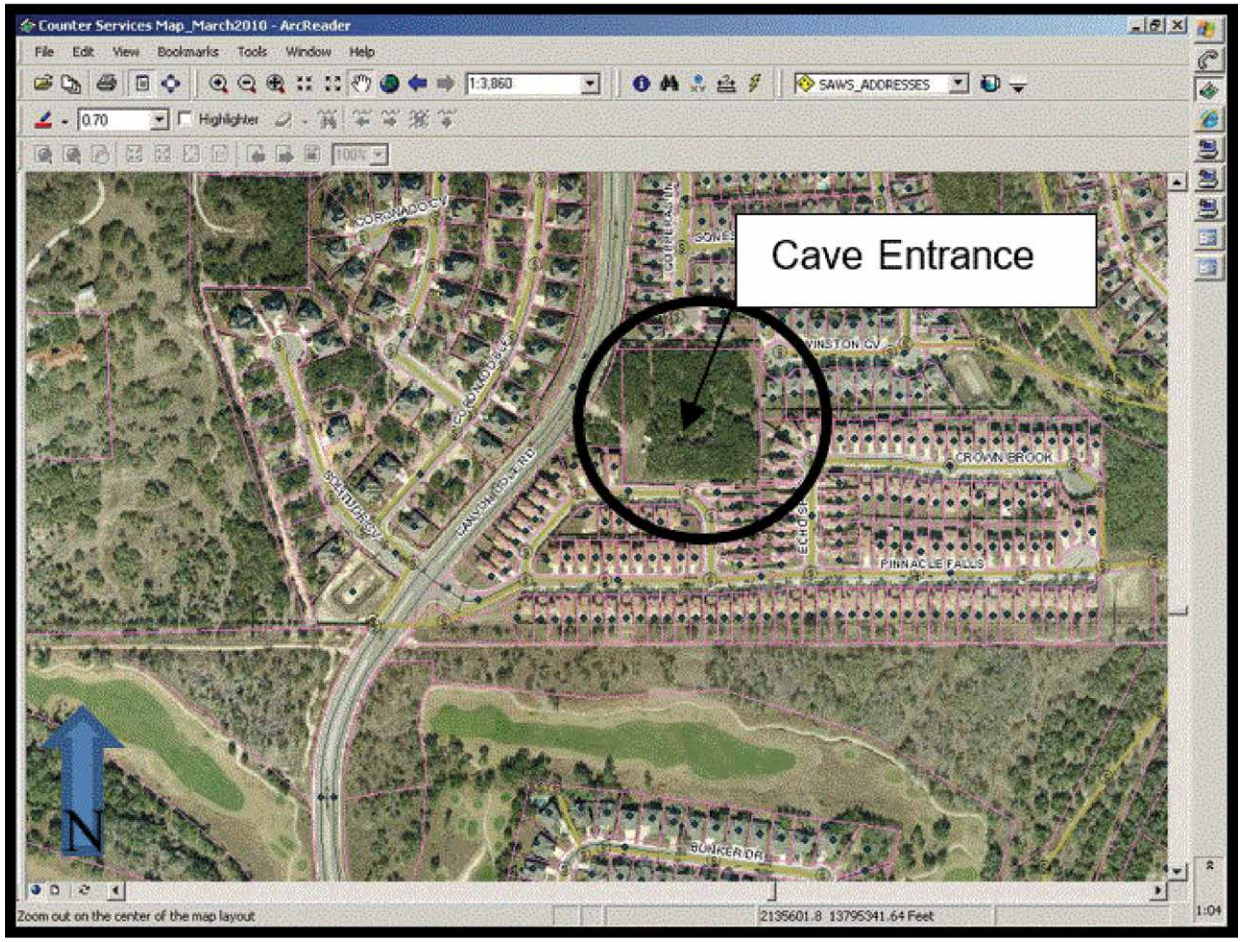


Figure 2. Friesenhahn Cave located on a small parcel, surrounded by residential development.

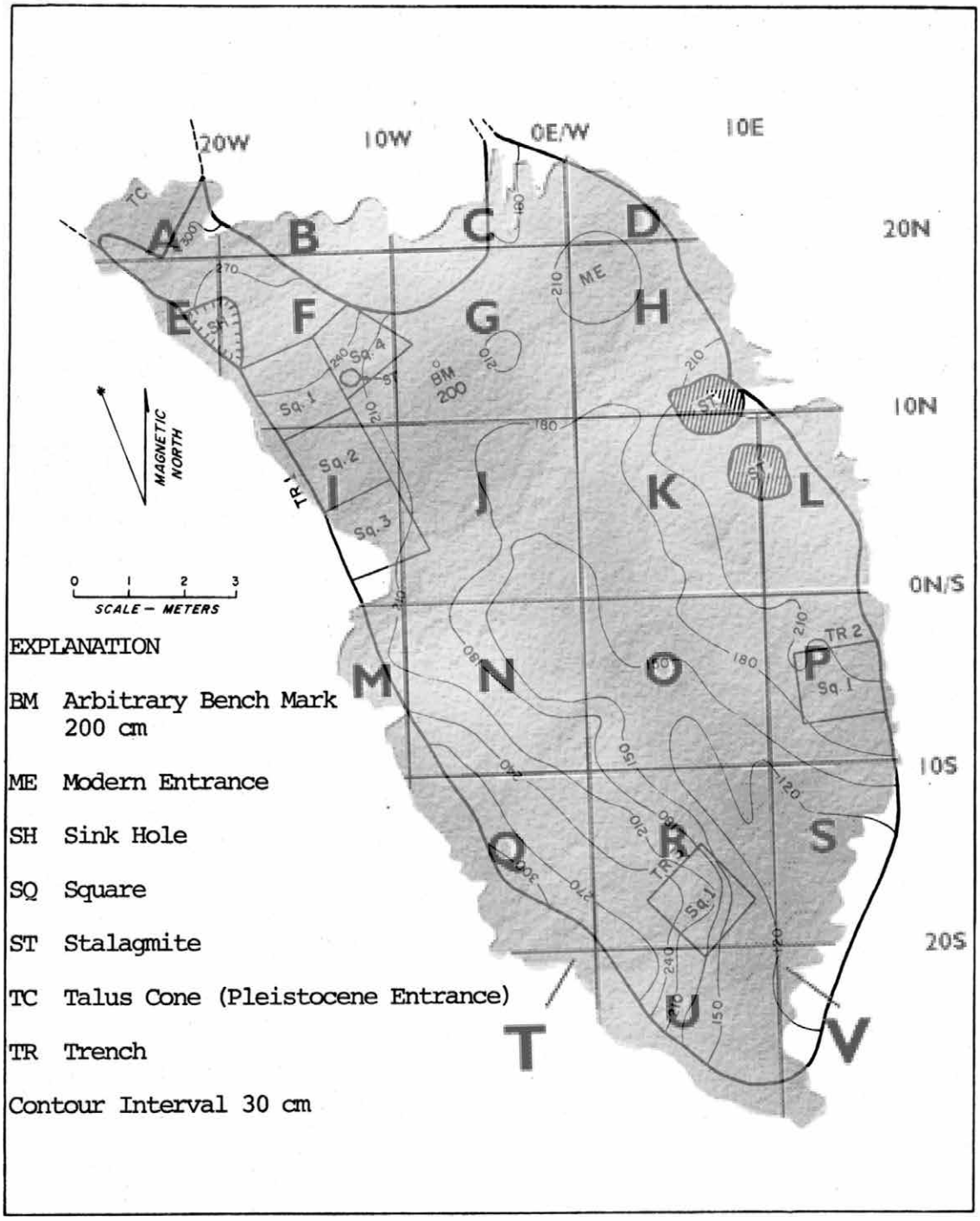


Figure 3. Map of Friesenhahn Cave (Graham, 1976).

has been frequently explored since its initial discovery in 1915. Notable are scientific expeditions by The University of Texas in 1949 and 1951, at the invitation of Mr. Alfred Friesenhahn (Milstead, 1956). Sediments within the main chamber of the cave have yielded thousands of bones from numerous vertebrate groups, including over 30 genera of mammals. In fact, Friesenhahn Cave has probably produced more significant fossils of Pleistocene vertebrates than any other site in North America, except LaBrea Tar Pits in California (Lundelius, 1967). Large deposits of unexhumed fossils can also be seen in the sediment and collapsed rock debris along the edges of the cave floor. In addition, surface collapse, at the north end of the main chamber, appears to block access to possible cavity extensions that conceivably could yield vertebrate fossils that utilized this site as a shelter earlier in the Pleistocene.

**Survey Techniques**

Three-dimensional electrical resistivity measurements were taken across four grids of 35 m by 55 m. The four grids overlapped by one electrode row in both the x and y directions with the vertex being located directly over the entrance shaft of Friesenhahn Cave. Final total combined grid size is 70 m by 110 m. Dipole- dipole electrical resistivity data were taken using a Syscal Pro Switch 96 electrical resistivity system (IRIS Instruments). The layout included a 12 by 8 electrode grid at 5 m spacing. Earth Imager 3D (Advanced Geosciences Inc., Austin, TX) was used for data inversion.

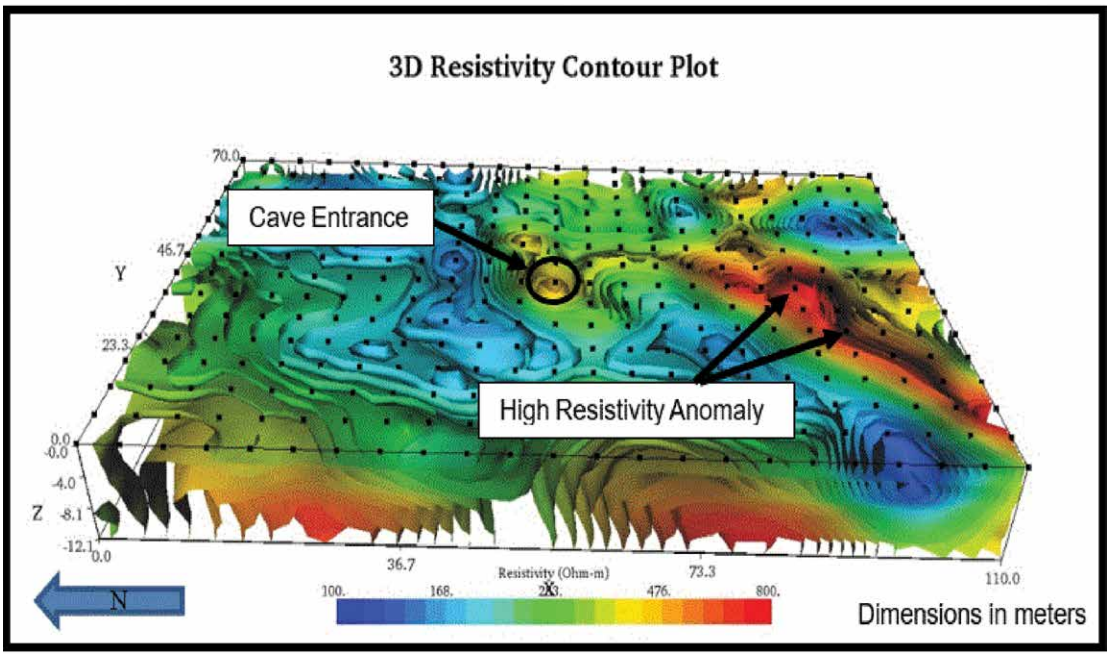


Figure 4. Resistivity contours illustrate the Friesenhahn Cave area. Black dots represent electrode placements and are five meters apart.

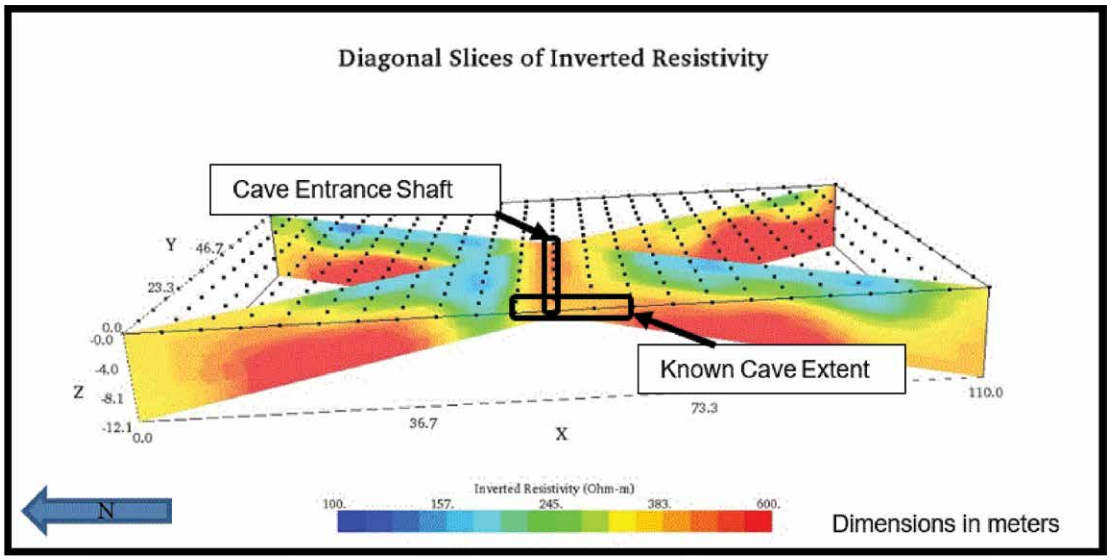


Figure 5. Diagonal cross-section vertex through the center of the cave shaft entrance.

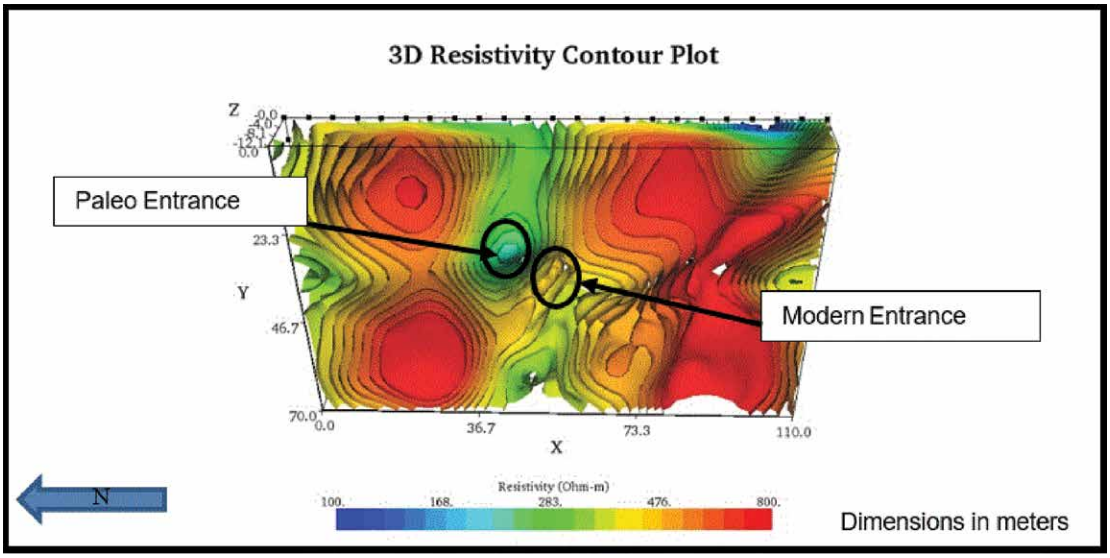


Figure 6. View from underneath revealing both Paleo and modern entrances.

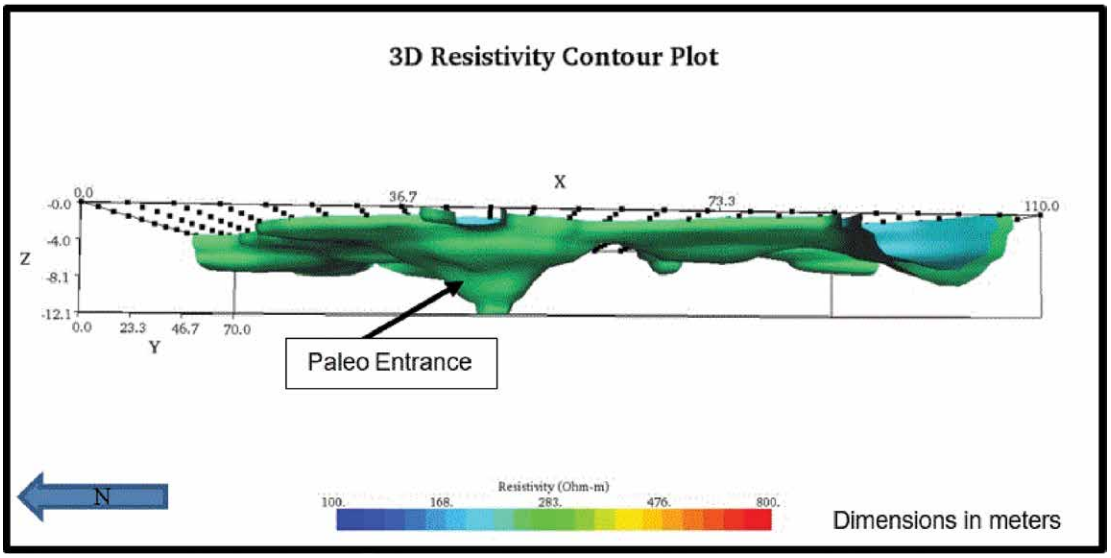


Figure 7. With resistivity values for the modern cave entrance removed, the Paleo entrance is evident.

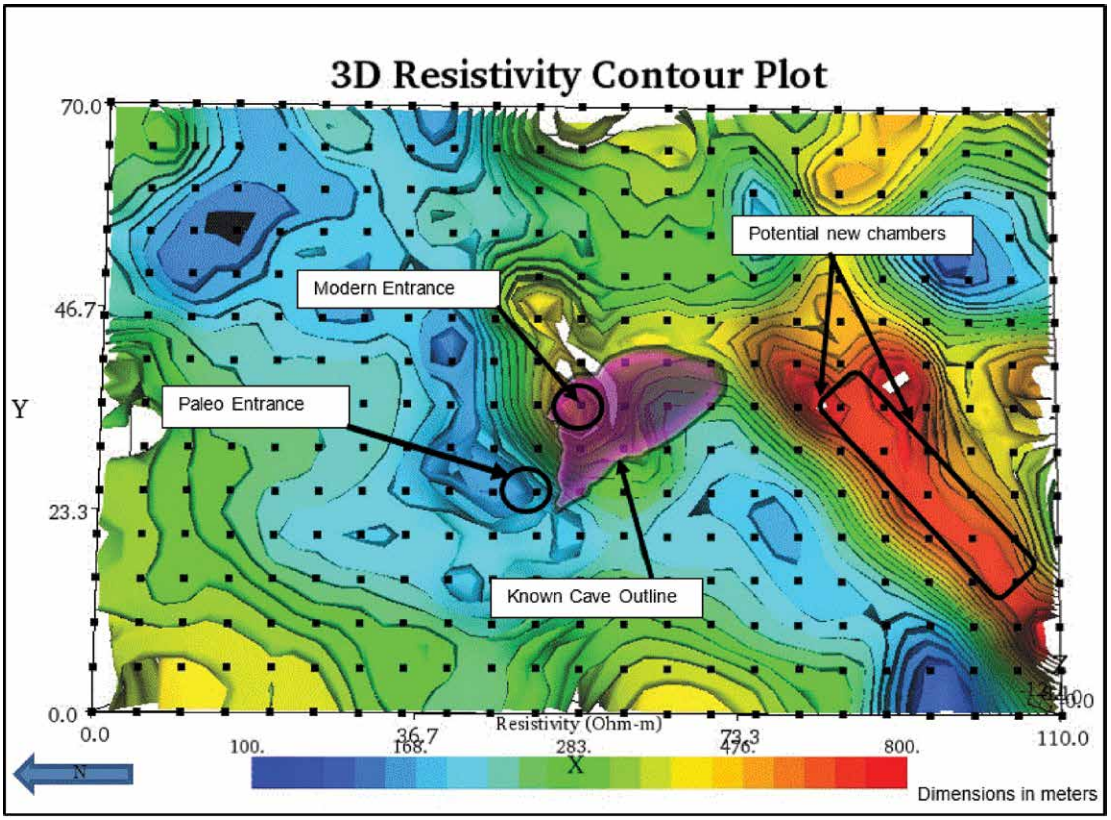


Figure 8. Top view, Cave in center magenta overlay, Paleo entrance left of center, and interpreted new chamber to right center.

**Results and Discussion**

Three-dimensional electrical resistivity results are provided in the following illustrations. They graphically show the electrical properties of the subsurface around Friesenhahn Cave. The models of inverted resistivity for the dipole-dipole data are illustrated as two-dimensional cross-sections, and three-dimensional block diagrams. Resistivity values range from approximately 100 to 800 ohm-m.

Located in the center of the grid in Figure 4, the known cave entrance indicates moderately high resistivity (i.e., yellow at approximately 350-400 ohm-m). The surface is shown to have relatively low resistivity (i.e., blue and green at less than approximately 250 ohm-m), with an exception of a NE-SW-trending zone from near the cave entrance (yellow) to the SW of the survey grid, which has electrical resistivity in excess of 500 ohm-m (orange), and as high as 800 ohm-m (red).

Two intersecting vertical cross-sections of electrical resistivity values are illustrated in Figure 5. The two vertical cross-sections are centered over the cave entrance. The entrance shaft is illustrated in orange with a resistivity of

approximately 375 ohm-m. Relatively high electrical resistivity (i.e., approximately 400 ohm-m and higher, orange and red) may indicate undefined karst conduits. These interpretations suggest that void spaces correlate with high electrical resistivity. This is consistent with the known, modern cave entrance and the absence of clay materials on the interior walls of either the cave entrance or the main cave chamber.

Figure 6 is a bottom view of the resistivity results with North to the left. The center of the grid is the base of the cave shaft entrance with a resistivity value of approximately 400 ohm-m. Electrical resistivity in excess of 500 ohm-m is evident elsewhere at the bottom of the block diagram.

Resistivity contours within the block diagram with values of 175−250 ohm-m are illustrated in Figure 7. Resistivity contours outside that range have been removed from this image to obscure the modern entrance. The resultant image reveals only the Paleo entrance, located approximately 10 m NW of the modern entrance. These relatively low electrical resistivity zones are interpreted as the collapsed entrance, once used by animals to access the cave during the Pleistocene Period (paleo-entrance). A debris-filled depression currently exists on the surface and marks the entrance to the collapsed feature. The collapse is evident within the cave as well, and it contains abundant fossil remains.

Figure 8 is a top view of the resistivity plot with the cave entrance at the center and the extent of the known cave illustrated in magenta. Clearly visible in the resistivity plot is a potential passage extending from near the known cave chamber, seen at the center of the grid in yellow, extending south (to the right in this image) approximately 20 m, then encountering a significantly higher resistivity zone, as high as 800 Ohm-m, represented in red. Significant volumes of water have been observed flowing into Friesenhahn Cave and passing through undefined karst conduit.

This geophysical analysis used dipole-dipole measures in a 110 m by 55 m grid centered on the entrance shaft of Friesenhahn Cave in northern Bexar County Texas with five-meter electrode spacing. The ground moisture level was very high; probably near saturation, as it had been raining heavily for several days, right up to the morning of the data collection. The cave itself was thoroughly soaked with water running down the walls and ceiling.

## Conclusions

The three-dimensional electrical resistivity survey completed at Friesenhahn Cave, using dipole-dipole array, revealed significant potential open voids as yet unseen and unconfirmed. It is expected that the next step in Friesenhahn research will include confirmation of this interpretation by drilling the most probable voids associated with the cave system. With the strength of the data, confidence is high that the interpretation is correct and will lead to discovery of more cave passages.

## References

Graham, R.W., 1976. Pleistocene and Holocene mammals, taphonomy, and paleoecology of the Friesenhahn Cave local fauna, Bexar County.

Graham, Russell W., Lundelius, E.L., Jr., Meissner, L., Muhlestein, K., 2013, Friesenhahn Cave: Late Pleistocene paleoecology and predator-prey relationships of mammoths with an extinct scimitar cat. Field Guides 30: 15-31. https://doi.org/10.1130/2013.0030(02).

Green, R.T., Prikryl, J., Morales, M., 2013, Electrical Resistivity Survey, Texas Department of Transportation Survey at Loop 1604 & State Highway 151, San Antonio, Texas.

Lundelius, E.L. Jr., 1967, Late-Pleistocene and Holocene faunal history of central Texas. Pleistocene extinctions: The search for a cause, pp. 288-319.

Milstead, W.W., 1956, Fossil turtles of Friesenhahn Cave, Texas, with the description of a new species of Testudo, Copeia, 1956(3), pp.162-171. https://doi.org/10.2307/1439631.

Prikryl, J., McGinnis, R., Green, R., 2007, Evaluation of Three-Dimensional Electrical Resistivity Array Types for Optimal Detection of Voids in Karstic Limestone.

Veni, G., 1988, The Caves of Bexar County, Second Ed., Texas Memorial Museum Speleological Monographs, 2, The University of Texas at Austin, Austin, TX, 300p.

Ting-Yong Li, Chun-Xia Huang, Lijun Tian, Marina B. Suarez, and Yongli Gao. Variation of $\delta^{13}C$ in plant-soil-cave systems in karst regions with different degrees of rocky desertification in southwest China. *Journal of Cave and Karst Studies*, v. 80, no. 4, p. 212-228. DOI:10.4311/2018ES0107

# VARIATION OF $\delta^{13}C$ IN PLANT-SOIL-CAVE SYSTEMS IN KARST REGIONS WITH DIFFERENT DEGREES OF ROCKY DESERTIFICATION IN SOUTHWEST CHINA AND IMPLICATIONS FOR PALEOENVIRONMENT RECONSTRUCTION

Ting-Yong Li[1, 2, C], Chun-Xia Huang[1], Lijun Tian[3], Marina B. Suarez[3], Yongli Gao[3]

Abstract

Speleothem $\delta^{13}C$ has been taken as an indicator of the history of rocky desertification, and changes in $\delta^{13}C$ have been thought to reflect the transition between C3 and C4 surface vegetation types. In this study the $\delta^{13}C$ values of plants, soil organic matter (SOM), dissolved inorganic carbon (DIC) of waters and modern calcite deposits in caves were investigated at five sites with different rocky desertification degree (RDD) in Southwest China. The main results can be summarized as follows: (1) dominant vegetation was the C3 type, with average plant $\delta^{13}C$ values ranging from $-26$ ‰ to $-32$ ‰ (V-PDB), and SOM $\delta^{13}C$ values ranging from $-20$ ‰ to $-25$ ‰ (V-PDB) for all the sites; (2) large variation for the $\delta^{13}C$ of DIC from drip water and modern calcite deposits in caves, which must be the result of multiple, inorganic factors in the epikarst zone and not the local vegetation type; (3) a proposed conceptual model to demonstrate that the evolution of Asian summer monsoon (ASM) can be recorded in speleothem $\delta^{13}C$ due to changes in epikarst zone hydrological conditions, exerting influence on stable carbon isotopes' fractionation, and not necessarily due to changing vegetation types in the subtropical zone of Southwest China.

## Introduction

Karst is one of the most fragile and vulnerable environments because of the low soil formation rate and high permeability of carbonate rocks. Rocky desertification is defined as the transformation of vegetation- and soil-covered karst areas into rocky landscape under the action of natural processes of hydrology and ecology, and through human activities (Yuan 1997; Jiang et al., 2014). The causes for initiation and development of rocky desertification, including the contributions from natural processes and human activities, are still unknown. To prevent and rehabilitate rocky desertification of karst areas, it is essential to know the history of rocky desertification for a specific region.

Speleothems in karst caves record climatic and ecologic information in geochemical proxies, such as the stable isotopes of oxygen and carbon ($\delta^{18}O$ and $\delta^{13}C$), and the concentrations of several elements (Fairchild et al., 2006). $\delta^{13}C$ and $\delta^{18}O$ have been the most popular proxies in the reconstruction of paleoclimate and paleoenvironmental changes (Dorale et al., 1992; Genty et al., 2003; Fairchild et al., 2006). $\delta^{13}C$ of soil $CO_2$ is controlled by the proportion of biomass from C3 and C4 plants and the $CO_2$ respiration of soil in different climatic conditions (Cerling, 1984; Mattey et al., 2016). It is considered that the variations of speleothem $\delta^{13}C$ can reflect the changes of regional vegetation, because the different photosynthetic pathways of different plant types result in different $\delta^{13}C$ values: C4 vegetation has much higher $\delta^{13}C$ (typically around $-12$ ‰), while carbon isotopic composition of C3 vegetation is close to $-25$ ‰ (McDermott, 2004); the $\delta^{13}C$ of associated speleothems is $-6$ ‰ to $+2$ ‰ with overlying C4 plants, and $-14$ ‰ to $-6$ ‰ with overlying C3 plants (Salomons and Mook, 1986, p. 241–269; McDermott, 2004). However, direct correlation of the speleothem $\delta^{13}C$ with regional vegetation is a simplified or idealized understanding. In reality, complex processes in soil and the epikarst zone will influence the migration of carbon isotopes and disturb the correlation between the speleothem geochemistry and overlying vegetation (Hendy, 1971; Salomons and Mook, 1986, p. 241–269; Coplen et al., 1994; Bar-Matthews et al., 1996; Baker et al., 1997; Fairchild et al., 2006; Frisia et al., 2011). The most recent publications have emphasized the influence of regional, hydrological circulation and the soil humidity balance on stalagmite $\delta^{13}C$ (Li et al., 2007; Liu et al., 2016).

Rocky desertification is a serious ecological and environmental problem in Southwest China (Jiang et al., 2014). In order to understand the origin and history of regional, rocky desertification, research on the mechanism of carbon isotope migration in karst systems, based on cave monitoring, has been carried out (Luo et al., 2009; Li et al., 2011, 2012). As well, reconstruction of the evolution of regional vegetation via the $\delta^{13}C$ records of speleothems has been done (Li et al., 1998). Li et al. (2012) studied the transition of $\delta^{13}C$ signals from overlying plants, soil, and bedrock, in cave water and modern deposits in Furong Cave, Southwest China. However, investigation of the $\delta^{13}C$ characteristics of modern plants and soils in karst regions with different rocky desertification degree (RDD) has been rare.

[1] Chongqing Key Laboratory of Karst Environment, School of Geographical Sciences, Southwest University, Chongqing, 400715
[2] Field Scientific Observation & Research Base of Karst Eco-environments at Nanchuan in Chongqing, Ministry of Land and Resources of China, Chongqing 408435, China
[3] Department of Geological Sciences, University of Texas at San Antonio, San Antonio, TX 78249, USA
[C] Corresponding author: cdlty@swu.edu.cn

In this paper, the organic carbon $\delta^{13}C$ of living plants (including leaves, branches, stems and roots) and soil at five sites with different rocky desertification degree (RDD) in Southwest China was investigated. In addition, the $\delta^{13}C$ of dissolved inorganic carbon (DIC-$\delta^{13}C$) of cave water in three caves was also monitored. This will increase knowledge about modern vegetation of karst areas in subtropical Southwest China, the transition of $\delta^{13}C$ signals in the epikarst zone with different RDD, and provide greater insight for paleoenvironment reconstruction via speleothem $\delta^{13}C$.

## Study Area

The most typical karst landscapes in China are concentrated in Southwest China. Four research sites with different RDD were chosen (Nanchuan, Guanling, Liuzhi and Panxian) (Fig. 1, Table 1) and a previous case study above Furong Cave (Wulong County, Chongqing City) (Li et al., 2012) was used as a comparison.

A humid, subtropical monsoon climate prevails in Southwest China, with precipitation in the April to October rainy season accounting for approximately 70-80 % of the annual rainfall (Li et al., 2011, 2014). The average annual temperature is 18.0 °C in Wulong County (above Furong Cave) and 8.0 °C at Jinfo Mountain, Nanchuan district (above Yangkou Cave, based on meteorological data during 2012 to 2017), with the annual rainfall at these locations being 1200 mm and 1348 mm, respectively (Li et al., 2011, 2012). Average annual temperature in Guanling County (above Naduo Cave) is 14.2 °C and the annual rainfall is 1293 mm (Shen et al., 2016). For Panxian County and Liuzhi Special District in Liupanshui City, the annual temperature/rainfall are 11.9 °C/1234 mm and 14.2 °C/1476 mm, respectively (baike.baidu.com). Detailed geographical information, local vegetation, soil thickness of the study areas and host rock thickness above the corresponding caves are presented in Table 1.

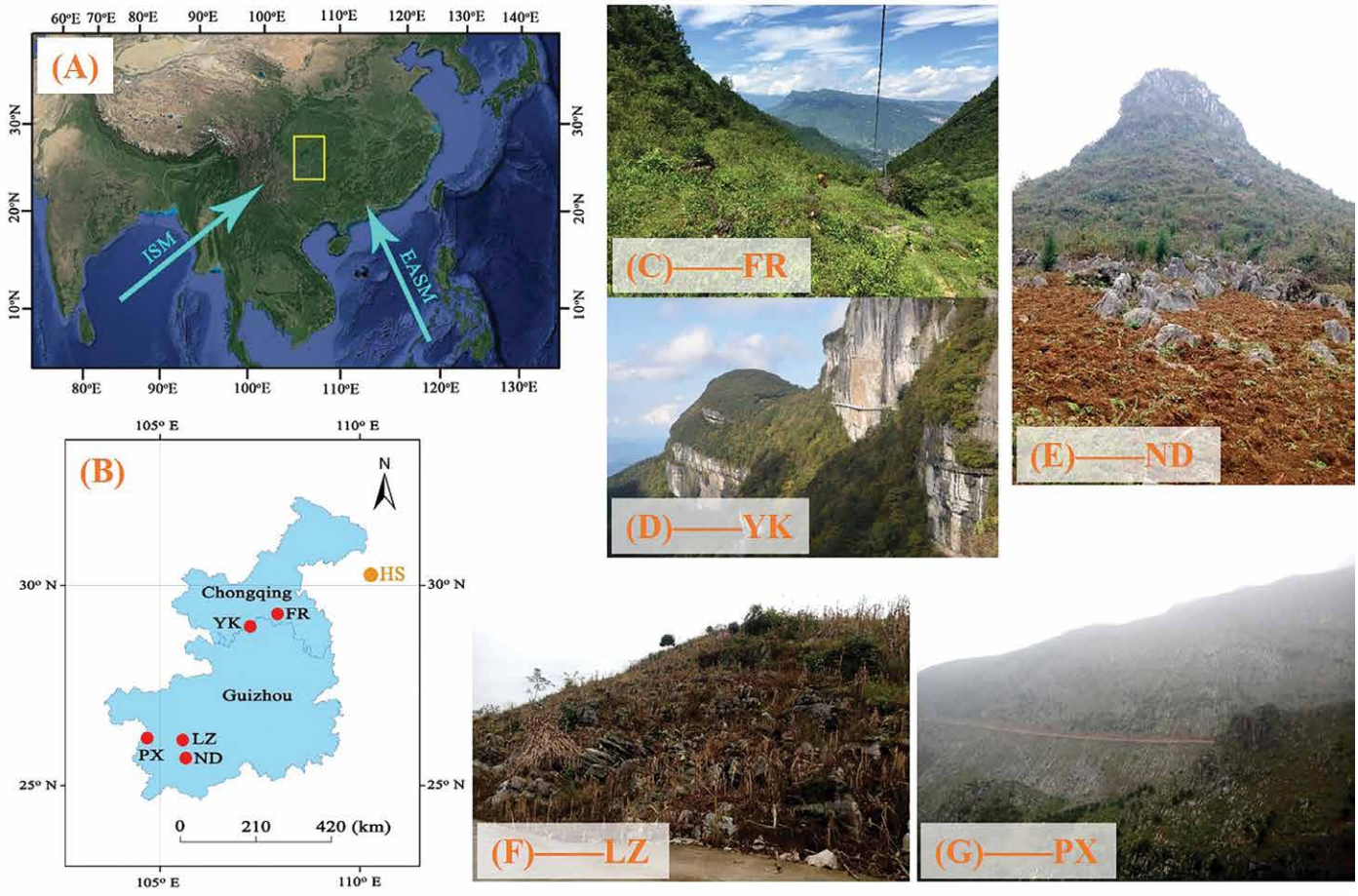


Figure 1. Location map showing the study area and specific sites. (A) The yellow rectangle indicates the study area and cyan arrows denote the directions of the East Asian summer monsoon (EASM) and ISM, which dominate the climate in Eastern and Southern China. (B) Enlarged map of study area. Red solid circles indicate the locations of Furong Cave (FR) (Li et al., 2011, 2012) and Yangkou Cave (YK) (Li et al., 2014a) in Chongqing City; Liuzhi Special District (LZ), Panxian County (PX) and Naduo Cave (ND) in Guizhou province. The brown, solid circle indicates the location of Heshang Cave (HS) (Hu et al., 2008a), which is referred to in this work. Subfigures (C), (D), (E), (F) and (G) show the local vegetation, landform and the situation of rocky desertification at these five study sites. The detailed geographical information of these areas has been described in Table 1.

**Table 1. Information about the sampling sites in this study.**

| Site | Latitude and Longitude | Elevation (m, a.s.l) | Mean annual air temperature, °C | Annual precipitation, mm | Province | Corresponding cave | Soil profiles | Thickness of soil profile, cm | Number of soil subsamples | Number of Plants samples | Vegetation | Rocky desertification degree (RDD)a |
|---|---|---|---|---|---|---|---|---|---|---|---|---|
| Wulong County (Li et al., 2012) | 29° 13′ N 107° 54′ E | 600–800 | 17.9 | 1078 | Chongqing | Furong Cave | SA | 55 | 11 | 27 | Arbors and shrubs | No |
| | | | | | | | SB | 25 | 5 | | | |
| | | | | | | | SC | 87 | 9 | | | |
| | | | | | | | SD | 64 | 13 | | | |
| | | | | | | | SE | 78 | 16 | | | |
| | | | | | | | SA | 55 | 11 | | | |
| Nanchuan district | 28° 50′ N 107° 20′ E | 2150 | 8.0 | 1348 | Chongqing | Yangkou Cave | JF-1 | 120 | 22 | 24 | Arbors and shrubs | No |
| | | | | | | | JF-2 | 125 | 23 | | | |
| | | | | | | | JF-3 | 75 | 14 | | | |
| Guanling County | 25° 48′ N 105° 35′ E | 1190 | 16.2 | 1268 | Guizhou | Naduo Cave | ND | 85 | 13 | 28 | Shrubs and grasses | Light |
| Liuzi Special District | 26° 11′ N 105° 33′ E | 1450 | 14.2 | 1476 | Guizhou | — | LZ-1 | 12 | 5 | 27 | Grasses and upland crops | Moderate |
| | | | | | | | LZ-2 | 32 | 8 | | | |
| | | | | | | | LZ-3 | 25 | 5 | | | |
| Panxian County | 26° 14′ N 104° 36′ E | 2200 | 11.9 | 1234 | Guizhou | — | PX-1 | 12 | 5 | 24 | Grasses | Severe |
| | | | | | | | PX-2 | 29 | 13 | | | |
| | | | | | | | PX-3 | 46 | 17 | | | |

a The classification of rocky desertification (RDD) level based on the rules of Xiong et al., (2002) and Jiang et al., (2014).

## Sampling and Analytical Methods

### Soil and Plant Samples

Based on the assessment of landform, plant families and vegetation intensity for each research site, one to three soil profiles were dug down to the bedrock, resulting in soil profile depths in the range of 12 cm to 125 cm (Table 1). Soil subsamples were collected at 3 cm to 10 cm intervals from the bottom to the top of each profile, with 125 soil subsamples collected in total (Table 1). The local vegetation was investigated by a 10 m × 10 m quadrat survey and 103 plant samples were collected in total, including the dominant trees, shrubs and grasses (Li et al., 2012, Table 1). For each site, detailed information about the soil profiles, local vegetation and RDD classification are presented in Table 1.

Before analysis for organic carbon $\delta^{13}C$, samples were prepared as follows: Sufficient HCl (5 % v/v) was used to release inorganic carbon from soil subsamples, which were subsequently dehydrated in air at 25 °C and ground into powder with a diameter of less than 50 μm. Plant samples were ultrasonically cleaned for 15 min in deionized water, dried at 50 °C for 48 h, and ground into powder with a diameter less than 150 μm. The detailed procedures are described by Li et al. (2012).

$\delta^{13}C$ analysis of organic matter contained in soil and plant subsamples from Chongqing City were conducted in the School of Geographical Sciences, Southwest University, China. The analytical instrument was the Thermo Delta V Plus, interfaced with a Flash 1200 Elemental Analyzer (EA)/Conflo-III. For the soil and plant samples from Guizhou Province, $\delta^{13}C$ analysis of organic carbon was performed in the Department of Geological Sciences, University of Texas at San Antonio, USA. The analytical instrument was the Thermo Finnigan Delta Plus XP interfaced with a Costech Elemental Analyzer. For both instruments, the analytical error for $\delta^{13}C$ was less than 0.1 ‰ (1σ). All the reported results of $\delta^{13}C$ were given with respect to V-PDB, using internal international standards: USGS-24 graphite ($\delta^{13}C$ = −15.99 ‰), IAEA 600 caffeine ($\delta^{13}C = -27.77$ ‰), ANU Sucrose ($\delta^{13}C = -10.45$ ‰) and Fisher caffeine ($\delta^{13}C = -35.4$ ‰).

### CO2 Concentrations of Cave and Soil Air

The $CO_2$ concentration ($pCO_2$) of cave air was monitored at drip-water sites (1# through 6#) in Yangkou Cave in Nanchuan district, Chongqing, with results shown in Fig. 2 (Wang et al., 2014). The instrument for determining $pCO_2$ was infrared device TESTO 535, with a measuring range of 0 ppmV to 9999 ppmV and resolution of 1 ppmV. Three soil profiles from above Yangkou Cave (JF-1, JF-2 and JF-3) were monitored for the $pCO_2$ of soil air at depths of 20 and 50 cm. The $pCO_2$ was determined using the Komyo Rikagaku kogyo K.K with AP-20 aspirating pump and 126SA test tube, which had a measuring range of 100 ppmV to 50,000 ppmV and resolution greater than 50 ppmV.

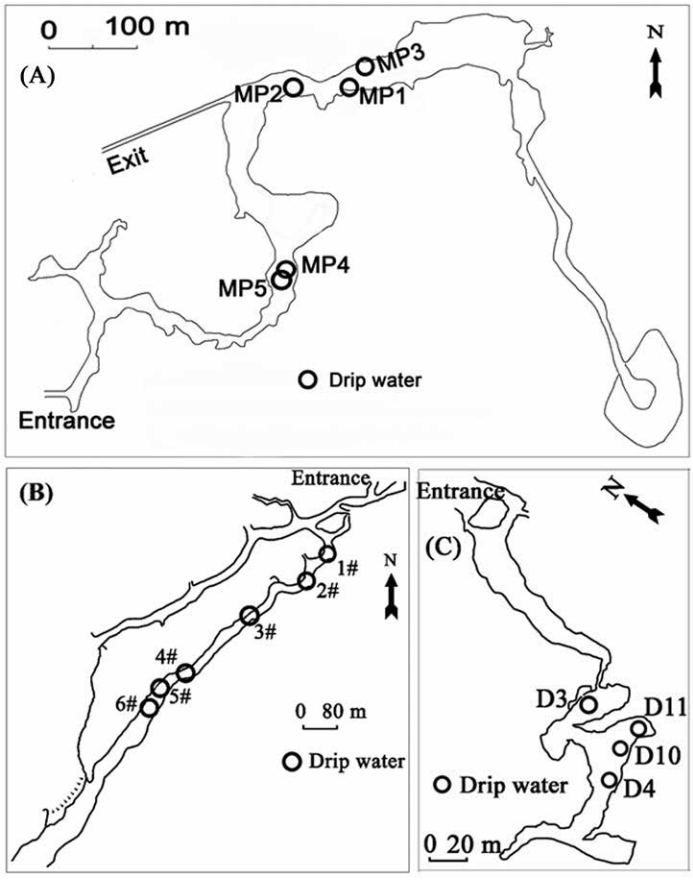


Figure 2. Sketch map of Furong Cave, Yangkou Cave and Naduo Cave and the distribution of the drip-water monitoring sites in the caves. These maps were modified from: (A) Furong Cave (Li et al., 2011); (B) Yangkou Cave (Wang et al., 2014); (C) Naduo Cave (Shen et al., 2016).

### Discharge Rate of Drip Water and Temperature of Cave Air

The discharge rate of the six drip water sites (#1 through #6) in Yangkou Cave was monitored. Depending on the water drip rate, the drip water was collected using 10 mL or 100 mL cylinders; the top of each cylinder had a funnel shape with 9 cm diameter. The volume of water collected in one minute was taken to reflect the discharge rate of the drip water (mL/min), and these *in situ* measurements were conducted monthly.

In the period from February 2012 to June 2014, the air temperature in the cave at about 5 m by site 3# was continuously recorded at 2 h intervals using the U12-011 temperature recorder (Onset company, USA), with an error of ±0.1 °C. Data were downloaded via HOBO software every month.

### DIC-δ13C in Cave Water

The DIC-$\delta^{13}C$ variation of drip water at six sites in Yangkou Cave (1# through 6#) was monitored. *In situ* sampling of drip water was conducted monthly in the period from July 2013 to October 2015. Collecting time for drip water varied in the range of 2 s to 50 min, based on the drip rate at the specific drip site and the month. To

**Table 2. $\delta^{13}C$ and $\delta^{18}O$ values of modern deposits in Yangkou Cave, Jinfo Mts. Chongqing.**

| Sample | $\delta^{13}C$, ‰ | $\delta^{18}O$, ‰ |
|---|---|---|
| modern-1 | −6.7 | −6.8 |
| modern-2 | −6.3 | −6.8 |
| modern-3 | −5.4 | −6.0 |
| modern-4 | −8.4 | −7.6 |
| modern-5 | −6.3 | −7.1 |
| modern-6 | −6.9 | −7.2 |
| modern-7 | −7.8 | −7.4 |
| Mean | −6.8 | −7.0 |
| Std. dev. | 1.0 | 0.5 |

water (20 mL) collected from each monitoring site, saturated aqueous $HgCl_2$ solution (0.2 mL) was added instantly to avoid potential isotopic fractionation by the effect of microorganisms. Water samples were sealed tightly and stored in the laboratory refrigerator at 5 °C. $CO_2$ for the measurement of the DIC was produced by the chemical reaction of phosphoric acid with the water sample. The DIC-$\delta^{13}C$ analyses of water samples were performed in the School of Geographical Sciences, Southwest University, China, using the Thermo Delta V Plus interfaced with the Thermo Gas Bench automated apparatus, with an analytical error of less than 0.2 ‰ (1σ).

For Furong Cave, located in Wulong County, Chongqing (Fig. 1), the DIC-$\delta^{13}C$ of cave water from the published data by Li et al. (2012) was used (Fig. 2A). For Naduo Cave, located in Guanling County, Guizhou Province (Fig. 1), the DIC-$\delta^{13}C$ of cave water from the published data by Shen et al. (2016) was used (Fig. 2C). There were no caves in the sites of Liuzi Special District and Panxian County, Guizhou province (Table 3).

### $\delta^{13}C$ of Cave "modern deposits" and Bedrock

Glass plates were placed under the six drip-water sites in Yangkou Cave to collect modern deposits, as was done in Furong Cave (Li et al., 2011, 2012). Only the deposits on artificially-placed substrates under drip water are accurate modern deposits. However, as there was no visible deposit on the plates through the monitoring period over several years, powders were scraped (less than 1 mm in depth) from the tops of stalagmites under drip sites without signs of

**Table 3. Changes of $\delta^{13}C$ in karst regions at different RDD, Southwest China.**

| Sites | Correspond cave | Thickness of Host rock, m | RDD | Average $\delta^{13}C$, ‰ | | | | | |
|---|---|---|---|---|---|---|---|---|---|
| | | | | Plants | Soils, SOM | Bedrock | DIC of drip water | Modern deposits | Note |
| Wulong County | Furong Cave | 300−500 | No | −31.8 ± 4.3a | −22.0 ± 1.4a | −1.1 ± 1.3 | −11.1 ± 0.6a | −10.5 ± 0.7a | Li et al. (2012)a |
| Nanchuan District | Yangkou Cave | 50−100 | No | −28.9 ± 1.8 | −24.6 ± 0.5 | 3.9 ± 0.5 | −3.0 ± 2.7 | −6.8 ± 1.0 | This study |
| Guanling County | Naduo Cave | 30−85 | Light | −26.2 ± 7.4 | −20.6 ± 0.9 | 1.5 ± 1.4 | −5.3 ± 2.2b | −6.5 ± 1.4 | Shen et al. (2016)b |
| Liuzhi Special District | NCCc | ··· | Moderate | −27.5 ± 5.5 | −19.9 ± 1.3 | −0.2 ± 0.0 (n=1) | ··· | ··· | This study |
| Panxian County | NCCc | ··· | Severe | −26.5 ± 4.2 | −21.2 ± 1.5 | 3.6 ± 0.9 | ··· | ··· | This study |

a Referred from Li et al. (2012)
b Referred from Shen et al. (2016)
c NCC = no corresponding cave identified but plants, soil, and bedrock samples were collected.

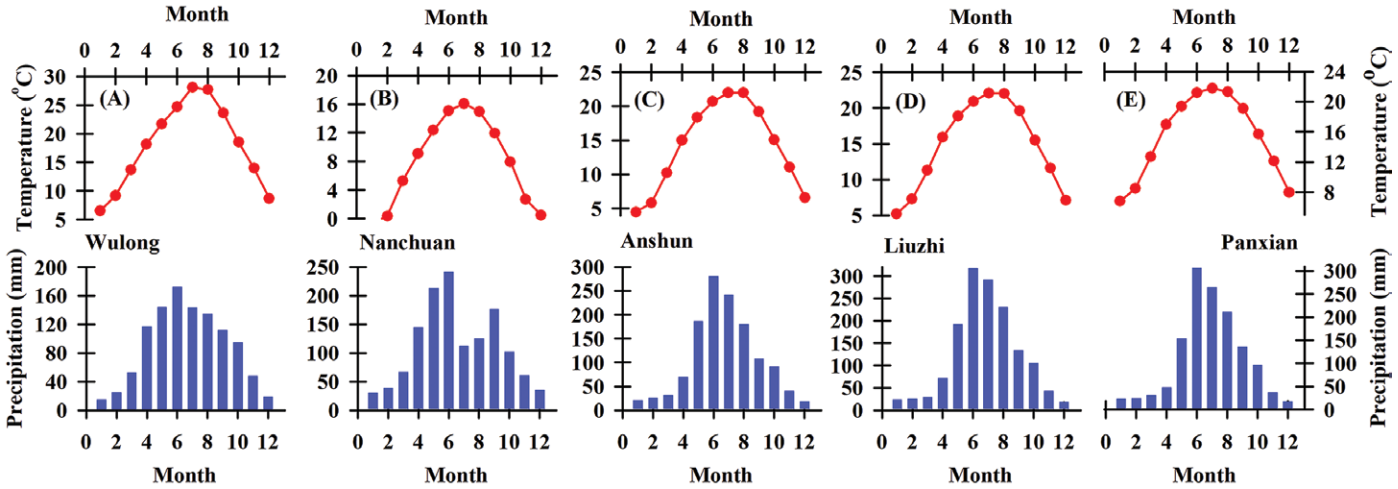


Figure 3. Monthly air temperature (°C) and precipitation (mm) for the study sites. (A) Wulong County (the location of Furong Cave), based on meteorological data from 2005 to 2016). (B) Jinfo Mt., Nanchuan District (the location of Yangkou Cave), based on meteorological data from 2012 to 2017. (C), (D), and (E) Anshun (the location of Naduo Cave), Liuzhi and Panxian, respectively, based on meteorological data from 1988 to 2010 from the meteorological data center of China Meteorological Administration (http://data.cma.cn/).

erosion or dissolution. Otherwise, visible, fresh deposits were collected from the surface of collapsed bedrock with drip water instead. These artificial, modern deposits would not influence the relationship between the DIC-$\delta^{13}C$ of drip water and RDD, because the relationship between drip water and deposit $\delta^{13}C$ is influenced by cave-related factors (e.g. ventilation, $CO_2$ degassing). Whereas the relationship between DIC-$\delta^{13}C$ of drip water and RDD is influenced by the factors in soil and the host rock. Analysis of $\delta^{13}C$ in the "modern deposits" samples was performed in the School of Geographical Sciences, Southwest University, China, using the Kiel IV carbonate device and Thermo Delta V Plus, with analytical error of below 0.1 ‰ (1σ). For each study area (Fig. 1), from above the cave and from near the drip-water sites in the cave, several blocks of bedrock were collected, broken by hammer and powder scraped from the fresh surface. The $\delta^{13}C$ content of this bedrock powder was determined using the same instruments as for the modern deposit samples.

## Results

### $\delta^{13}C$ of Plants

Twenty-four plant samples (classified as 24 species from 20 families) were collected from above Yangkou Cave (Jinfo Mt., Chongqing) (Supplementary Table 1). All of these plants were dominant species in the karst area of Southwest China. The $\delta^{13}C$ values of the plants ranged from −25.0 ‰ to −32.2 ‰, with the average being −28.9 ‰ ± 1.8 ‰. Twenty-eight plant samples were collected from above Naduo Cave (Guanling County, Guizhou province), with $\delta^{13}C$ values ranging from −11.2 ‰ to −32.2 ‰, with an average of −26.2 ‰ ± 7.4 ‰ (Supplementary Table 2). For the 27 plant samples collected in Liuzhi Special District, the $\delta^{13}C$ values ranged from −12.0 ‰ to −32.4 ‰ with an average of −27.5 ‰ ± 5.5 ‰ (Supplementary Table 3). Of the 24 plant samples collected in Panxian County, the $\delta^{13}C$ values ranged from −13.1 ‰ to −29.8 ‰, and the average was −26.5 ‰ ± 4.2 ‰ (Supplementary Table 4).

### $\delta^{13}C$ of soil organic matter (SOM)

Three soil profiles were dug above Yangkou Cave, named JF-1, JF-2 and JF-3 at depths of 120 cm, 125 cm, and 73 cm, respectively (Table 1). For each profile, the average $\delta^{13}C$ values of SOM ($\delta^{13}C_{SOM}$) were −24.4 ‰ ± 0.5 ‰, −24.9 ‰ ± 0.3 ‰, and −24.2 ‰ ± 0.4 ‰ (Fig. 4A; Supplementary Table 5), respectively. The soil profile above Naduo Cave was 85 cm in depth (Table 1), with an average $\delta^{13}C_{SOM}$ of −20.6 ‰ ± 0.9 ‰ (Fig. 4B; Supplementary Table 6). The average $\delta^{13}C_{SOM}$ values of three soil profiles in Liuzhi Special District were −19.8 ‰ ± 0.4 ‰, −19.2 ‰ ± 1.5 ‰ and −21.3 ‰ ± 0.4 ‰, and the average was −19.9 ‰ ± 1.3 ‰ for all soil samples (Fig. 4C; Supplementary Table 7). The average $\delta^{13}C_{SOM}$ values of three soil profiles in Panxian County were −23.0 ‰ ± 0.7 ‰, −21.5 ± 1.7 ‰, and −20.4 ‰ ± 0.9 ‰ and the average was −21.2 ‰ ± 1.5 ‰ for all of these soil samples (Fig. 4D; Supplementary Table 8).

### $CO_2$ Concentration of Soil Air above Yangkou Cave

The $CO_2$ concentration of soil air above Yangkou Cave changed seasonally in the range of 200-6800 ppmV, generally with higher values in summer and autumn months and lower values in winter and spring months (Fig. 5). Depth of soil profiles JF-1 and JF-2 were 120 cm and 125 cm, respectively, deeper than that of profile JF-3 at 70 cm (Table 1). Correspondingly, the average $CO_2$ concentration of soil air in JF-1 and JF-2 was 950 ppmV and 1300 ppmV, respectively, higher than in JF-3 at 800 ppmV.

### $CO_2$ Concentration of Cave Air in Yangkou Cave

For the six cave air $CO_2$-monitored sites (1#-6#, as drip water sites), the $CO_2$ concentration changed in the range of 308 ppmV to 554 ppmV, 326 ppmV to 654 ppmV, 316 ppmV to 800 ppmV, 333 ppmV to 622 ppmV, 346 ppmV to 781 ppmV and 312 ppmV to 544 ppmV, with an average of 388 ppmV, 412 ppmV, 446 ppmV, 402 ppmV, 445 ppmV,

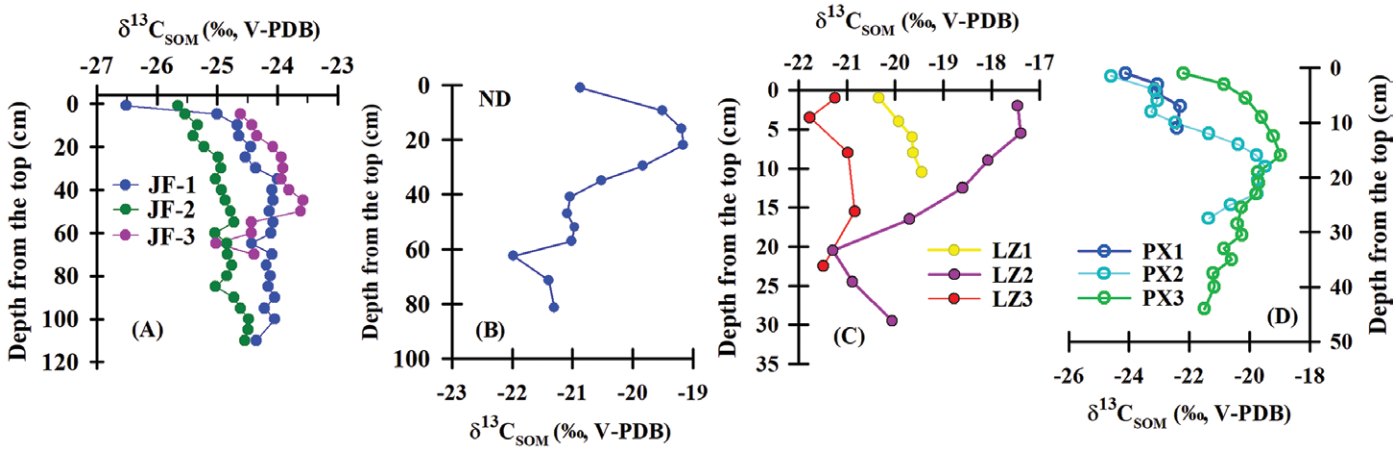


Figure 4. The $\delta^{13}C$SOM of soil profiles in: (A) Jinfo Mt., above Yangkou Cave, (B) Anshun country, the location of Naduo Cave, (C) Liuzhi Special District, and (D) Panxian County in Guizhou province.

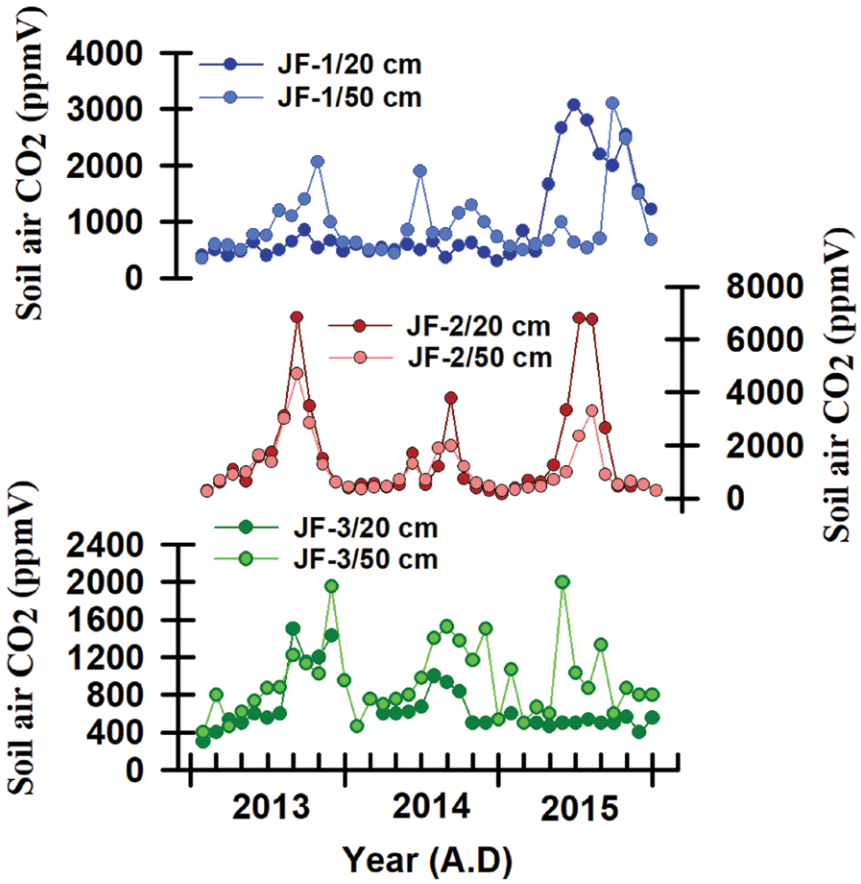


Figure 5. Monthly changes in soil air $CO_2$ concentration at different depths for the three soil profiles in Jinfo Mt., above Yangkou Cave.

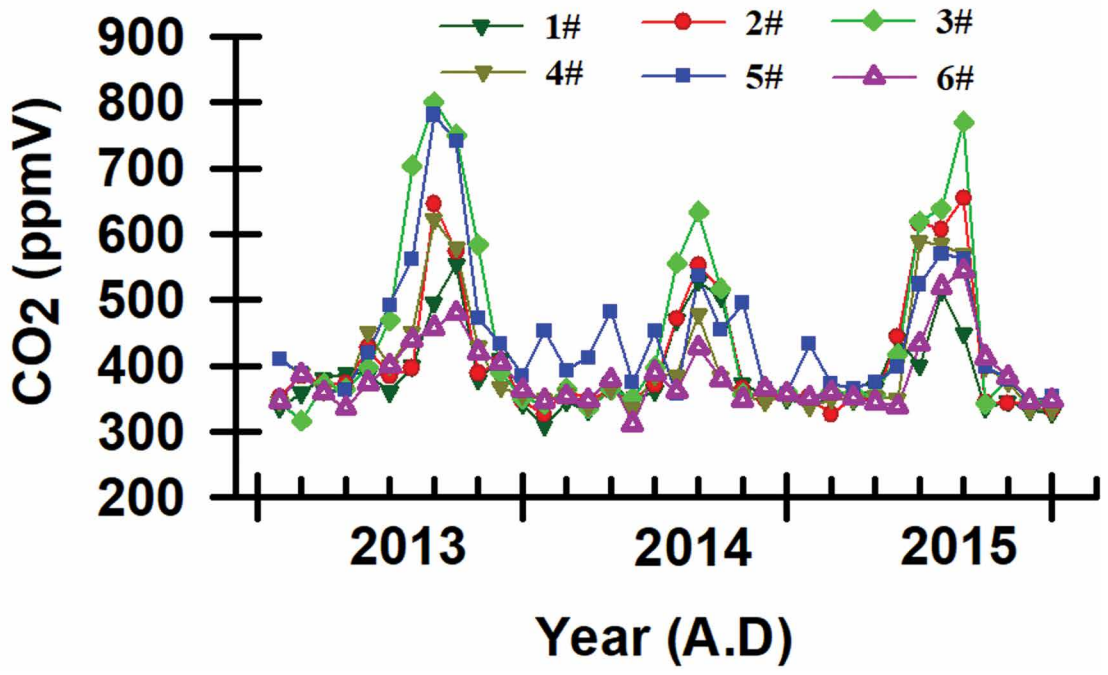


Figure 6. Monthly changes of cave air $CO_2$ concentration for the six drip-water monitoring sites in Yangkou Cave.

and 385 ppmV, respectively. There were obvious seasonal changes of cave air $CO_2$ concentration in Yangkou Cave, with higher values in the 600 ppmV to 800 ppmV range in summer months and lower values in the 300 ppmV to 400 ppmV range in winter and spring months (Fig. 6).

The relatively low soil $CO_2$ concentration above Yangkou Cave and air $CO_2$ concentration in Yangkou Cave were in contrast with the global average concentration of atmospheric $CO_2$ (~400 ppmV). This could possibly be attributed to analytical uncertainty (i.e., 50 ppmV for soil $CO_2$). Additionally, the high elevation above Yangkou Cave, which is more than 2,100 m a.s.l. and frequently frozen in winter months because of the low air temperature, resulted in significant depression of soil $CO_2$ production. Despite this phenomenon, the seasonal changes of $CO_2$ concentration in the soil and in the cave were clear.

**Discharge Rate Variation of Drip Water in Yangkou Cave**

The average discharge rate for the six drip-water sites (1#-6#) in Yangkou Cave were 178.6 mL/min, 141.5 mL/min, 15.4 mL/min, 2.8 mL/min, 6.9 mL/min, and 96.3 mL/min, respectively. Except at site 5#, there was no obvious seasonal change in the discharge rate (Fig. 7). For all the drip sites, the discharge changed in the range of 2.6 mL/min and 898.0 mL/min, 17.0 mL/min and 269.0 mL/min, 5.0 mL/min and 28.0 mL/min, 0.4 mL/min and 22.0 mL/min, 1.0 mL/min and 27.0 mL/min, and 3.9 mL/min, and 322.0 mL/min, respectively. This huge range in the change of discharge rate indicated that most of the drip waters monitored in Yangkou Cave were fissure water and responded relatively quickly to local precipitation, especially for drip sites 1#, 2# and 6# (Fig. 7).

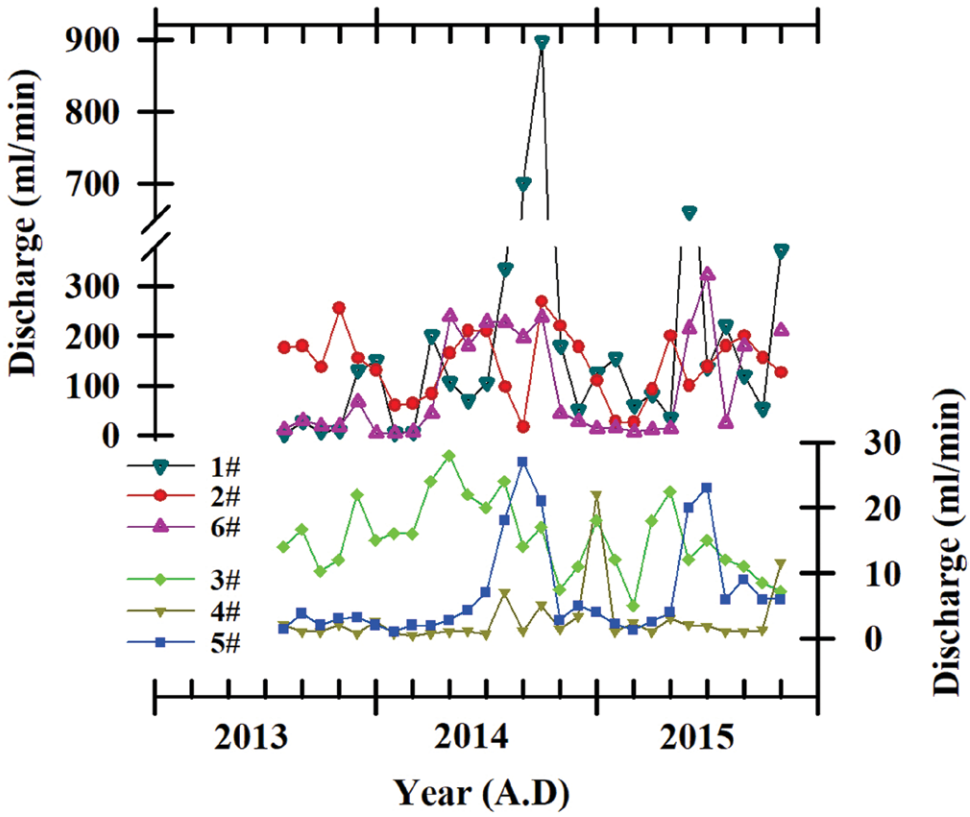


Figure 7. Monthly changes of the discharge rate for the six drip-water monitoring sites in Yangkou Cave.

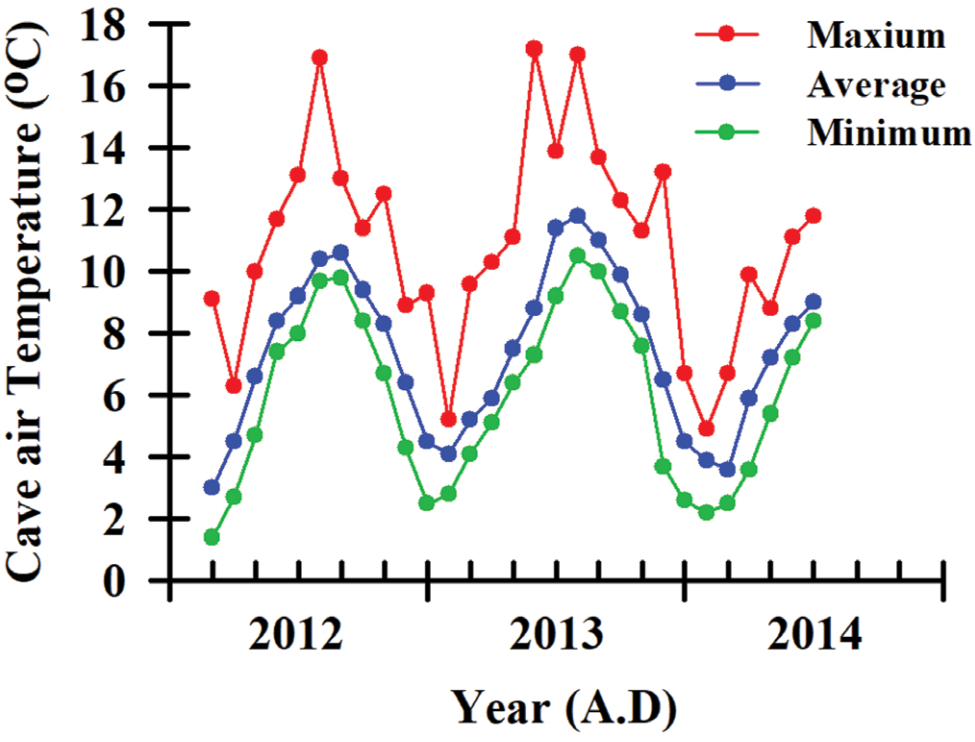


Figure 8. Monthly changes of cave air temperature, monitored at about five m from site 3# in Yangkou Cave (Fig. 2C).

### Air Temperature in Yangkou Cave

In the period from February 2012 to June 2014, the air temperature in Yangkou Cave fluctuated in the range of 1.4 °C – 17.2 °C (Fig. 8), with higher temperatures in the summer months and lower values in winter months, similar to the seasonal change of regional air temperature outside the cave (Fig. 3B). For the whole monitoring period, the monthly mean air temperature in Yangkou Cave was 7.4 °C, close to the value of 7.5 °C, reported by Li et al. (2014a).

### $\delta^{13}C$ of DIC, Bedrock and Modern Deposits

The average DIC-$\delta^{13}C$ values for the six drip-water sites (1#-6#) in Yangkou Cave were −5.1 ‰ ± 2.3 ‰, −3.0 ‰ ± 1.9 ‰, −5.8 ‰ ± 1.8 ‰, −0.3 ‰ ± 1.0 ‰, −0.5 ‰ ± 1.4 ‰, and −1.8 ‰ ± 1.8 ‰, respectively (Fig. 9). The great fluctuation in the ranges of drip water DIC-$\delta^{13}C$ (4 ‰ to 10 ‰) in Yangkou Cave (Fig. 9) should partially be attributed to the relatively open channel of the cave and the considerable cave ventilation effect (Fairchild et al., 2006), as partly indicated by the huge magnitude of air temperature fluctuations in Yangkou Cave (1.4 to 17.2 °C) (Fig. 8). Other potential reasons for the irregular change in drip water DIC-$\delta^{13}C$ in Yangkou Cave could include the seasonal change of soil $CO_2$ production and the equilibrium between soil water and soil $CO_2$ (Baker et al., 1997). Both are closely related to changeable precipitation and soil hydrological conditions.

Sixteen subsamples of bedrock were collected in total, 11 in Yangkou Cave and five out of the cave, with the average $\delta^{13}C$ values being 4.1‰ and 3.5‰, respectively. For all the bedrock subsamples, the average $\delta^{13}C$ was 3.9 ‰ ± 0.5 ‰ (Supplementary Table 9). The $\delta^{13}C$ values of seven “modern deposit” subsamples collected in Yangkou Cave, ranged from −5.4 ‰ to −8.4 ‰, with an average value of −6.8 ‰ ± 1.0 ‰ (Table 3).

## Discussion

### Differences in $\delta^{13}C$ of Regional Plants

For all sites mentioned in this study, Wulong, Nanchuan, Guanling, Liuzhi and Panxian, the average $\delta^{13}C$ of local plants was −31.8 ‰ ± 4.3 ‰ (Li et al., 2012), −28.9 ‰ ± 1.8 ‰, −26.2 ‰ ± 7.4 ‰, −27.5 ‰ ± 5.5 ‰, and −26.5 ‰ ± 4.2 ‰, respectively (Table 3).

The average $\delta^{13}C$ value of the plants above Naduo Cave (in Guanling County), −26.2 ‰, was close to that of plants above Yangkou Cave (−28.9 ‰). The relatively large standard deviation (7.4 ‰ for Naduo Cave vs. 1.8 ‰ for Yangkou Cave), was attributed to four species above Naduo Cave: *Pogonatherum paniceum, Imperata cylindrica, Sorghum bicolor* and *Capillipedium assimile*, with $\delta^{13}C$ values higher than -13‰ (Supplementary Table 2). *Sorghum bicolor* is a crop introduced from Northern China. *Pogonatherum paniceum, Imperata cylindrica* and *Capillipedium assimile* are local grasses; these account for an especially small proportion (< 3%) of local biomass, based on the field investigation. Exclusion of these four species resulted in an average $\delta^{13}C$ for plants above Naduo Cave of −29.9 ‰ ± 1.6 ‰.

For Liuzhi Special District, the species of *Arthraxon hispidus, Imperata cylindrica* and *Zea mays*, which are Gramineae plants, had higher $\delta^{13}C$ values of around −12 ‰ to −13 ‰ (Supplementary Table 3). Exclusion of these three species resulted in an average $\delta^{13}C$ for the other 24 plant samples of −29.4 ‰ ± 1.6 ‰. *Zea mays* is a crop and *Arthraxon hispidus* and *Imperata cylindrical* are grasses. For most local plants in Liuzhi, the $\delta^{13}C$ value is around −29 ‰.

For Panxian County, the Gramineae grass species *Imperata cylindrica* and *Arthraxon hispidus*, with higher $\delta^{13}C$ values of −13.4 ‰ and −13.1 ‰, respectively, accounted for a relatively small proportion of local, total biomass. Exclusion of these two species resulted in an average $\delta^{13}C$ for the other 22 plant samples of −27.7 ‰ ± 1.1 ‰, with all $\delta^{13}C$ values below −25 ‰ (Supplementary Table 4).

In summary, for most of the present vegetation in these four study sites, the average $\delta^{13}C$ of plants consistently matched the $\delta^{13}C$ distribution of modern C3 photosynthesis vegetation (−20 ‰ to −35 ‰) (Dienes, 1980, p. 320–406; McDermott, 2004). In other words, at present, severe rocky desertification in Panxian County has not changed the dominance of C3 vegetation. This observation is essentially different to previous opinion, which argued that the evolution of rocky desertification in southwest China will change C3/C4 vegetation and finally result in changes to speleothem $\delta^{13}C$ (Zhang et al., 2006).

### Variation of $\delta^{13}C_{SOM}$ in Soils

For soil profiles JF-1 and JF-2 above Yangkou Cave, the $\delta^{13}C_{SOM}$ values were steady, with variation of about 0.5 ‰ below a depth of about 40 cm. Additionally, from the top to the bottom of the soil profiles, the $\delta^{13}C_{SOM}$ values tended to increase (Fig. 4A), which was consistent with the trend in $\delta^{13}C_{SOM}$ values above Furong Cave (Li et al., 2012) arising from the fractionation of stable carbon isotopes, due to plant decomposition (Trumbore, 2000). The lowest $\delta^{13}C_{SOM}$ values at the top of the soil profiles, as low as −28.9 ‰ ± 1.8 ‰ (Table 3), were attributed to the relatively large amount of undecomposed plants at the top of the soil profile. However, profile JF-3 showed a reverse of this trend from a depth of 45 cm, with a higher $\delta^{13}C_{SOM}$ value by about 1.5 ‰ at the depth of 65 cm (Fig. 4A). This abnormal phenomenon was attributed to the uneven distribution of plant roots and residues, or some disturbance of the soil layers.

Above Naduo Cave, the $\delta^{13}C_{SOM}$ values increased with growing depth for the top 22 cm section of the soil profile, but became relatively lower at depths of 22 cm to 41 cm (Fig. 4B). At deeper than 41 cm, the $\delta^{13}C_{SOM}$ values were around −21 ‰, except for an excursion of ~1 ‰ at a depth of 63 cm (Fig. 4B). This distribution of $\delta^{13}C_{SOM}$ values along the soil profile was similar to the characteristics of soil profile JF-3 above Yangkou Cave (Fig. 4A), as explained above.

From the top to bottom, the $\delta^{13}C_{SOM}$ of profiles LZ1 and LZ3 remained steady around their average values, with a variation amplitude of about 1 ‰ (Fig. 4C). The $\delta^{13}C_{SOM}$ of profile LZ2 decreased by 3.8 ‰ from the top to a depth of 20.5 cm, and reversed to increase by 1‰ at the bottom. Maize (*Zea mays*), which is a C4 plant ($\delta^{13}C$ = −12.3 ‰) and a typical crop in southwest China, can grow even in karst regions with severe, rocky desertification because of its drought tolerance. Accordingly, one additional soil sample was collected from maize land in Liuzhi Special District, and the $\delta^{13}C_{SOM}$ test result was −20.9 ‰. Therefore, the development of human agricultural activities and the planting of maize in karst regions had no significant effect on the enrichment of the value of $\delta^{13}C_{SOM}$.

Generally, the $\delta^{13}C_{SOM}$ values of PX1 increased from the top to the bottom of the soil profile. Both the PX2 and PX3 profiles showed an increase in $\delta^{13}C_{SOM}$ values from the top to a depth of 18 cm and 16 cm, respectively, and then decreased by 1.9 ‰ and 2.5 ‰, respectively, to the bottom (Fig. 4D). This was similar to the $\delta^{13}C_{SOM}$ changes in the soil profiles above Naduo Cave (Fig. 4A) and for LZ2 in Liuzhi Special District (Fig. 4C), which was attributed to the rapid water loss and soil erosion in the karst rocky desertification area (Jiang et al., 2014). This led to the relatively fast migration of surface SOM and relatively lower $\delta^{13}C_{SOM}$ values into the deep soil layers.

### Relatively Higher DIC-$\delta^{13}C$ in Yangkou Cave

Because of the large cave opening and over 10 m high/wide tunnel of Yangkou Cave, the monthly average air temperature in the deepest chamber of this cave ranged from 1.4 to 17.2 °C during the period of February 2012 to June 2014 (Fig. 8). Seasonal temperature changes influence the cave ventilation, accounting for the disequilibrium fraction-

ation of stable, carbon isotopes with the degassing of $CO_2$ (Spötl et al., 2005). The relatively higher DIC-$\delta^{13}C$ of drip water in Yangkou Cave could be explained by incomplete isotopic equilibrium between soil $CO_2$ and percolating $H_2O$, due to relatively short water-soil residence times (Baker et al., 1997), as indicated by the relatively fast discharge of drip waters (except at site #4) (Fig. 7). Another possible reason is the relatively lower biological activity in the overlying soils because of the higher elevation (2,150 m a.s.l) and lower temperature, which result in a lower soil $CO_2$ concentration (Fig. 5). For example, the maximum soil $CO_2$ concentrations above Yangkou Cave were about 3200 ppmV, 7000 ppmV, and 2000 ppmV for JF-1, JF-2, and JF-3 soil profiles, respectively (Fig. 5). In contrast, the maximum soil $CO_2$ concentration above Furong Cave was more than 13,000 ppmV in the months of July and August. The higher DIC-$\delta^{13}C$ values and lower discharge rate of site #4 may be attributed to the fractionation of stable isotopes by prior calcite precipitation (PCP) due to the long residence of groundwater (Fairchild et al., 2006).

**Systematic Variation of $\delta^{13}C$ for Yangkou Cave**

The average $\delta^{13}C_{SOM}$ value above Yangkou Cave was −24.6 ‰ ± 0.5 ‰, about 4.4 ‰ higher, compared to the average $\delta^{13}C$ value of the plants above Yangkou Cave, which was −28.9 ‰ ± 1.8 ‰ (Table 3). Above Furong Cave, the average $\delta^{13}C_{SOM}$ value was −21.5 ‰, which was 11.6 ‰ higher than the $\delta^{13}C$ value of local plants (−31.8 ‰) (Li et al., 2012). The relatively small difference in soil and plant $\delta^{13}C$ above Yangkou Cave was attributed to the higher altitude (2,150 m a.s.l) (Table 1), lower temperature, greater precipitation and higher regional humidity, which result in relatively lower decomposition of SOM and preserve the negative $\delta^{13}C$ information of local plants.

The average $\delta^{13}C$ value of the "modern deposits" in Yangkou Cave was −6.8 ‰ ± 1.0 ‰ (Table 3), lower than the average DIC-$\delta^{13}C$ value of drip water, which was 3.0 ‰ ± 2.7 ‰ (Table 3). It must be reiterated that the scraped modern deposits of Yangkou Cave in this study were temporal mixing deposits (months or years), not the deposits strictly precipitated from the contemporaneous drip water, as described in section 3.5. Considering the DIC-$\delta^{13}C$ of drip water changes greatly (Fig. 9), if most of the collected "modern deposits" precipitated from the water had relatively lower DIC-$\delta^{13}C$ values, this could reasonably explain why the $\delta^{13}C$ values of the "modern deposits" were seemingly even lower than those of DIC in drip water. Additionally, the average value of −6.8 ‰ for the modern deposits in Yangkou Cave was within the range of −14 ‰ to −6 ‰ for speleothems with overlying C3 vegetation (McDermott, 2004). The relatively higher carbon isotope signature should be attributed to multiple factors, such as the rapid filtering of percolating $H_2O$ (Fig. 7), resulting in non-equilibrium of isotopes between soil water and soil $CO_2$ (Baker et al., 1997), and rapid degassing of $CO_2$ for drip waters because of the strong ventilation (Fig. 8) (McDermott, 2004). Nevertheless, even considering the overlying dominance of C3 plants, the $\delta^{13}C$ values of the modern deposits in Yangkou Cave were relatively high.

**Systematic Variation of $\delta^{13}C$ for Naduo Cave**

The DIC-$\delta^{13}C$ of drip waters for four drip sites in Naduo Cave ranged from 0.6 ‰ to −10.4 ‰ with an average of −5.3 ‰ ± 2.2 ‰, based on data published by Shen et al. (2016). This massive DIC-$\delta^{13}C$ range in the Naduo Cave drip waters was attributed to seasonal changes in soil $CO_2$, which, presented by the $CO_2$ in cave air, ranged from 300 ppmV to 1700 ppmV. It was also ascribed to the difference in length and pathways of groundwater for each drip site (Shen et al., 2016). The $\delta^{13}C$ of modern deposits in Naduo Cave changed in the range of −4.3 ‰ to −8.6 ‰ and the average being −6.5 ‰ ± 1.4 ‰ (Table 3). So, for Naduo Cave, the $\delta^{13}C$ is increased by 5.6 ‰ and 15.3 ‰, from local plants to SOM and from SOM to drip water DIC, respectively. The average $\delta^{13}C$ of modern deposits in Naduo Cave were relatively lower compared with the average of DIC in drip waters, like those in Yangkou Cave. Considering the $\delta^{13}C$ of bedrock above Naduo Cave was 1.5 ‰, this phenomenon was attributed to the asynchrony of the modern deposits and drip water. In other words, most "modern deposits" precipitated from drip water with relatively lower DIC-$\delta^{13}C$ value, similar to as discussed with systematic variation in Yangkou Cave.

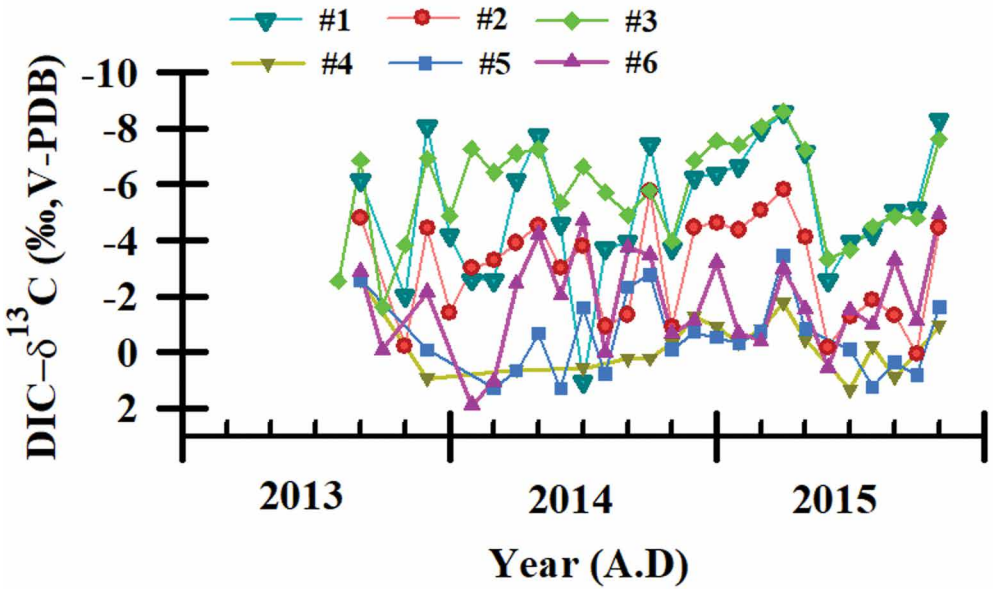


Figure 9. The drip-water DIC-$\delta^{13}C$ values in Yangkou Cave for the six drip-water sites (1# to 6#).

**Changes of $\delta^{13}C$ in Karst Regions with Different RDD**

There were some differences in the $\delta^{13}C$ of plants in the five karst areas discussed in this study. The lowest average plant $\delta^{13}C$ (−31.8 ‰) presented above Furong Cave, and the highest value (−26.2 ‰) was above Naduo Cave (Table 3). For rocky desertification areas, the relatively high plant $\delta^{13}C$ is mainly because of the Gramineae plants *Imperata cylindrica*, *Capillipedium assimile*, *Arthraxon hispidus* and *Arthraxon hispidus* (Supplementary Tables 2, 3 and 4), which had $\delta^{13}C$ values as high as −11 ‰ to −13 ‰. Excepting these Gramineae plants, the average plant $\delta^{13}C$ values for the rocky desertification areas were −26.3 ‰, −29.4 ‰, and −27.7 ‰ for Guanling County, Liuzhi Special District and Panxian County, respectively. Considering the relatively small proportion (< 3 %) of biomass formed by the Gramineae plants, their contribution to the average $\delta^{13}C$ of local plants will be negligible.

In summary, based on the findings of this study, at present the dominant plants in the karst regions of Southwest China belong to C3 vegetation, characterized by negative plant $\delta^{13}C$ values of below −26 ‰ (Table 3). The regional deviation of plant $\delta^{13}C$ values was attributed to the variation of species and local environment (O'Leary, 1988).

For these five karst regions (Fig. 1), the average $\delta^{13}C_{SOM}$ value was around −19.9 ‰ to −21.5 ‰, except for above Yangkou Cave, where the average $\delta^{13}C_{SOM}$ value was −24.6 ‰ (Table 3). This relatively lower $\delta^{13}C_{SOM}$ value was attributed to the higher altitude and lower temperature, which can depress the decomposition of organic matter. It is significant that, in spite of the $\delta^{13}C$ differences of local plants, or the situation of RDD, the $\delta^{13}C_{SOM}$ values were consistent across the four regions.

The most significant changes were in the DIC-$\delta^{13}C$ of drip waters and the $\delta^{13}C$ of modern deposits in caves (Table 3). The DIC-$\delta^{13}C$ of drip waters is influenced by multiple factors, including the type of local vegetation (C3 or C4) (Cerling, 1984; McDermott, 2004), biomass, root respiration and microbial activity (Luo et al., 2007), local precipitation and humidity, residence time of soil water and its influence on dissolution of soil $CO_2$ (Baker et al., 1997), prior calcite precipitation (PCP) in the epikarst zone (Fairchild et al., 2006), dissolution of bedrock (Genty et al., 2001; Fairchild et al., 2006), and the openness of the karst system (Hendy, 1971; Salomons and Mook, 1986, p. 241–269). For all the sites mentioned in this study, the average $\delta^{13}C$ of bedrock ranged from −1.1 ‰ to 3.9 ‰ (Table 3). The average DIC-$\delta^{13}C$ of drip waters ranged from −11.1 ‰ to −3.0 ‰ and the average $\delta^{13}C$ of cave "modern deposits" ranged from −10.5 ‰ to −6.5 ‰ (Table 3).

There appeared to be a positive correlation between the $\delta^{13}C$ of DIC "modern deposits" and the $\delta^{13}C$ of bedrock. The DIC-$\delta^{13}C$ of drip water and the $\delta^{13}C$ of "modern deposits" changed with amplitudes of 11 ‰ and 3 ‰, respectively, in Yangkou Cave, and 11 ‰ and 4 ‰, respectively, in Naduo Cave (Fig. 9; Table 2; and Shen et al., 2016). Dissolution of bedrock is a minor contributor to the relatively small proportion of carbon in DIC (Genty, et al., 2001), and most of the carbon originates from organic sources. Furthermore, the dissolution of bedrock is also partly affected by the degree of exposure of the karst system (Hendy, 1971; Salomons and Mook, 1986, p. 241–269; Fairchild et al., 2006). For Furong, Yangkou and Naduo Caves, the different $\delta^{13}C$ values of DIC and "modern deposits" were attributed to the different RDD of these sites (Table 1), but not because of the differences in species of local plants, nor the $\delta^{13}C$ of local plants and SOM (Table 3). The RDD above Yangkou Cave and Naduo Cave are classified as No Rocky Desertification and Light Rocky Desertification, respectively (Table 1) (Xiong et al., 2002, Jiang et al., 2014). In general, the higher RDD means more rock exposure, and less soil thickness and vegetation coverage (Xiong et al., 2002, Jiang et al., 2014), resulting in less organic matter (with negative $\delta^{13}C$ values of C3 vegetation) supplied to soils. More importantly, higher RDD can lead to less bioactivity in soils, more soil erosion, and rapid infiltration of precipitation, so that an equilibrium between soil water and soil $CO_2$ cannot be reached (Baker et al., 1997). The above-mentioned processes lead to the relatively high $\delta^{13}C$ of drip water DIC and corresponding speleothems.

**Implications for Paleoenvironment Reconstruction**

Based on Cerling's (1984) findings, speleothem $\delta^{13}C$ is also interpreted to reflect the evolution of local vegetation (Coplen et al., 1994; Bar-Matthews et al., 1997; Dorale et al., 1998; Lee-Thorp et al., 2001; Genty et al., 2003; Holmgren et al., 2003; Cosford et al., 2009; Zhao et al., 2016). Undoubtedly, evolution of vegetation (C3 and C4 or the proportion of C3/C4) will change the biomass and the $\delta^{13}C$ of SOM and soil $CO_2$. Evolution of local vegetation is dominated by changes in temperature and precipitation (or humidity), which can directly connect the $\delta^{13}C$ of SOM and soil $CO_2$ with climate change. Meanwhile, there are complex processes linking soil $CO_2$ to speleothems, including the dissolution of soil $CO_2$ in vadose water (Baker et al., 1997; Bar-Matthews et al., 2000), dissolution of bedrock (Genty et al., 2001), migration of water in the vadose zone (Dreybrodt and Schloz, 2011), prior calcite precipitation (PCP) (Fairchild et al., 2006), ventilation in caves and degassing of $CO_2$ from drip water in relation to the $CO_2$ concentration of the cave atmosphere (Spötl, et al., 2005; Li et al., 2012). These processes may change the $\delta^{13}C$ values significantly and even mask the signals of local vegetation and climate. Despite this, some processes are essentially influenced by climate change. For example, higher temperatures and/or decreased precipitation, resulting from climate change, will strengthen evaporation in fractures, bringing about PCP and ultimately increased $\delta^{13}C$ in drip water and corresponding speleothems. In this situation, the $\delta^{13}C$ of speleothems can display a positive correlation with local temperature (Martin-Chivelet et al., 2011).

Variations in stalagmite $\delta^{13}C$ have been used to reconstruct the evolution of local vegetation and to assess the history of rocky desertification in the karst regions of Southwest and Central China. Lower $\delta^{13}C$ values have been interpreted to mean more extensive vegetation under wetter climate, and higher $\delta^{13}C$ values to indicate dry climate or the strengthening of rocky desertification (Cosford et al., 2009; Kuo et al., 2011). Mass works have demonstrated that the change in stalagmite $\delta^{13}C$ should not be explained simply by changes in vegetation because multiple factors can influence the change of stalagmite $\delta^{13}C$ (McDermott, 2004; Fairchild et al., 2006; Huang et al., 2016).

This investigation showed that for modern conditions, rocky desertification does not change the predominance of C3 vegetation, and there is no significant correlation between the $\delta^{13}C_{SOM}$ and RDD (Table 7). Consider that the annual temperature decreased by ~3 °C in Central China during the Oldest and Younger Dryas and Last Glacial period (Zhu et al., 2008; Caley et al., 2014), and the $\delta^{13}C$ of organic matter and pollen in peat from Southern China showed the dominance of C3 vegetation, even during cold epochs such as the Younger Dryas and Heinrich event 1 (Zhou et al., 2004; Zhong et al., 2010), the prominent enrichment trend of stalagmite $\delta^{13}C$ since the Last Glacial period in Central and Southern China, cannot be attributed to the transition of vegetation types from C3 to C4. Rocky desertification cannot necessarily change the dominance of C3 vegetation in Southern/Southwestern China, but it can change the biomass and microbial processes in soils, which then influence the $\delta^{13}C$ of speleothems (Luo et al., 2007).

Essentially, higher RDD may lead to more exposure of rock (Xiong et al., 2002; Jiang et al., 2014), less vegetation density and biomass, decreased soil thickness (Fig. 1), faster water infiltration and more soil erosion (Jiang et al., 2014). These processes reduce isotopic equilibrium between soil $CO_2$ and water (Baker et al., 1997; Bar-Matthews et al., 2000), increase the relative proportion of atmospheric $CO_2$ in soils (Genty et al., 2001), strengthen PCP in fractures (Fairchild et al., 2006), and finally result in isotopically higher $\delta^{13}C$ in DIC and speleothems. So, it is plausible that variations of stalagmite $\delta^{13}C$ in the subtropical karst regions of China reflect the soil humidity balance associated with regional hydrological circulation (Li, 2007; Liu et al., 2016), which may originate from climate change or the evolution of rocky desertification.

It is difficult to distinguish between the contribution of human activities and natural processes to rocky desertification, especially in the past 2000 years with mixed effects of population growth, irrigation, the development of farming and industrialization, and climate changes on decadal-centennial timescales (Jiang et al., 2014). For the period before the 2 ka BP, when populations were small, the change in rocky desertification and the change of speleothem $\delta^{13}C$ should mainly be attributed to natural processes, such as the change of local hydrological circulation, caused by climate changes. Based on this assumption, see the case study below.

Speleothem $\delta^{13}C$ and $\delta^{18}O$ records from Asian monsoon regions present similar patterns on orbital timescales (Jo et al., 2014), and the strong co-variation of $\delta^{13}C$ and $\delta^{18}O$ records on centennial timescales have been attributed to the soil humidity balance (Liu et al., 2016). This indicates a correlation between local vegetation, soil $CO_2$ and monsoon circulation (Huang et al., 2016). Strong Asian summer monsoon (ASM) is associated with higher temperature in the northern hemisphere (Cheng et al., 2016); the increased precipitation and higher temperatures in monsoon regimes benefits the prevailing of C3 vegetation. This mechanism is a logical interpretation for the similar changes of speleothem $\delta^{13}C$ and $\delta^{18}O$ records. Southwestern China is located on the main moisture transportation pathway and is mainly influenced by the relatively simple Indian summer monsoon (ISM) (Ding and Sun, 2002; Ding and Chan, 2005). The lower speleothem $\delta^{18}O$ in Southwestern China mainly indicates strengthened summer monsoon and more local precipitation (Li et al., 2007).

Based on the climate background mentioned above, a simplified concept model to assess the relationship between speleothem $\delta^{18}O$, $\delta^{13}C$, local vegetation, and precipitation for Southwest China is proposed (Fig. 10). In this model, scenario I, strong summer monsoon generates high precipitation and, combined with warmer temperatures, is conducive to the prevalence of C3 vegetation, higher vegetation density and higher soil $CO_2$ concentration. Increased precipitation raises the soil humidity, provides conditions for isotopic equilibrium of carbon between soil $CO_2$ and water, and, finally, results in lower speleothem $\delta^{18}O$ and $\delta^{13}C$ values. In scenario II, strong summer monsoon leads to heavy precipitation, rapid infiltration of soil water and non-isotopic-equilibrium between soil $CO_2$ and water (Baker et al., 1997; McDermott, 2004), or enhanced weathering of host rock because of the large water flux, and, finally, results in higher speleothem $\delta^{13}C$ and lower $\delta^{18}O$ values (Bar-Matthews et al., 2000). In scenario III, relatively weak summer monsoon generates lower precipitation, resulting in lower humidity, less vegetation density (still dominated by C3 plants in Southwest China), lower soil $CO_2$ concentration and longer residence of water in soil and fractures. In addition, because of the decline of surface water supply, it is possible that the fractures and cracks in the epikarst zone contain less water or are even empty, leading to degassing of $CO_2$ and PCP, which results in higher speleothem $\delta^{13}C$ values (Fairchild et al., 2006). In scenario IV, lower temperature and precipitation depresses the growth of vegetation and soil microbial activity, thereby weakening the process of pedogenesis. The main topography in Southwest China is mountainous terrain, with limited or, even, no C-horizon (weathering crust) in karst soil profiles (Jiang et al., 2014). This ultimately leads to the reduction of adhesion and affinity between the soil and bedrock. Consequently, the soil is easily eroded by heavy rainstorms and

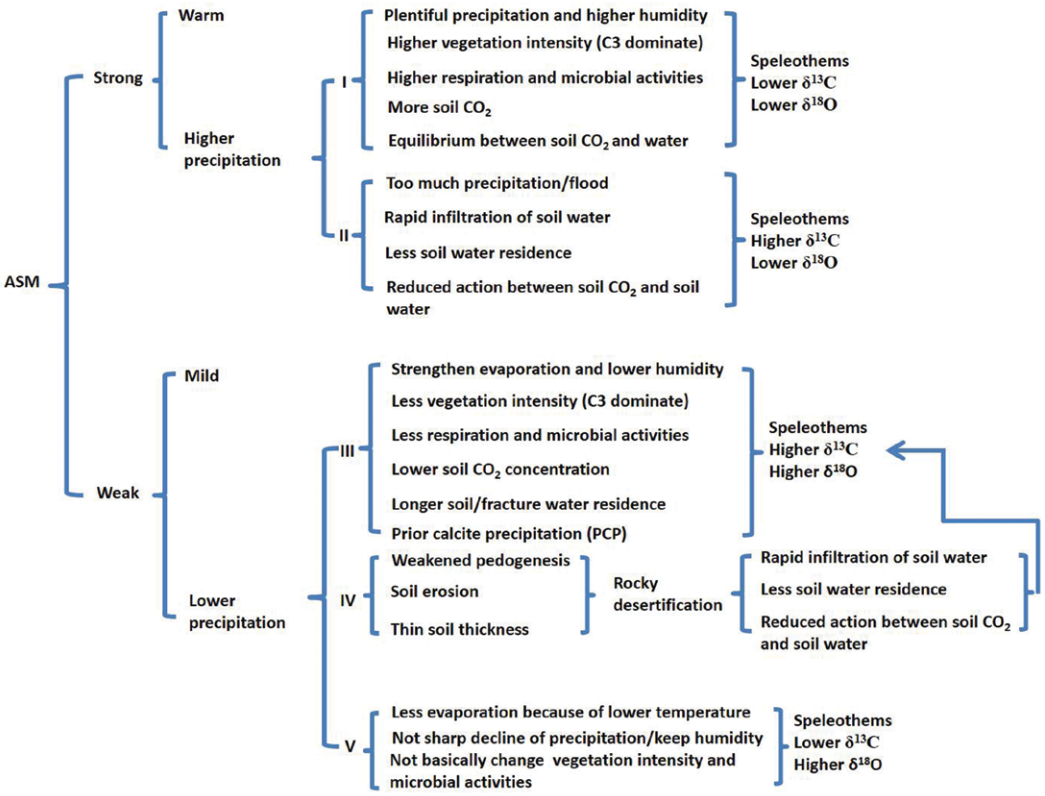


Figure 10. Concept model relating to the evolution of ASM and regional vegetation, hydrological conditions and the possible combinations of speleothem $\delta^{13}C$ and $\delta^{18}O$ in subtropical Southern and Central China.

overland flows, exposing the bedrock to rocky desertification (Yuan, 1993; Zhang et al., 2006; Jiang et al., 2014). Rocky desertification results in decreased soil thickness, rapid infiltration of surface and soil water, and non-isotopic-equilibrium between soil $CO_2$ and water (Baker et al., 1997; McDermott, 2004), and eventually leads to higher speleothem $\delta^{13}C$ (Fig. 10). Scenario V is also a possibility, with weak summer monsoon accompanied by mild temperatures and low precipitation (Zhu et al., 2008; Caley et al., 2014), but without reaching the threshold to trigger the transition from C3 to C4 vegetation, even over a period of decades to centuries (Zhu et al., 2008; Caley et al., 2014). Lower temperatures reduce evaporation, promote the

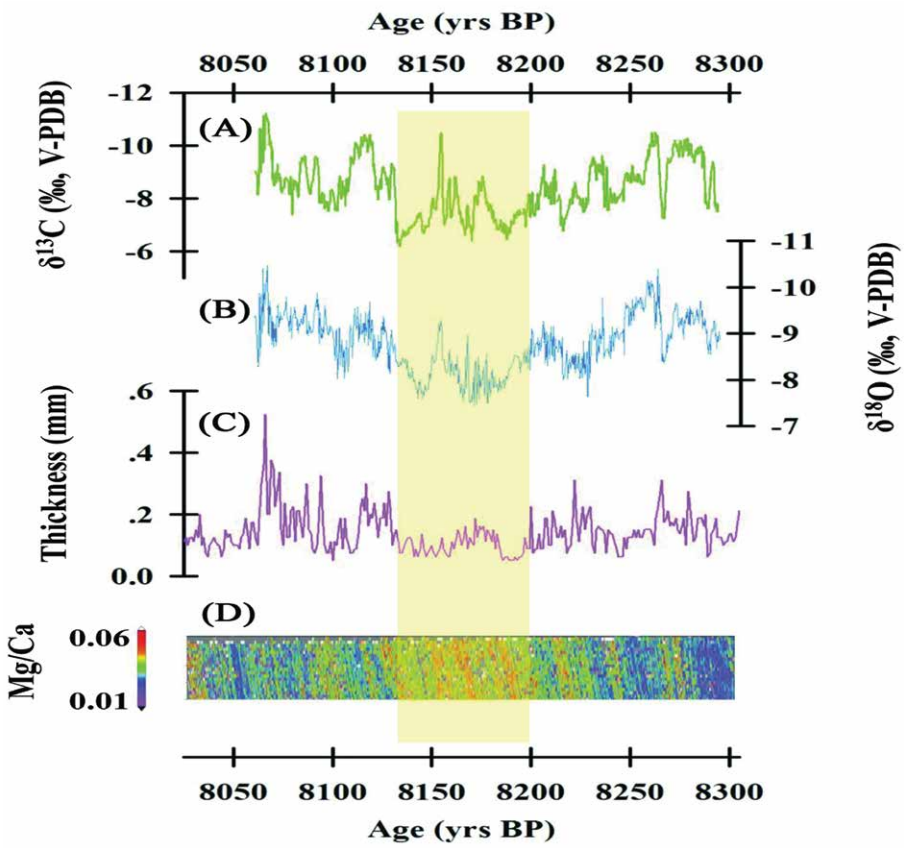


Figure 11. Comparison of multi-proxy records of stalagmite HS-4 from Heshang Cave (redrawn from Liu et al., 2013). (**A**) $\delta^{13}C$, (**B**) $\delta^{18}O$, (**C**) thickness of annual lamina, (**D**) Mg/Ca. The enriched $\delta^{13}C$ and $\delta^{18}O$ values, decreased thickness and increased Mg/Ca during the 8.2 ka event (the light-yellow bar) denoted the weakening of ASM and the possibility of PCP in the epikarst zone.

condensation of water vapor and precipitation, especially in mountainous Southwest China (Jiang et al., 2014). With this temperature and hydrology combination, Southwest China would still maintain the characteristics of a subtropical, humid monsoon climate, higher speleothem $\delta^{18}O$ and lower $\delta^{13}C$ values (Fig. 10).

It is worth pointing out that the simplified concept model comprises the abovementioned five scenarios and does not involve the complex cave factors that can cause isotopic fractionation of carbon, such as drip rate (Hansen et al., 2013), cave ventilation (Spötl et al., 2005) and degassing of $CO_2$ (Fairchild et al., 2006; Mickler et al., 2006; Scholz et al., 2009; Huang et al., 2016). So, speleothems from a cave with stable temperature, high humidity, poor ventilation, and that are deposited at isotopic equilibrium fractionation (Hendy, 1971), are preferential for the reconstruction of paleoclimate and paleoenvironment. In addition, the replication of speleothem records from a cave is commendatory for judging the paleoclimatic suitability of speleothems (Dorale and Liu, 2009).

**Case Study for Stalagmite $\delta^{13}C$, $\delta^{18}O$, Mg/Ca and Paleoclimate**

The climate- and environment-dominated organic signals carried by DIC-$\delta^{13}C$ may be masked by some inorganic and physical factors mentioned above. In such cases, the analysis of multi-proxies is recommended to assess the influences of these factors; e.g., higher Mg/Ca ratio and lower $Ca^{2+}$ concentration in drip water have been used to reflect the PCP effect (Fairchild et al., 2006; Luo et al., 2013), and $^{87}Sr/^{86}Sr$ has been used to reflect the dissolution of host rock (Oster et al., 2010). Multi-proxy records from the same cave will undoubtedly raise the reliability of paleoclimate and paleoenvironment reconstruction. Here, a case study to demonstrate this argument is presented.

Heshang Cave is in central China (30°27' N, 110°25' E, 294 m a.s.l, ~290 km northeast of Furong Cave) (Fig. 1B), and has been monitored for more than 10 years (Hu et al., 2008a; Henderson et al., 2008). The $\delta^{18}O$ of rainwater above Heshang Cave is not altered by evaporation when it filters into the cave and stalagmite $\delta^{18}O$ has been used as the indicator for changes in rainfall (Hu et al., 2008b). As shown in Figure 11, both the sub-annually resolved $\delta^{18}O$, $\delta^{13}C$ and Mg/Ca values of stalagmite HS-4 from Heshang Cave increased significantly during the 8.2 ka event, a global cold-climatic event, which occurred at ~8.2 ka BP (Liu et al., 2013). In other words, the decrease in rainfall indicated by the increased $\delta^{18}O$ of stalagmite HS-4 was strongly supported by higher $\delta^{13}C$ and high ratios of Mg/Ca (Liu et al., 2013). This is because in Heshang Cave, lower rainfall means lower karst flow rates and more opportunity for PCP, which leads to higher stalagmite $\delta^{13}C$ and Mg/Ca (Johnson et al., 2006; Hu et al., 2008a; Henderson et al., 2008; Liu et al., 2013), as described in scenario III (Fig. 10). In contrast, lower stalagmite $\delta^{18}O$ means more rainfall, faster karst flow rates and no/less PCP, which can result in lower $\delta^{13}C$ and Mg/Ca ratio, as described in scenario I (Fig. 10).

It is known that stalagmite $\delta^{13}C$ shows significant variability and uncertainty, even in stalagmites from the same cave. There are different correlations between the $\delta^{13}C$ and $\delta^{18}O$ values for a given stalagmite on different time scales, e.g., orbital-, millennial- and centennial-scale (Liu et al., 2016). Complex factors may influence stalagmite $\delta^{13}C$, such as vegetation types and density, biomass, soil $pCO_2$, and karst flow rate, which are all closely associated with climate change-dominated temperature and precipitation (McDermott, 2004). Cave monitoring and multi-proxy analysis for stalagmites, including $\delta^{13}C$, $\delta^{18}O$, Mg/Ca, $^{87}Sr/^{86}Sr$, is particularly important for the reliable interpretation of $\delta^{13}C$ (Li et al., 2014b). In addition, lacustrine and peat records are a valuable source of information for subtropical Central and Southern China, because pollen records from neighboring regions can provide direct evidence for variation in regional vegetation and climate, and may provide supporting evidence for changes in local vegetation.

## Conclusions

Although speleothem $\delta^{13}C$ has been used to trace the evolution of regional vegetation and rocky desertification history, there has not been a systematic investigation on the present vegetation types and isotopic composition of plants in Southern and Central China areas with humid subtropical monsoon climate. In this study, 130 plant samples were collected from five sites with different RDD in Southwest China, revealing most plants to be C3 plants. There was no correlation between the $\delta^{13}C_{SOM}$ and RDD; in contrast, the DIC-$\delta^{13}C$ of drip water and $\delta^{13}C$ of "modern deposits" in caves changed with large amplitude due to hydrological conditions in the epikarst zone and geological and physical characteristics of individual caves/drip sites. This study revealed that, at present, rocky desertification in Southwest China does not cause the transition of C3 to C4 vegetation. Additionally, based on pollen records in Southern and Central China, it was inferred that this transition did not occur during the Last Glacial period.

A concept model comprising five scenarios was proposed, indicating that the evolution of ASM and rocky desertification can be recorded in speleothem $\delta^{13}C$, mainly by the change of epikarst hydrological conditions rather than the change of vegetation types. Cave monitoring and multi-proxy analysis are recommended to identify the influence of non-climatic factors, which are believed to be instrumental in providing a reliable explanation of speleothem $\delta^{13}C$ and reconstruction of paleoenvironment.

## Acknowledgements

Thank you to Mr. Huang Chuliang for his great assistance with field work in Guizhou Province. Dr. Liu Jinchun, School of Life Sciences, Southwest University, China, is greatly appreciated for identification of all plants. A profession-

al English translator, Dr. Xiang Xinyi, Southwest University, China, is also greatly appreciated for her effort in polishing the manuscript. This research was supported by NSFC (Nos. 41172165, 41440020), the Fundamental Research Funds for the Central Universities (Nos. XDJK2017A010, XDJK2013A012) to Ting -Yong Li.

## References

Baker, A., Ito, E., Smart, P.L., Mcewan, R.F., 1997, Elevated and variable values of 13C in speleothems in a British cave system, Chemical Geology, v. 136, s3-4, p. 263–270.

Bar-Matthews, M., Matthews A., Sass E., Halicz L., Ayalon A., 1996, Carbon and oxygen isotope study of the active water-carbonate system in a karstic Mediterranean cave: Implications for paleoclimate research in semiarid regions, Geochimica et Cosmochimica Acta, v. 60, n. 2, p. 337–347. https://doi.org/10.1016/0016-7037(95)00395-9.

Bar-Matthews, M., Ayalon, A., Kaufman, A., 1997, Late Quaternary paleoclimate in the eastern Mediterranean region from stable isotope analysis of speleothems at Soreq Cave, Israel, Quaternary Research, v. 47, n. 2, p. 155–168. https://doi.org/10.1006/qres.1997.1883.

Bar-Matthews, M., Ayalon, A., Kaufman, A., 2000, Timing and hydrological conditions of Sapropel events in the Eastern Mediterranean, as evident from speleothem, Soreq Cave, Israel, Chemical Geology, v. 169, n. 1, p. 145–156. https://doi.org/10.1016/S0009-2541(99)00232-6.

Zhu Cheng, Xing Chen, Zhang GuangSheng, Ma ChunMei, Zhu Qing, Li ZhongXuan, Xu WeiFeng, 2008, Spore-pollen-climate factor transfer function and paleoenvironment reconstruction in Dajiuhu, Shennongjia, Central China, Chinese Science Bulletin, v. 53, p. 42–49.

Caley, T., Roche, D.M., Renssen, H., 2014, Orbital Asian summer monsoon dynamics revealed using an isotope-enabled global climate model, Nature Communications, v. 5, p. 5371. https://doi:10.1038/ncomms6371.

Cerling, T.E., 1984, The stable isotopic composition of modern soil carbonate and its relationship to climate, Earth and Planetary Science Letters, v. 71, p. 229–240. https://doi.org/10.1016/0012-821X(84)90089-X.

Hu Chaoyong, Henderson, G.M., Huang Junhua, Chen Zhenghong, Johnson, K.R., 2008a, Report of a three-year monitoring programme at Heshang Cave, Central China, International Journal of Speleology, v. 37, n. 3, p. 143–151. https://doi.org/10.5038/1827-806X.37.3.1.

Hu Chaoyong, Henderson, G.M., Huang Junhua, Xie S.C., Sun Y., Johnson, K.R., 2008b, Quantification of Holocene Asian monsoon rainfall from spatially separated cave records, Earth and Planetary Science Letters, v. 266, n. 3-4, p. 221–232.

Coplen, T.B., Winograd, I.J., Landwehr, J.M., Riggs, A.C., 1994, 500,000-year stable carbon isotopic record from Devil's Hole, Nevada, Science, v. 263, n. 5145, p. 361–365. https://doi.org/10.1126/science.263.5145.361.

Cosford, J., Hairou Qing, Mattey, D., Eglington, B., Meilang Zhang, 2009, Climatic and local effects on stalagmite $\delta^{13}C$ values at Lianhua Cave, China, Palaeogeography, Palaeoclimatology, Palaeoecology, v. 280, n. 1, p. 235–244. https://doi.org/10.1016/j.palaeo.2009.05.020.

Yuan Daoxian, 1993, Environmental change and human impact on karst in south China, *in* Williams, P., ed., Karst terrains: environmental change and human impact, Catena Supplement, v. 25, p. 104.

Yuan Daoxian, 1997, Rock desertification in the subtropical karst of south China, Zeitschrift fur Geomorphologie, n. 108, p. 81–90.

Liu Dianbing, Wang Yongjin, Cheng Hai, Edwards R.L., Kong Xinggong, Li Ting-Yong, 2016, Strong coupling of centennial-scale changes of Asian monsoon and soil processes derived from stalagmite $\delta^{18}O$ and $\delta^{13}C$ records, southern China, Quaternary Research, v. 85, n. 3, p. 333–346.

Dienes, P., 1980, The isotopic composition of reduced organic carbon, *in* Fritz, P., Fontes, J. C., eds., Handbook of Environmental Isotope Geochemistry I: The Terrestrial Environment, Amsterdam: Elsevier.

Dorale, J.A., González, L.A., Reagan, M.K., Pickett, D.A., Murrell, M.T., Baker, R.G., 1992, A high-resolution record of Holocene climate change in speleothem calcite from Cold Water Cave, northeast Iowa, Science, v. 258, p. 1626–1630. https://doi.org/10.1126/science.258.5088.1626.

Dorale, J.A., Edwards, R.L., Emi, I., Gonzalez, L.A., 1998, Climate and vegetation history of the midcontinent from 75 to 25 ka: A speleothem record form Crevice Cave, Missouri, USA, Science, v. 282, p. 1871–1874. https://doi.org/10.1126/science.282.5395.1871.

Dorale J, Liu Zaihua, 2009, Limitations of Hendy Test criteria in judging the paleoclimatic suitability of speleothems and the need for replication, Journal of Cave and Karst Studies, v. 71, n. 1, p. 73–80.

Dreybrodt, W., Scholz, D., 2011, Climatic dependence of stable carbon and oxygen isotope signals recorded in speleothems: From soil water to speleothems calcite, Geochimica et. Cosmochimica Acta, v. 75, n. 3, p. 734–752. https://doi.org/10.1016/j.gca.2010.11.002.

Fairchild, I.J., Smith, C.L., Baker, A., Fuller, L., Spötl, C., Mattey, D., McDermott, F., E.I.M.F., 2006, Modification and preservation of environmental signals in speleothems, Earth Science Reviews, v. 75, p. 105–153. https://doi.org/10.1016/j.earscirev.2005.08.003.

Frisia, S., Fairchild, I.J., Fohlmeister, J., Miorandi, R., Spötl, C., Borsato, A., 2011, Carbon mass-balance modeling and carbon isotope exchange processes in dynamic caves, Geochimica et Cosmochimica Acta, v. 75, n. 2, p. 380–400. https://doi.org/10.1016/j.gca.2010.10.021.

Genty, D., Baker, A., Massault, M., Proctor, C., Gilmour, M., Pons-Branchu, E., Hamelin, B., 2001, Dead carbon in stalagmites: carbonate bedrock paleodissolution vs. ageing of soil organic matter: Implications for $^{13}C$ variations in speleothems, Geochimica et Cosmochimica Acta, v. 65, n.20, p. 3443–3457. https://doi.org/10.1016/S0016-7037(01)00697-4.

Genty, D., Blamart, D., Ouahdi, R., Gilmour, M., Baker, A., Jouzel J., Van-Exter, S., 2003, Precise dating of Dansgaard-Oeschger climate oscillations in western Europe from stalagmite data, Nature, v. 421, p. 833–837. https://doi.org/10.1038/nature01391.

Cheng Hai, Edwards, R. L., Sinha Ashigh, C. Spötl, Yi Liang, Chen Shitao, Kelly, M., Gayatri Kathayat, Wang Xiangfeng, Li Xianglei, Kong Xinggong, Wang Yongjin, Ning Youfeng, Zhang Haiwei, 2016, The Asian monsoon over the past 640,000 years and ice age terminations, Nature, v. 534, p. 640–646. https://doi.org/10.1038/nature18591.

Hansen, M., Dreybrodt, W., Scholz, D., 2013, Chemical evolution of dissolved inorganic carbon species flowing in thin water films and its implications for (rapid) degassing of $CO_2$ during speleothem growth, Geochimica et Cosmochimica Acta, v 107, p. 242–251. https://doi.org/10.1016/j.gca.2013.01.006.

Wang H.-B, Li Ting-Yong, Yuan N., Li J.-Y., 2014, Environmental signification and characteristics of δD and δ18O variation in drip water in Yangkou Cave, Chongqing, Carsologica Sinica, v. 33, n. 2, p. 146–155. (In Chinese with English abstract and figures).

Henderson, G.M., Hu C.Y,. Johnson, K. R., 2008, Controls on trace elements in stalagmites derived from *in situ* growth in a Chinese cave, 18th Annual V M Goldschmidt Conference A 366.

Hendy, C.H., 1971, The isotopic geochemistry of speleothems: The calculation of the effects of different modes of formation on the isotopic composition of speleothems and their applicability as palaeoclimatic indicators, Geochimica et Cosmochimica Acta, v. 35, n. 8, p. 801–824. https://doi.org/10.1016/0016-7037(71)90127-X.

Holmgren, K., Lee-Thorp, J.A., Cooper, G.R.J., Lundblad, K., Partridge, T.C., Scott, L., Sithaldeen, R., Talma, A.S., Tyson, P.D., 2003, Persistent millennial-scale climatic variability over the past 25,000 years in southern Africa, Quaternary Science Review, v. 22, n. 21-22, p. 2311–2326. https://doi.org/10.1016/S0277-3791(03)00204-X.

Li Hong Chun, Gu D.L., Chen W.J., Yuan Daoxian, Li Ting-Yong, 1998, Application of high-resolution carbon isotope record of a stalagmite from the Shihua Cave, Beijing— $\delta^{13}C$ record of deforestation after the establishment of the Grand Capital (Yuan Dadu) in 1272 A. D., Geological Review, v. 44, n. 5, p. 456–463 (In Chinese with English abstract). http://baike.baidu.com/l/R39lSAyx?bk_share=copy.
https://baike.baidu.com/item/%E5%A4%A7%E7%94%A8%E9%95%87/32613.

Xiong K.N., Li P., Zhou Z.F., An Y.L., Lv T., Lan A.J., 2002, Remote sensing of rocky desertification in karst: a case study of Guizhou Province: Geological Publishing House, v. 23.

Jo Kyoung-ham, Woo Kyung Sik, Sangheon Yi, Yang Dong-Yoon, Lim Hyoun Soo, Wang Yongjin, Cheng Hai, Edwards, R.L., 2014, Mid-latitude interhemispheric hydrologic seesaw over the past 550,000 years, Nature, v. 508, p. 378–382. https://doi.org/10.1038/nature13076.

Johnson, K. R., Hu Chaoyong, Belshaw, N.S., Henderson, G.M., 2006, Seasonal trace-element and stable-isotope variations in a Chinese speleothem: The potential for high-resolution paleomonsoon reconstruction, Earth and Planetary Science Letters, v. 244, n. 1-2, p. 394–407. https://doi.org/10.1016/j.epsl.2006.01.064.

Lee-Thorp, J.A., Holmgren, K., Lauritzen, S.-E., Linge, H., Moberg, A., Partridge, T.C., Stevenson, C., Tyson, P.D., 2001, Rapid climate shifts in the southern African interior throughout the mid to late Holocene, Geophysical Research Letters, v. 28, p. 4507–4510. https://doi.org/10.1029/2000GL012728.

Martín-Chivelet, J., Muñoz-García, M.B., Edwards, R.L., Turrero, M.J., Ortega, A.I., 2011, Land surface temperature changes in Northern Iberia since 4000 yr BP, based on $\delta^{13}C$ of speleothems, Global Planetary Change, v. 77, n. 1-2, p. 1–12. https://doi.org/10.1016/j.gloplacha.2011.02.002.

Mattey, D.P., Atkinson, T.C., Barker, J.A., Fisher, R., Latin, J.P., Durrell, R., Ainsworth M., 2016, Carbon dioxide, ground air and carbon cycling in Gibraltar karst, Geochimica et Cosmochimica Acta, v. 184, p. 88–113. https://doi.org/10.1016/j.gca.2016.01.041.

McDermott, F., 2004, Palaeo-climate reconstruction from stable isotope variations in speleothems: a review, Quaternary Science Review, v. 23, n. 7, p. 901–918. https://doi.org/10.1016/j.quascirev.2003.06.021

Zhang Meilang, Zhu X.Y., Lin Y.S., Qin J.M., Zhang C., Luo R.G., Yang Y., 2006, Study on$\delta^{13}C$ isotope records from stalagmites, Guangxi Sciences. https://doi.org/10.3969/j.issn.1005-9164.2006.01.016.

Mickler, P.J., Stern, L.A., Banner, J.L., 2006, Large kinetic isotope effects in modern speleothems, Geological Society of America Bulletin, v. 118, n. 1/2, p. 65–81. https://doi.org/10.1130/B25698.1.

Zhao Min, Li Hong-Chun, Shen Chuan-Chou, Kang Su-Chen, Chou Chun-Yen, 2016, $\delta^{18}O$, $\delta^{13}C$, elemental content and depositional features of a stalagmite from Yelang Cave reflecting climate and vegetation changes since late Pleistocene in central Guizhou, China, Quaternary International. https://doi.org/10.1016/j.quaint.2016.07.022.

O´Leary, M.H., 1988, Carbon isotope in photosynthesis, Bioscience, v. 38, n. 5, p. 328–336.

Oster, J.L., Montañez, I.P., Guilderson, T.P., Sharp, W.D., Banner, J.L., 2010, Modeling speleothem $\delta^{13}C$ variability in a central Sierra Nevada cave using $^{14}C$ and $^{87}Sr/^{86}Sr$, Geochimica et Cosmochimica Acta, v. 74, n. 18, p.5228–5242.

Salomons, W., and Mook, W.G., 1986, Isotope geochemistry of carbonates in the weathering zone: The Terrestrial Environment B. Elsevier B.V.

Scholz, D., Mühlinghaus, C., Mangini, A., 2009, Modelling $\delta^{13}C$ and $\delta^{18}O$ in the solution layer on stalagmite surfaces, Geochimica et Cosmochimica Acta, p. 73, n. 9, p. 2592–2602.

Spötl, C., Fairchild, I.J., Tooth, A.F., 2005, Cave air control on drip water geochemistry, Obir Caves (Austria, p. implications for speleothem deposition in dynamically ventilated caves, Geochimica et Cosmochimica Acta, v. 69, p. 2451–2468.

Li Ting-Yong, 2007, The controlling factors research on the paleoenvironmental informations in stalagmite and the paleoclimate reconstruction since the last glacial period in Chongqing area, [Ph.D. dissertation]: Chongqing, China, Southwest University.

Li Ting-Yong, Daoxian Yuan, Li Hong Chun, Yangyan, Wang Jianli, Wang, Xinya, Li, Jun-Yun, Qin, Jiaming, Zhang, M Meilang, Lin, Yushi, 2007, High-resolution climate variability of southwest China during 57-70 ka reflected in a stalagmite $\delta^{18}O$ record from Xinya Cave, Science China Earth Sciences, v. 50, n. 8, p. 1202–1208. https://doi.org/10.1007/s11430-007-0059-z.

Li Ting-Yong, Shen Chuan-Chou, Li Hong Chun, Li Jun-Yun, Chiang Hong-Wei, Song Sheng-Rong, Yuan Daoxian, Chris D.-J., Gao LinPan, Zhou Liping, Wang Jian Li, Yang Ye Ming, Tang Liang-Liang, Xie Shi-You, 2011, Oxygen and carbon isotopic systematics of aragonite speleothems and water in Furong Cave, Chongqing, China, Geochimica et Cosmochimica Acta, v. 75, p. 4140–4156. https://doi.org/10.1016/j.gca.2011.04.003.

Li Ting-Yong, Li Hong Chun, Xiang Xiao, Kuo TzShing, Li Jun Yan, Zhou Fu Li, Chen Hong Li, Peng Ling Li, 2012, Transportation characteristics of $\delta^{13}C$ in the plants-soil-bedrock-cave system in Chongqing karst area, Science China Earth Sciences, v. 55, n. 4, p. 685–694. https://doi.org/10.1007/s11430-011-4294-y.

Li Ting-Yong, Shen Chuan-Chou, Huang L.-J., Jiang X.-Y., Yang X.-L., Mii H.-S., Lee S.-Y., and Lo L., 2014a, Stalagmite-inferred variability of the Asian summer monsoon during the penultimate glacial–interglacial period, Climate of the Past, v. 10, p. 1211–1219. https://doi.org/10.5194/cp-10-1211-2014.

Kuo Tz-Shing, Liu Zi-Qi, Li Hong-Chun, Wan Nai-Jung, Shen Chuan-Chou, Ku The-Lung, 2011, Climate and environmental changes during the past millennium in central western Guizhou, China as recorded by Stalagmite ZJD-21, Journal of Asian Earth Sciences, v. 40, n. 6, p. 1111–1120. https://doi.org/10.1016/j.jseaes.2011.01.001.

Trumbow, S., 2000, Age of soil organic matter and soil respiration: radiocarbon constraints on below-ground c dynamics, Ecological Applications, v. 10, n. 2, p. 399–411. https://doi.org.10.1890/1051-0761.

Liu Y. H., Henderson, G.M., Hu ChaoYong, Mason, A.J., Charnley, N., Johnson, K. R., Xie S.–C., 2013, Links between the East Asian monsoon and North Atlantic climate during the 8,200-year event, Nature Geoscience, v. 6, p. 117–120. https://doi.org/10.1016/j.yqres.2016.02.008.

Huang W., Dianbing Liu, Wang Yongjin, Zhang Z.Q., 2016, Research status and advance in carbon isotope ($\delta^{13}C$) variation from stalagmite, Advances in Earth Science, v. 31, n. 9, p. 968–983. (In Chinese with English Abstract)

Zhou Weijan, Yu Xuefeng, Jull, A.J.T., Burr, G., Xiao J.Y., Lu Xuefeng, Xian Feng, 2004, High-resolution evidence from Southern China of an early Holocene optimum and a mid-Holocene dry event during the past 18,000 years, Quaternary Research, v. 62, p. 39−48.

Luo Weijun, Wang S.J., Liu X.M., 2007, Biomass effect on carbon isotope ratios of modern calcite deposition and its mechanism: A case study of four caves in Guizhou Province, China, Geochimica, v. 36, n. 4, p. 344–350. (In Chinese with English Abstract)

Luo Weijun, Wang S.J., 2009, Transmission of $\delta^{13}C$ signals and its paleoclimatic implications in Liangfeng Cave system of Guizhou Province, SW China, Environmental Earth Science, v. 59, p. 655–661. https://doi.org/10.1007/s12665-009-0062-0.

Luo Weijun, Wang S., Xie X., Zhou Y., Li Ting-Yong, 2013, Temporal and spatial variations in hydrogeochemistry of cave percolation water and their implications for four caves in Guizhou, China, China Journal of Geochemistry, v. 32, n. 2, p. 119–129. https://doi.org/10.1007/s12665-009-0062-0.

Shen W., Wang J.L., Jiang X.S., Mao Q.Y., 2016, Hydrochemistry and $\delta^{13}C_{DIC}$ features of cave water in Naduo Cave, Guizhou and their influencing factors, Carsologica Sinica, v. 35, n. 1, p. 98–105. (In Chinese with English abstract)

Zhong Wei, Xue Jibin, Zheng Yonming, Ma Qiaohong, Cai Ying, Ouyang Jun, Xu Liubin, Zhou Shangzhe, Yu Xuefeng, 2010, Variations of monsoonal precipitation over the last 16,000 years in the eastern Nanling Mountains, South China, Journal of Paleolimnology, v. 44, p. 177–188.

Ding Yihui, Sun Y., 2002, Seasonal march of the East Asian summer monsoon and related moisture transport, Weather and Climate, v. 1, p. 18–23. (In Chinese with English Abstract)

Ding Yihui, Chan Johnny C.L., 2005, The East Asian summer monsoon: an overview, Meteorology and Atmospheric Physics, v. 89, p. 117–142. https://doi.org/10.1007/s00703-005-0125-z.

Li Z.H., Driese, S.G., Cheng Hai, 2014b, A multiple cave deposit assessment of suitability of speleothem isotopes for reconstructing palaeo-vegetation and palaeo-temperature, Sedimentology, v. 61, n. 3, p. 749–766. https://doi.org/10.1111/sed.12078.

Jiang Zongcheng, Lian Yanqing, Qin Xqaoqun, 2014, Rocky desertification in southwest china: impacts, causes, and restoration, Earth Science Review, v. 132, n. 3, p. 1–12. https://doi.org/10.1016/j.earscirev.2014.01.005.

# GUIDE TO AUTHORS

The *Journal of Cave and Karst Studies* is a multidisciplinary journal devoted to cave and karst research. The *Journal* is seeking original, unpublished manuscripts concerning the scientific study of caves or other karst features. Authors do not need to be members of the National Speleological Society, but preference is given to manuscripts of importance to North American speleology.

LANGUAGES: The *Journal of Cave and Karst Studies* uses American-style English as its standard language and spelling style, with the exception of allowing a second abstract in another language when room allows. In the case of proper names, the *Journal* tries to accommodate other spellings and punctuation styles. In cases where the Editor-in-Chief finds it appropriate to use non-English words outside of proper names (generally where no equivalent English word exist), the *Journal* italicizes them. However, the common abbreviations i.e., e.g., et al., and etc. should appear in roman text. Authors are encouraged to write for our combined professional and amateur readerships

CONTENT: Each paper will contain a title with the authors' names and addresses, an abstract, and the text of the paper, including a summary or conclusions section. Acknowledgments and references follow the text. Manuscripts should be limited to 6,000 words and no more than 10 figures and 5 tables. Larger manuscripts may be considered, but the *Journal* reserves the right to charge processing fees for larger submissions.

ABSTRACTS: An abstract stating the essential points and results must accompany all articles. An abstract is a summary, not a promise of what topics are covered in the paper.

STYLE: The *Journal* consults The Chicago Manual of Style on most general style issues.

REFERENCES: In the text, references to previously published work should be followed by the relevant author's name and date (and page number, when appropriate) in brackets. All cited references are alphabetical at the end of the manuscript with senior author's last name first, followed by date of publication, title, publisher, volume, and page numbers. Geological Society of America format should be used (see http://www.geosociety.org/documents/gsa/pubs/GSA_RefGuide_Examples.pdf). Please do not abbreviate periodical titles. Web references are acceptable when deemed appropriate. The references should follow the style of: Author (or publisher), year, Webpage title: Publisher (if a specific author is available), full URL (e.g., http://www.usgs.gov/citguide.html), and the date the website was accessed in brackets. If there are specific authors given, use their name and list the responsible organization as publisher. Because of the ephemeral nature of websites, please provide the specific date. Citations within the text should read: (Author, Year).

SUBMISSION: Manuscripts are to be submitted via the PeerTrack submission system at http://www.edmgr.com/jcks/. Instructions are provided at that address. At your first visit, you will be prompted to establish a login and password, after which you will enter information about your manuscript and upload your manuscript, tables, and figure files. Manuscript files can be uploaded as DOC, WPD, RTF, TXT, or LaTeX. Note: LaTeX files should not use any unusual style files; a LaTeX template and BiBTeX file may be obtained from the Editor-in-Chief. Table files can be uploaded as DOC, WPD, RTF, TXT, or LaTeX files and figure files can be uploaded as TIFF, AI, EPS, or CDR files. Extensive supporting data may be placed on the Journal's website as supplemental material at the discretion of the Editor-in-Chief. The data that are used within a paper must be made available upon request. Authors may be required to provide supporting data in a fundamental format, such as ASCII for text data or comma-delimited ASCII for tabular data.

DISCUSSIONS: Critical discussions of papers previously published in the *Journal* are welcome. Authors will be given an opportunity to reply. Discussions and replies must be limited to a maximum of 1000 words and discussions will be subject to review before publication. Discussions must be within 6 months after the original article appears.

MEASUREMENTS: All measurements will be in Systeme Internationale (metric) except when quoting historical references. Other units will be allowed where necessary if placed in parentheses and following the SI units.

FIGURES: Figures and lettering must be neat and legible. Figure captions should be on a separate sheet of paper and not within the figure. Figures should be numbered in sequence and referred to in the text by inserting (Fig. x). Most figures will be reduced, hence the lettering should be large. Photographs must be sharp and high contrast. Figures must have a minimum resolution of 300 dpi for acceptance. Please do not submit JPEG images.

TABLES: See http://caves.org/pub/journal/PDF/Tables.pdf to get guidelines for table layout.

COPYRIGHT AND AUTHOR'S RESPONSIBILITIES: It is the author's responsibility to clear any copyright or acknowledgement matters concerning text, tables, or figures used. Authors should also ensure adequate attention to sensitive or legal issues such as land owner and land manager concerns or policies and cave location disclosures.

PROCESS: All submitted manuscripts are sent out to at least two experts in the field. Reviewed manuscripts are then returned to the author for consideration of the referees' remarks and revision, where appropriate. Revised manuscripts are returned to the appropriate Associate Editor who then recommends acceptance or rejection. The Editor-in-Chief makes final decisions regarding publication. Upon acceptance, the senior author will be sent one set of PDF proofs for review. Examine the current issue for more information about the format used.

# Journal of Cave and Karst Studies

Volume 80 Number 4 December 2018

## CONTENTS